Doctoral Dissertation (Censored)
博士論文（要約）

Statistical analyses of optically selected galaxy clusters from Subaru Hyper Suprime-Cam

(すばるハイパーシュプリームカムの可視光観測により検出された銀河団の統計的研究)

A Dissertation Submitted for the Degree of Doctor of Philosophy

December 2019

令和元年 12 月博士（理学）申請

Department of Physics, Graduate School of Science,

The University of Tokyo

東京大学大学院理学系研究科物理学専攻

Ryoma Murata

村田 龍馬

Abstract

Cosmological observations in the last twenty years have established the standard Λ-dominated Cold Dark Matter (ΛCDM) cosmological model based on General Relativity for the gravity theory thanks to the increasing amount of observational data. It is essential to validate the consistency of this model with other independent cosmological probes or to constrain extensions of the standard model such as self-interacting dark matter, time-evolving dark energy, and modified gravity with observational data.

Galaxy clusters are the most massive gravitationally bound structure in the Universe with mass scales $\sim 10^{14} M_{\odot}$, which form in dark matter halos after interactions between gravitational dynamics and baryonic process related to galaxy formation. Observations of galaxy clusters in the literature have revealed and constrained the existence and nature of dark matter, dark energy, baryonic matter, and galaxy evolution and formation with other cosmological and observational probes.

Given the smaller number of such massive dark matter halos in which galaxy clusters reside, we require deep imaging data from wide field-of-view surveys to investigate the statistical properties of galaxy clusters over a wide redshift range. The recent development of wide-field optical imaging surveys such as the Hyper Suprime-Cam Subaru Strategic Program (HSC-SSP) makes an optical selection of galaxy clusters based on red member galaxies in such cluster regions particularly powerful, typically with a larger number of galaxy clusters than those selected by X-ray or radio wavelengths at present.

With the same imaging data, such wide-field optical imaging surveys also enable us to calibrate the relation of galaxy cluster mass (M) and the number of red member galaxies above some luminosity threshold for each cluster (N), called optical richness, through weak gravitational lensing effects around galaxy clusters by statistically averaging over a large number of weakly and systematically deformed shapes of distant galaxies to reveal their mass profiles with equal sensitivity to the dark and baryonic matter. Constraining this mass-richness relation via weak gravitational lensing is fundamentally important to connect theories or simulations with observations on galaxy clusters, since the halo mass determine the physical properties dominantly such as density profiles of dark matter halo and galaxy evolution and formation physics. Also, constraining the mass distribution function of dark matter halos at galaxy cluster mass scales leads to cosmological parameter estimations.

Among the physical properties of galaxy clusters, the splashback radius has been recently proposed as a physical boundary of dark matter halos at the outskirts from a suite of high-resolution N-body simulations, which separates orbiting from accreting materials (e.g., dark matter and galaxies) as a sharp density edge. At the splashback radius, the logarithmic derivative of density profiles is predicted to drop significantly over a narrow range of radius due to piling up of materials with small radial velocities at their first orbital

apocenter after infall into halos. Importantly, recent observational constraints from different survey data in the literature on the splashback radius around optically selected galaxy clusters from an optical cluster-finding algorithm, called redMaPPer, have shown that the observed splashback radius is $\sim 20\%$ smaller than that predicted by N-body simulations under the ΛCDM model at a high significance ($\sim 4\sigma$), with the help of the mass-richness relation from weak gravitational lensing effects. These observations with high signal-to-noise ratios are based on statistical measurements of projected photometric galaxy densities around galaxy clusters, since dynamics of galaxies are expected to follow dark matter distribution in the outskirts based on gravitational potentials dominantly determined by the larger amount of dark matter. The dependence of the splashback radius on new physics such as self-interacting dark matter, time-evolving dark energy, and modified gravity have been investigated in the literature over the last five years to try to explain the deviation in the observed splashback radius from the standard model. The features of the splashback radius have also been known as probes of galaxy formation and evolution with galaxy color or magnitude cuts.

As a test of the ΛCDM model, in this thesis, we present observational and statistical studies of optically selected galaxy clusters on the mass-richness relation and the splashback radius with mock simulation analyses. We employ the data catalogs from the ongoing HSC-SSP with the Subaru telescope for optically selected galaxy clusters, weak lensing analyses, and photometric galaxies. We use ~ 2000 optically selected galaxy clusters from the independent cluster-finding algorithm, called CAMIRA, at a wide cluster redshift range of $0.1 < z_{\rm cl} < 1.0$ thanks to deep and high-resolution HSC images, whereas previous observational works in the literature on the mass-richness relation and the splashback radius are limited to $z_{\rm cl} \lesssim 0.7$.

First, we measure stacked weak lensing profiles around the HSC CAMIRA clusters over the wide redshift range. We detect lensing signals around high-redshift clusters at $0.7 < z_{\rm cl} < 1.0$ with a signal-to-noise ratio of 19 within comoving radius range $0.5 \lesssim R \lesssim 15h^{-1}$Mpc. We constrain their richness-mass relations $P(\ln N|M, z_{\rm cl})$ assuming a log-normal distribution without informative priors on model parameters, by jointly fitting to the lensing profiles and abundance measurements under two different sets of cosmological model parameters in the ΛCDM model based on the cosmic microwave background (CMB) measurements from the *Planck* and *WMAP* satellites. We show that constraints on the mean relation $\langle M|N\rangle$ with a precision of $\sim 5\%$ for each model are consistent between the *Planck* and *WMAP* models, whereas the scatter values $\sigma_{\ln M|N}$ for the *Planck* model are systematically larger than those for the *WMAP* model, which is consistent with the literature. In addition, we show that the scatter values for the *Planck* model increase toward lower richness values when employing a flexible parametrization for the mass-richness relation, whereas those for the *WMAP* model are consistent with constant values as a function of richness. This result highlights the importance of the scatter in the mass-richness relation to constrain the cosmological parameters from galaxy clusters.

Second, we present analyses on the splashback radius of the HSC CAMIRA clusters with the results of the analysis for the mass-richness relation. We detect the splashback feature from the projected cross-correlation measurements between the clusters and photometric galaxies over the wide redshift range, including for high redshift clusters at $0.7 < z_{\rm cl} < 1.0$, thanks to deep HSC images. We investigate the dependence of splashback features on cluster redshift, richness, galaxy magnitude limits, and galaxy colors over the wide redshift range, which should also be informative to compare with hydrodynamic galaxy simulations when available for galaxy evolution and formation studies. We find that constraints from red galaxy

populations only are more precise than those without any color cut, leading to 1σ precisions of $\sim 15\%$ for cluster samples at $0.4 < z_{\rm cl} < 0.7$ and $0.7 < z_{\rm cl} < 1.0$. We also find that these constraints at $0.4 < z_{\rm cl} < 0.7$ and $0.7 < z_{\rm cl} < 1.0$ are more consistent with the model predictions under the ΛCDM model with the help of our mass-richness relation ($\lesssim 1\sigma$) than their 20% smaller values as suggested by the previous studies based on redMaPPer clusters ($\sim 2\sigma$ for CAMIRA clusters). We also establish a methodology to investigate selection effects of optical cluster-finding algorithms on the observed splashback features by creating a mock galaxy catalog from a halo occupation distribution model and, for the first time, closely resembling the procedure in data analyses and model prediction calculations with the real data. With this methodology, we find that such effects are insignificant for the CAMIRA cluster-finding algorithm compared to our statistical errors. We also find that the redMaPPer-like cluster-finding algorithm induces a smaller inferred splashback radius in our mock catalog at the level of $\sim 15\%$, which well explains smaller splashback radii in the literature, whereas these biases are significantly reduced when increasing its aperture size. This finding suggests that aperture sizes of optical cluster finders that are smaller than splashback feature scales should induce significant biases on the inferred location of splashback radius.

Hence, for the first time, we conclude that the observed splashback radii are consistent with the theoretical predictions based on the ΛCDM model and our mass-richness relation from weak lensing effects for the HSC CAMIRA clusters at our precisions over the wide redshift range ($\sim 15\%$ for each bin of $0.1 < z_{\rm cl} < 0.4$, $0.4 < z_{\rm cl} < 0.7$, and $0.7 < z_{\rm cl} < 1.0$), and it is also the case for the redMaPPer clusters in the literature when accounting for the selection bias effects in the redMaPPer cluster-finding algorithm, which we find in the mock simulation analyses.

We can improve precisions on measurements of the mass-richness relation and the splashback radius by employing the upcoming full HSC survey data or other future survey data in various wavelengths, including X-ray and radio, in order to study cosmological and astrophysical aspects of galaxy clusters and the Universe itself in more detail. Our observational results with the CAMIRA clusters and our analysis frameworks and methodology for the observational data and mock observations are informative to conduct such analyses with properly accounting for the selection effects in the near future.

Contents

Abstract **i**

Acronyms and Abbreviations **vi**

1 Introduction **1**

1.1 The established standard cosmological model: ΛCDM model 1

1.2 Galaxy clusters as crossroads of cosmology and astrophysics 3

1.3 The observed inconsistency with the ΛCDM model in the splashback radius of optically selected galaxy clusters 6

1.4 The wide field-of-view and deep optical imaging survey of Subaru Hyper Suprime-Cam 10

1.5 Plan of this thesis 11

1.6 Convention and unit 12

2 The mass-richness relation of optically selected clusters from weak gravitational lensing and abundance with Subaru HSC first-year data **13**

2.1 Overview 13

2.2 HSC first-year dataset 14

2.2.1 HSC-SSP survey 14

2.2.2 HSC CAMIRA cluster catalog 14

2.2.3 HSC weak lensing shear catalog 15

2.2.4 HSC photometric redshift catalog 16

2.3 Measurement 16

2.3.1 Cluster abundance 17

2.3.2 Stacked cluster lensing profile 17

2.4 Forward modeling of cluster observables 21

2.4.1 Richness-mass relation 21

2.4.2 Abundance in richness and redshift bins 22

2.4.3 Stacked cluster lensing profile in richness and redshift bins 23

2.4.4 N-body simulation based halo emulator for the mass function and the lensing profile . 26

2.4.5 Covariance 27

2.5 Results 29

2.5.1 Posterior distribution of parameters 30

2.5.2 Joint probability $P_\beta(\ln M, \ln N)$ and mass-richness relation $P_\beta(\ln M|N)$ 33
2.5.3 Richness-mass relation $P(\ln N|M, z)$ 40
2.6 Discussion 40
2.6.1 Robustness of our results 40
2.6.2 Complementarity of abundance and stacked lensing profile measurements 42
2.6.3 Redshift evolution in the richness-mass relation 42
2.7 Chapter summary 46

3 The splashback radius of optically selected clusters with Subaru HSC Second Public Data Release 50

4 Summary and Conclusion 51

Acknowledgements 54

Appendix 56

A Optical cluster-finding algorithm 56

B Weak gravitational lensing 60
B.1 Overview 60
B.2 Lens equation 61
B.3 Distortion of finite image sizes: shear 63
B.4 Estimator 66
B.5 Tangential shear with respect to galaxy clusters 67
B.6 Stacked cluster-galaxy lensing 69
B.7 Possible systematic errors 70
B.7.1 Point-spread function 70
B.7.2 Redshift estimation 70
B.7.3 Off-centering 71
B.7.4 Dilution effect 71

C *N*-body simulation-based halo emulator: Dark Emulator 72

D Covariance for abundance and lensing measurements 74
D.1 Analytic model of the covariance matrix 74
D.2 Validation against realistic mock shear and cluster catalogs 77

E Sanity check of the mass-richness relation 79

F Model parameter constraint contours 81
F.1 Mass-richness relation 81

Bibliography 81

Acronyms and Abbreviations

BCG	Brightest Cluster Galaxy
CAMIRA	Cluster finding Algorithm based on Multi-band Identification of Red-sequence gAlaxies
CDM	Cold Dark Matter
CMB	Cosmic Microwave Background
COSMOS	Cosmological Evolution Survey
DES	Dark Energy Survey
DK14	Diemer & Krastsov (2014)
dof	degree-of-freedom
HOD	Halo Occupation Distribution
HSC	Hyper Suprime-Cam
HSC-SSP	Hyper Suprime-Cam Subaru Strategic Program
Kavli IPMU	Kavli Institute for the Physics and Mathematics of the Universe
KiDS	Kilo-Degree Survey
LSST	Large Synoptic Survey Telescope
MCMC	Markov Chain Monte Carlo
NAOJ	National Astronomical Observatory of Japan
NFW	Navarro-Frenk-White density profile model
PC	Principal Component
PDF	Probability Distribution Function
PDR	Public Data Release
PSF	Point-Spread Functions
PS1	Pan-STARRS1
Pan-STARRS	Panoramic Survey Telescope and Rapid Response System
redMaPPer	red-sequence Matched-filter Probabilistic Percolation cluster finding algorithm
SDSS	Sloan Digital Sky Survey
SSP	Subaru Strategic Program
SZ	Sunyaev–Zel'dovich effect
WFIRST	Wide-Field Infrared Survey Telescope
WMAP	Wilkinson Microwave Anisotropy Probe
ΛCDM	Λ-dominated Cold Dark Matter

Chapter 1

Introduction

1.1 The established standard cosmological model: ΛCDM model

Cosmological and astronomical observations in the last twenty years have firmly established the standard Λ-dominated Cold Dark Matter (ΛCDM) cosmological model for cosmic structure formation based on General Relativity for the gravity theory, thanks to increasing amounts of observational data with rapid progress in observational techniques and facilities, and theoretical foundations. The ΛCDM model has remarkably shown a success in explaining many different observational probes and evidences under a simple assumption with the same set of cosmological parameters within precisions. These cosmological probes include temperature angular anisotropies in the cosmic microwave background (CMB) from ground-based telescopes or satellites such as the *Wilkinson Microwave Anisotropy Probe* (*WMAP*; Hinshaw et al., 2013) and the *Planck* (Planck Collaboration et al., 2016), the redshift-distance relations based on the standard candle with the known intrinsic luminosity of Type Ia supernovae or the standard ruler of the baryon acoustic oscillation in galaxy spatial correlation functions in the late universe, the abundance of galaxy clusters, the gravitational lensing effects, and big bang nucleosynthesis. For more detail, we refer to a recent review in Weinberg et al. (2013) and references therein. At the same time, constraints from ongoing research with smaller statistical errors start to find possible hints of deviations or inconsistencies among different probes, e.g., on the Hubble parameter (Freedman, 2017; Wong et al., 2019), the amplitudes of matter density fluctuation from the early and late universe (Planck Collaboration et al., 2016b; Abbott et al., 2018; Costanzi et al., 2018; Hikage et al., 2019), and galactic small-scales (Del Popolo & Le Delliou, 2017).

In this standard paradigm, the energy components consist of ordinary baryonic matter (e.g., stars and galaxies) and radiation (e.g., photon) for only $\sim 5\%$ of the total energetic budget in the Universe at present, and dark components for another $\sim 95\%$ fraction: dark matter ($\sim 25\%$) and dark energy ($\sim 70\%$). Dark matter interacts only gravitationally and does not emit light from itself as stars and galaxies. The first observational evidence of dark matter is pointed by Fritz Zwicky thorough galaxy dynamics in the Coma

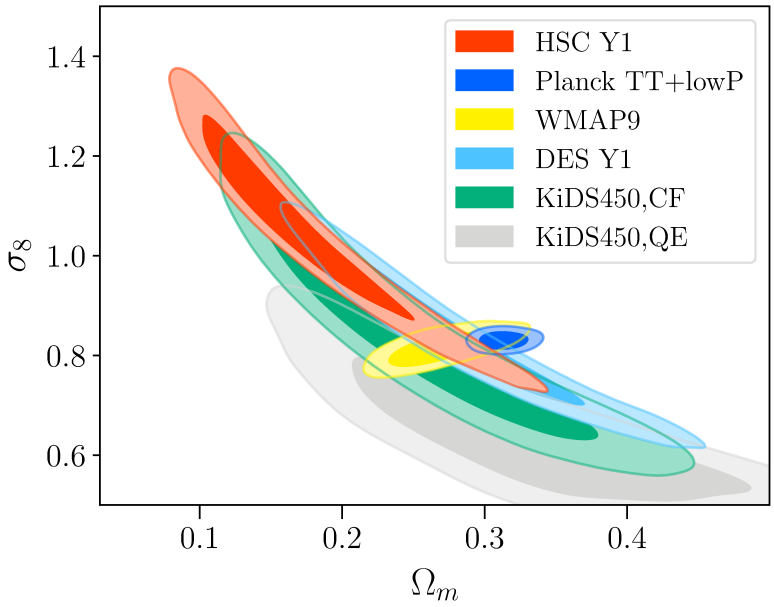

Figure 1.1 An example of the current constraints on the cosmological parameters in the standard ΛCDM model and a consistency level between different cosmological probes or methods. A marginalized posterior contour in the $\Omega_{\rm m0} - \sigma_8$ cosmological parameters in the ΛCDM model with 68% and 95% credible levels in red color is derived from the cosmological weak lensing cosmic shear analyses in Hikage et al. (2019) with the HSC first-year (Y1) data catalog, which uses cosmological weak lensing effects without employing galaxy clusters. For comparisons, contours from other surveys or the CMB measurements in the *Planck* or *WMAP* satellites (Planck Collaboration et al., 2016; Hinshaw et al., 2013) are also presented. This figure is reproduced from the left panel of Figure 5 in Hikage et al. (2019).

cluster (Zwicky, 1933). From cosmological observations, dark matter is favored to be cold and collisionless, and thus non-relativistic with small velocities dispersion at early universe. The standard model assumes no self-interaction of dark matter other than that via the gravitational field. Dark energy is a mysterious but dominant energy component at the present age of the Universe with negative pressure, leading to the observed accelerating expansion of the Universe in the late universe. The first clear evidence of the accelerating universe from dark energy is revealed by the redshift-distance relation from Type Ia supernova (Riess et al., 1998; Perlmutter et al., 1999). In the ΛCDM model, the cosmological constant Λ term without time evolution is introduced into the Einstein equation in General Relativity as dark energy. We humans do not understand the true nature of dark matter and dark energy, including any self-interaction of dark matter and time-evolution of dark energy as a deviation from the cosmological constant. Also, dark energy could be a signature of modified gravity as a violation of General Relativity at large cosmological scales. The effects of neutrino mass in cosmological scales have not been observationally detected although we know the existence from ground-based experiments on neutrino oscillations. Thus upcoming cosmological and astronomical observations will be valuable sources of such information with ground-based collider experiments.

Cosmic inflation as the exponential expansion stage generates tiny adiabatic, nearly scale-invariant, and Gaussian density perturbations via quantum mechanisms for the initial condition of the Universe for the energy components, and these perturbations subsequently amplify and assemble via gravitational instability

with interactions to a smaller amount of baryonic matters, to form cosmic structures such as planets, stars, galaxies, and galaxy clusters that we see today with telescopes, eventually life like us. In the ΛCDM model, the cosmic structures generally grow hierarchically due to larger density fluctuations at smaller length scales. In other words, smaller scales of perturbations in general collapse earlier to form smaller dark matter halos as a self-gravitationally bound system of dark matter. Subsequently, larger and more massive structures, such as more massive galaxies and galaxy clusters, gradually form and evolve in dark matter halos by accretion of these smaller dark matter halos into more massive halos, or mergers between different halos with similar masses through interacting with baryonic matters, e.g., for galaxy evolution and formation. Thus, galaxy evolution and formation processes are closely connected with properties of host dark matter halos such as halo mass or accretion rates of materials to halos.

The cosmological parameters for the standard flat ΛCDM model consists of independent six free parameters as follows: the Hubble parameter at present-day $H_0 \equiv 100\ h$ km s^{-1}Mpc^{-1} as often parametrized by h, normalized amounts of ordinary baryonic matter, cold dark matter, and the cosmological constant at present-day as $\Omega_{\rm b0}$, $\Omega_{\rm c0}$, and Ω_Λ, respectively, on a condition of $\Omega_{\rm b0} + \Omega_{\rm c0} + \Omega_\Lambda = 1$ for the flatness (thus two independent parameters from the three), the normalization and spectral index of the matter density fluctuation σ_8 and n_s, respectively, and a reionization optical depth τ for the CMB. We again refer to the review in Weinberg et al. (2013) for more details. The best-fit parameters in Planck Collaboration et al. (2016) can roughly explain almost all cosmological probes simultaneously. In particular, Figure 1.1 shows an example of the current constraints on the cosmological parameters of $\Omega_{\rm m0}$ and σ_8 from the CMB measurements in the *WMAP* and *Planck* with those from gravitational lensing measurements.

The ΛCDM model should be critically and more severely tested. It is essential to validate the consistency of this model with other independent cosmological probes by comparing with predictions of the ΛCDM model, or to constrain extensions of the standard cosmological model (e.g., self-interacting dark matter, time-evolving dark energy, modified gravity, and neutrino mass) from inconsistencies with the ΛCDM model if exists in observational data. However, in the era of precision cosmology with increasing amounts of observational data for smaller statistical errors, we should conduct data analyses with great care on systematic errors to avoid interpreting such systematics as new physics.

1.2 Galaxy clusters as crossroads of cosmology and astrophysics

Galaxy clusters are the most massive gravitationally bound structure in the Universe with mass scales $\sim 10^{14} M_\odot$, which form in dark matter halos around rare high peaks in the initial density field generated by the cosmic inflation after interactions between gravitational dynamics and baryonic process related to galaxy formation (see Allen et al., 2011; Kravtsov & Borgani, 2012; Weinberg et al., 2013; Wechsler & Tinker, 2018; Pratt et al., 2019; Walker et al., 2019; Vogelsberger et al., 2019, for recent reviews). Galaxy clusters are dominated by dark matter and therefore are useful sites for cosmological studies since N-body simulations

Figure 1.2 Subaru HSC *grz*-band color composite optical images of the richest clusters at different redshifts in the HSC CAMIRA optically selected cluster catalog in Oguri et al. (2018a). In each panel, the cluster photometric redshift and optical richness are denoted by z and N, respectively. The center of each panel presents the brightest cluster galaxy identified by the CAMIRA cluster-finding algorithm in Oguri (2014). The size of each panel is approximately 3.7 arcmin $\times$ 3.7 arcmin. From the lowest to the highest redshift, the size of 3.7 arcmin corresponds to 0.57 h^{-1}Mpc, 1.2 h^{-1}Mpc, 2.1 h^{-1}Mpc, and 2.6 h^{-1}Mpc in comoving coordinates, and 0.48 h^{-1}Mpc, 0.86 h^{-1}Mpc, 1.2 h^{-1}Mpc, and 1.3 h^{-1}Mpc in physical coordinates with the *Planck* cosmological parameters. This figure is reproduced from Figure 5 in Oguri et al. (2018a).

can predict cluster observables reasonably well. The abundance and clustering of massive clusters and their time evolution are known to be sensitive to cosmological parameters such as the matter density ($\Omega_{\rm m0}$), the normalization of the matter power spectrum (σ_8), and dark energy (see e.g., White et al., 1993; Eke et al., 1996; Kitayama & Suto, 1997; Haiman et al., 2001; Voit, 2005; Vikhlinin et al., 2009; Mantz et al., 2010; Rozo et al., 2010; Allen et al., 2011; Oguri & Takada, 2011; Weinberg et al., 2013; Planck Collaboration et al., 2016b). Also, observations on galaxy clusters are useful to test the paradigm of CDM. Recent gravitational lensing analyses have shown that the radial density profile (e.g., Umetsu et al., 2011) and the degree of non-sphericity (e.g., Oguri et al., 2010) of massive galaxy clusters are in good agreement with the expectations from the ΛCDM model within error-bars. Observations on bullet galaxy cluster have also ruled out a regime of self-interactions in dark matter (e.g., Markevitch et al., 2004) as a test of collisionless nature of CDM, from maps of hot gas, dark matter revealed by gravitational lensing effects, and galaxies of a galaxy cluster with a high-velocity merger.

Galaxy clusters can be observationally identified in optical, X-ray, and radio/mm/submm wavelengths. In optical images, one of the most striking features within galaxy clusters is the presence of a larger number of red and elliptical galaxies with little ongoing star formation (Oemler, 1974; Dressler, 1980; Dressler & Gunn, 1983; Balogh et al., 1997; Poggianti et al., 1999), exhibiting a tight relation in the color-magnitude diagram called red-sequence (e.g., Stanford et al., 1998). These quenching effects are expected from intra-

cluster astrophysical processes, including tidal disruption, harassment, strangulation (Larson et al., 1980), and ram-pressure stripping (Gunn & Gott, 1972), or from the age-matching model (e.g., Hearin et al., 2014) which employs expectations that galaxies in larger overdensities form earlier. The recent development of wide-field optical imaging surveys makes an optical selection of galaxy clusters based on red member galaxies (see Figure 1.2 for examples of their images) in such cluster regions particularly powerful, typically with a larger number of galaxy clusters than those selected by X-ray or radio wavelengths at present, since optical surveys take wide-field images with multiple photometric passbands from which we can select clusters of galaxies efficiently via the enhancement of red-sequence galaxy number counts in such cluster regions and derive photometric redshifts of clusters from colors affected by the 4000Å break (e.g., Gladders & Yee, 2000).

There are several optical cluster-finding algorithms based on the red-sequence galaxies for cluster selection in multi-band optical data and richness estimation for each galaxy cluster. Recently, CAMIRA[1](Oguri, 2014; Oguri et al., 2018a) and redMaPPer[2](Rykoff et al., 2012, 2014; Rozo & Rykoff, 2014; Rozo et al., 2015a,b; Rykoff et al., 2016) cluster-finding algorithms have often been employed to construct optically selected cluster catalogs to study the physical properties of galaxy clusters. We refer to Appendix A for more details. The main difference between the redMaPPer and CAMIRA cluster-finding algorithms is that CAMIRA subtracts the background galaxy levels to estimate the richness in cluster selection locally, but redMaPPer does this globally. Moreover, CAMIRA employs a larger aperture size ($\simeq 1h^{-1}$Mpc in physical coordinates) independent of richness values in cluster selections, whereas redMaPPer uses a smaller richness-dependent aperture ($< 1h^{-1}$Mpc in physical coordinates for almost all clusters).

Since theoretical predictions of galaxy cluster observables are primarily determined with respect to the halo mass for a given cosmological model, we need a valid statistical model to connect the halo mass and observed mass proxy in order to make full use of galaxy cluster samples. In optical surveys, a commonly-used mass proxy is an optical richness, which roughly corresponds to the number of red-sequence member galaxies above some luminosity threshold in each galaxy cluster (e.g., Rozo et al., 2009). Well-calibrated and unbiased mass-richness relations allow us to infer galaxy cluster masses from observed richness values. Based on the same optical imaging data used for galaxy cluster selections, weak gravitational lensing provides a powerful means to constrain mass-observable relations of galaxy clusters. It is the deflection of light due to the intervening matter density field along the line-of-sight direction to produce a coherent distortion pattern in background galaxy shapes (for reviews, see e.g., Bartelmann & Schneider, 2001; Kilbinger, 2015; Mandelbaum, 2018b). Stacked weak lensing measurements statistically probe the projected average mass distribution of galaxy clusters with equal sensitivity to the dark and baryonic matter (see Appendix B for more details). Stacking shapes of background galaxies for a sample of galaxy clusters enhances the signal-to-noise ratio of the measurements. Previous studies have utilized the weak gravitational lensing effect to constrain mass-observable relations, including mass-richness relations (e.g., Johnston et al., 2007;

[1]Cluster finding algorithm based on Multi-band Identification of Red sequence gAlaxies
[2]red-sequence Matched-filter Probabilistic Percolation

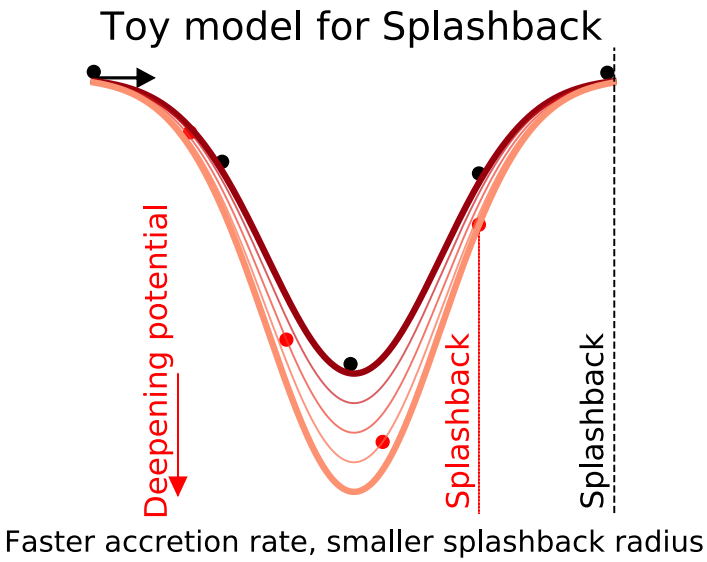

Figure 1.3 Schematic figure for physics of the splashback radius (courtesy of Surhud More, not from published papers). The horizontal axis shows a radial distance from a halo located at the center of this figure. The vertical axis denotes the gravitational potential of this halo system. A black point on the left side with a black arrow presents an infalling object such as dark matter or a galaxy. Without deepening the potential, the energy for the object conserves, and the object reaches the black point on the right side with the same potential as one at the start of infalling. On the other hand, when gradually deepening potential from other accreting materials (red colors) like the red arrow, the potential of the object has an explicit time-dependence. Thus, the energy for this object does not conserve. As a result, this object turns around (splashback) at a radius with a smaller potential than one at the start of infalling. From these physical points, dark matter halos with faster accretion rate have smaller splashback radii, and accretion rate statistically depends on halo mass.

Leauthaud et al., 2010; Okabe et al., 2013; von der Linden et al., 2014; Hoekstra et al., 2015; Battaglia et al., 2016; Simet et al., 2017; Melchior et al., 2017; Murata et al., 2018; Medezinski et al., 2018a; Miyatake et al., 2019; McClintock et al., 2019). Constraining this mass-richness relation via weak gravitational lensing is fundamentally important to connect theories or simulations with observations on galaxy clusters, since the halo mass determine the physical properties dominantly such as density profiles of dark matter halos and galaxy evolution and formation physics. Also, constraining the mass distribution function of dark matter halos at galaxy cluster mass scales leads to cosmological parameter estimations.

1.3 The observed inconsistency with the ΛCDM model in the splashback radius of optically selected galaxy clusters

The splashback radius has been recently proposed as a physical boundary of dark matter halos at the outskirts which separates orbiting from accreting materials (e.g., dark matter particles and galaxies in subhalos) as a sharp density edge, which is seen even after stacking of halos through numerical high-resolution N-body simulations (Diemer & Kravtsov, 2014; More et al., 2015) and a semi-analytic model

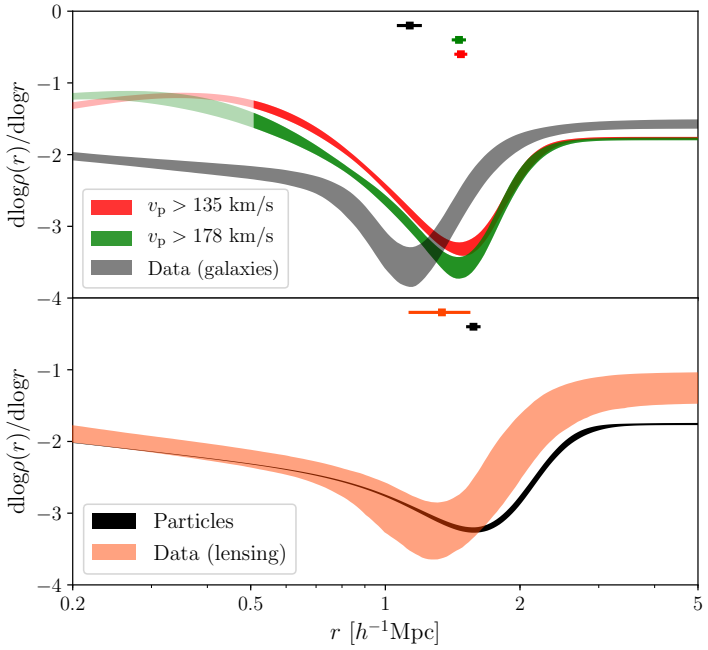

Figure 1.4 Comparison of the three-dimensional splashback radius from model predictions under the ΛCDM model and real data in Chang et al. (2018) from the DES redMaPPer optically selected cluster catalog. The top panel shows that the measurement denoted by "Data (galaxies)" in black color from projected galaxy profiles is $\sim 20\%$ smaller their model predictions in red or green colors, as found by More et al. (2016) for the first time with the SDSS redMaPPer clusters. In the bottom panel, Chang et al. (2018) also exhibits a comparison with lensing profiles for the splashback radius with a lower signal-to-noise ratio, which we do not perform in this thesis. This figure is reproduced from Figure 8 in Chang et al. (2018).

(Adhikari et al., 2014). At the splashback radius, the logarithmic derivative of density profiles is predicted to drop significantly over a narrow range of radius in the outskirts due to the piling up of materials with small radial velocities at their first orbital apocenter after infall into halos (refer to Figure 1 of Adhikari et al., 2014, for the phase diagram of dark matter halos in simulations, which demonstrates that orbiting and accreting materials are well separated at the splashback radius). Previous density model profiles such as the Navarro-Frenk-White (NFW; Navarro et al., 1996) model profile cannot reproduce such features (Diemer & Kravtsov, 2014). The splashback radius primarily depends on accretion rate, redshift, and halo mass (e.g., Diemer et al., 2017). When the gravitational potential deepens during the particle orbit due to mass accretion on to the halo, particles do not reach as far out: the larger the accretion rate, the smaller the splashback radius. The secondary infall models with the spherical collapse model (Gunn & Gott, 1972) predict such sharp density edge semi-analytically (e.g., Fillmore & Goldreich, 1984; Bertschinger, 1985; Adhikari et al., 2014; Shi, 2016), and thus splashback radius locations can be predicted approximately from simple dynamics in gravitational potentials of dark matter halos with an explicit evolving time-dependence due to accreting materials. Furthermore, the splashback features have been investigated from various aspects with simulations (Mansfield et al., 2017; Diemer, 2017; Okumura et al., 2018; Sugiura et al., 2019; Xhakaj et al., 2019), including dark energy (Adhikari et al., 2018), modified gravity (Adhikari et al., 2018; Contigiani et al., 2019b), and self-interacting dark matter (Banerjee et al., 2019). For reference, we show a schematic

figure for a toy model of the splashback radius in Figure 1.3.

Observationally, the splashback feature has been detected and constrained statistically for galaxy clusters selected by the optical cluster-finding algorithm redMaPPer through cross-correlation measurements between clusters and galaxies (More et al., 2016; Baxter et al., 2017; Chang et al., 2018; Shin et al., 2019) or weak lensing measurements (Chang et al., 2018) with high precisions thanks to a large number of optically selected clusters. Less precise measurements with a smaller number of galaxy clusters have also been done for clusters selected by the Sunyaev–Zel'dovich effects (Zürcher & More, 2019; Shin et al., 2019) or by X-ray flux (Umetsu & Diemer, 2017; Contigiani et al., 2019a). We note that the signal-to-noise ratios for weak lensing measurements are smaller than those for cluster-galaxy cross-correlation measurements to constrain the splashback feature. It is important to validate theoretical predictions against observed splashback features with the help of weak lensing mass calibrations, where weak lensing measurements constrain mass-observable relation (e.g., mass-richness relation for optically-selected clusters) mainly from their amplitudes, instead of the location of the splashback radius imprinted in lensing measurements. Interestingly, the measurements of the splashback radius with high precision for the redMaPPer clusters (More et al., 2016; Baxter et al., 2017; Chang et al., 2018) from the Sloan Digital Sky Survey (SDSS) or the Dark Energy Survey (DES) data show that their observed splashback radius from cluster-galaxy cross-correlation measurements is smaller than expectations from *N*-body simulations under the ΛCDM cosmology at the level of $20\% \pm 5\%$. Shin et al. (2019) also show a similar trend at $\sim 2\sigma$ level for the redMaPPer clusters at more massive mass scale. We refer to Figure 1.4, which is reproduced from Chang et al. (2018), for a summary plot of the inconsistency found in Chang et al. (2018).

One of the possible origins of the inconsistency is some systematics in the optical cluster-finding algorithm, such as projection effects in optical cluster finding algorithms that are misidentifications of non-member galaxies along the line-of-sight direction as member galaxies in optical richness estimation (e.g., Cohn et al., 2007; Zu et al., 2017; Busch & White, 2017; Costanzi et al., 2019; Sunayama & More, 2019). In particular, Busch & White (2017) and Sunayama & More (2019) investigated projection effects on the splashback features with a simplified redMaPPer-like optical cluster-finding algorithm in the Millennium Simulation (Springel et al., 2005), although their cluster abundance densities in the simulations is ~ 3 times larger than observations as a function of richness mainly due to their mock galaxy populations for the mock cluster finders, which may lead to the overestimate of the projection effects. Also, Busch & White (2017) and Sunayama & More (2019) did not follow a procedure in the observational studies (e.g., More et al., 2016; Chang et al., 2018) explicitly to estimate the three-dimensional splashback radius from projected cross-correlation functions with a model profile proposed in Diemer & Kravtsov (2014). Therefore, we can improve this aspect in mock simulation analyses to investigate possible bias effects from optical cluster-finding algorithms by more closely resembling the comparison procedure in the observations. Thus, further independent investigation would be useful to confirm whether the inconsistency is caused by artifacts due to optical cluster-finding algorithms or not.

Another interesting possible origin of the inconsistency is new physics beyond the standard ΛCDM model, such as self-interacting dark matter. Non-gravitational interactions between dark matter have been proposed to explain various observables with some tensions on cluster and galaxy group scales. Models for the cross-section can depend on the relative velocity of dark matter and the scattering angle. Their effects on the splashback radius are investigated in Banerjee et al. (2019) with numerical cosmological simulations as mentioned above. Banerjee et al. (2019) show that the self-interactions between dark matter can macroscopically alter the distribution of subhalos (i.e., galaxies) and the density of dark matter even around the splashback radius. First, self-interacting dark matter can produce a cumulative drag, causing subhalos (i.e., galaxies) to lose energy and turn around before reaching the ΛCDM splashback radius (i.e., smaller splashback radius than expectations under the ΛCDM model). Second, Banerjee et al. (2019) show that self-interacting dark matter could preferentially disrupt subhalos (i.e., galaxies) which would otherwise have had the largest apocenters (i.e., splashback radius), since such subhalos move around halo centers with larger forces from self-interacting dark matter than the ΛCDM scenario. As a result, the splashback radius can be smaller than expectations from ΛCDM. Additionally, models with anisotropic scattering could have qualitatively different and more significant effects compared to those with isotropic scattering, since anisotropic scattering can lead to a coherent drag force on accreting materials (e.g., dark matter and galaxies) on to galaxy clusters. In particular, Banerjee et al. (2019) show that, under a relative higher cross-section for anisotropic scattering compared to constraints from Bullet clusters, the splashback radius of subhalos (i.e., galaxies) could be shifted to the 20% smaller value than that from the ΛCDM model at a fixed cluster mass bin, to explain the observed inconsistency in the redMaPPer clusters in the literature (More et al., 2016; Chang et al., 2018).

The distribution of galaxies after magnitude or color cuts in observations is expected to have the same splashback radius as dark matter distribution to the first order approximation unless such cuts select particular orbits of recently accreted galaxies in clusters due to fast quenching effects for instance, since dynamics of galaxies are expected to follow dark matter distribution in the outskirts based on gravitational potentials dominantly determined by the larger amount of dark matter. The difference between dark matter and subhalos, where galaxies should reside, can be caused by dynamical friction (Chandrasekhar, 1943) that affects subhalos with a mass ratio to host halo mass $M_{\rm sub}/M_{\rm host} \gtrsim 0.01$ (Adhikari et al., 2016) to lead to a net orbital energy loss by an effective drag force via gravitational interaction with nearby matter to decrease splashback radii significantly ($\gtrsim 5\%$) compared to the dark matter. In observations, fainter galaxies are expected to live in less massive subhalos, and thus dynamical friction effects are smaller. Hence, fainter galaxies are expected to have splashback radii closer to those for the dark matter. However, relations between subhalo masses and galaxy luminosities (including scatter between them) have not been fully understood. Dynamical friction effects on splashback radii are investigated in the literature (More et al., 2016; Chang et al., 2018; Zürcher & More, 2019) with different absolute magnitude thresholds, but a magnitude dependence of splashback radii for massive clusters has not been detected even with smaller

error bars in More et al. (2016) at a $\lesssim 5\%$ precision level, despite the fact that a $\gtrsim 5\%$ shift of splashback radii is expected in simulations especially for more massive subhalos when selecting subhalos with maximum circular velocities throughout their entire history to reproduce galaxy abundances in observations (More et al., 2016; Chang et al., 2018). The scatter between the maximum circular velocities (or subhalo masses) and galaxy luminosities could wash out dynamical friction effects (More et al., 2016). It would be interesting to explore dynamical friction effects with an independent optical cluster-finding algorithm and fainter galaxy samples.

Also, quenching of satellite galaxies (i.e., a transition of blue to red galaxies) at the outskirts of galaxy clusters has been investigated (e.g., Wetzel et al., 2013; Fang et al., 2016; Zinger et al., 2018; Adhikari et al., 2019). The splashback radius separates orbiting from accreting galaxies as the physical boundary of halos, and thus investigating relations between the splashback and quenching features around clusters over a wide range of redshift would be informative to constrain galaxy formation and evolution physics.

1.4 The wide field-of-view and deep optical imaging survey of Subaru Hyper Suprime-Cam

Given the smaller number of such massive dark matter halos in which galaxy clusters reside, we require deep imaging data from wide field-of-view surveys to investigate the statistical properties of galaxy clusters over a wide redshift range. Ongoing and upcoming wide-field optical or infrared galaxy surveys allow us to study galaxy clusters in great detail if systematic errors are under control, including the Kilo-Degree Survey (KiDS; de Jong et al., 2013; Kuijken et al., 2015) and the DES (Flaugher, 2005; Dark Energy Survey Collaboration et al., 2016) for ongoing surveys, and the Large Synoptic Survey Telescope (LSST; Ivezić et al., 2008), *Euclid* (Laureijs et al., 2011), and *Wide-Field Infrared Survey Telescope* (*WFIRST*; Spergel et al., 2015) for upcoming surveys.

The Hyper Suprime-Cam Subaru Strategic Program (HSC-SSP) is also such an ongoing wide-field optical imaging survey (Miyazaki et al., 2012, 2015, 2018a; Komiyama et al., 2018; Furusawa et al., 2018; Kawanomoto et al., 2018; Aihara et al., 2018a,b, 2019) with a 1.77 deg^2 field-of-view camera on the 8.2 m Subaru telescope. Compared to the other ongoing surveys, the HSC-SSP survey is unique in its combination of depth and high-resolution image quality, which allows us to detect galaxy clusters over a wide redshift range up to $z_{\mathrm{cl}} \sim 1$, to measure stacked lensing profiles around such high-redshift clusters with a lower shape noise than that of other ongoing surveys such as KiDS and DES (see Table 2 in Hikage et al., 2019, for more details), and to investigate their splashback features with photometric galaxies down to fainter apparent magnitudes, although the survey area is smaller than those of other imaging surveys. The HSC *grizy* broadband filters are shown in Figure A.1.

In this thesis, since the CAMIRA optically selected clusters based on the HSC-SSP data are available

(Oguri et al., 2018a), we employ these CAMIRA clusters to investigate the statistical properties on the mass-richness relation and the splashback radius. The HSC-SSP data catalogs for the CAMIRA clusters, weak lensing shear, photometric redshifts, and photometric galaxies employed in this thesis are at present or will soon be available at websites.[3][4]

1.5 Plan of this thesis

The main physical motivation of this thesis is to reveal whether the observed inconsistency of the splashback radius in redMaPPer optically selected galaxy clusters in the literature is actually caused by new physics beyond the established standard ΛCDM cosmological model, such as non-gravitational self-interaction of dark matter, or not. It is fundamentally essential to test the validity of the ΛCDM cosmological model from the recently proposed physical boundary of galaxy clusters, the splashback radius, for understanding the physical aspects of the Universe.

For this purpose, in this thesis, we present observational and statistical studies of the CAMIRA optically selected clusters at $0.1 < z_{\rm cl} < 1.0$ thanks to deep HSC images, on the mass-richness relation with weak gravitational lensing effects and the splashback radius with simplified mock simulation analyses to investigate selection bias effects in the CAMIRA and redMaPPer optical cluster-finding algorithms, whereas previous works on the mass-richness relation and the splashback radius are limited to $z_{\rm cl} \lesssim 0.7$ even for DES (McClintock et al., 2019; Chang et al., 2018). Our study in this thesis is the first study with detections of the splashback radius in clusters selected by the CAMIRA cluster-finding algorithm, whereas all the previous works of optically selected galaxy clusters with the inconsistency of the smaller splashback radius locations are based on the redMaPPer cluster-finding algorithm (More et al., 2016; Chang et al., 2018; Shin et al., 2019).

The outline of this thesis is as follows:

- In Chapter 2, we constrain the mass-richness relation of the HSC CAMIRA clusters with weak gravitational lensing and abundance measurements. This chapter is based on a published work of Murata et al. (2019).

- In Chapter 3, we investigate the splashback radius of the HSC CAMIRA clusters with projected cross-correlation function measurements between the clusters and HSC photometric galaxies with the help of our mass-richness relation presented in Chapter 2. We also employ simplified mock simulation analyses to investigate the selection bias effects of the CAMIRA and redMaPPer algorithms on the observed splashback radius. This chapter is based on Murata et al. (2020), which we have submitted to Publications of the Astronomical Society of Japan and arXiv[5].

[3] https://hsc-release.mtk.nao.ac.jp/doc/
[4] https://www.slac.stanford.edu/~oguri/cluster/
[5] https://arxiv.org/abs/2001.01160

- In Chapter 4, we summarize our main findings and conclude.

1.6 Convention and unit

Throughout this thesis, we use natural units where the speed of light is set equal to unity, $c = 1$.

We use $M \equiv M_{200\mathrm{m}} = 4\pi(R_{200\mathrm{m}})^3\bar{\rho}_{\mathrm{m0}} \times 200/3$ for the halo mass definition, where $R_{200\mathrm{m}}$ is the three-dimensional comoving radius within which the mean mass density is 200 times the present-day mean mass density, $\bar{\rho}_{\mathrm{m0}}$. In this thesis, we use a radius and density in comoving coordinates rather than in physical coordinates unless otherwise stated.

We adopt the flat ΛCDM model as the fiducial cosmological model with the parameters from the *Planck15* (hereafter the *Planck*) result (Planck Collaboration et al., 2016): $\Omega_{\mathrm{b0}}h^2 = 0.02225$ and $\Omega_{\mathrm{c0}}h^2 = 0.1198$ for the density parameters of baryon and cold dark matter, respectively, $\Omega_\Lambda = 0.6844$ for the cosmological constant, $\sigma_8 = 0.831$ for the normalization of the matter fluctuation, and $n_s = 0.9645$ for the spectral index. In Chapter 2, we also use cosmological parameters consistent with those from *WMAP9* (hereafter the *WMAP*) results (Hinshaw et al., 2013) to compare with the results of the mass-richness relation when assuming the *Planck* cosmological parameters: $\Omega_{\mathrm{b0}}h^2 = 0.02254$, $\Omega_{\mathrm{c0}}h^2 = 0.1142$, $\Omega_\Lambda = 0.721$, $\sigma_8 = 0.82$, and $n_s = 0.97$. As shown in Figure 1.1, these best-fit values of Ω_{m0} and σ_8 for the *Planck* model are larger than those for the *WMAP* model. Thus, the dark matter halo mass function for the *Planck* model is larger than that for the *WMAP* model at high mass scales due to larger density amounts of matters and larger density fluctuations to make halos more efficiently for the *Planck* model.

For reference, we write down the unit of length and mass in this thesis as $1\ \mathrm{Mpc} = 10^6\mathrm{pc} = 3.086\times10^{22}\mathrm{m}$ and $M_\odot = 1.988 \times 10^{30}\mathrm{kg}$.

We employ the convention in More et al. (2015, 2016) for the splashback radius as in all the previous observational works in the literature, where $r_{\mathrm{sp}}^{\mathrm{3D}}$ and $R_{\mathrm{sp}}^{\mathrm{2D}}$ correspond to the locations of the steepest logarithmic derivative of the radially averaged density profiles after stacking of halos in the three-dimensional or projected space, respectively, due to its accessibility in observations, whereas the different definition of the splashback radius are employed from dynamics of dark matter particles in simulations (Mansfield et al., 2017; Diemer, 2017) with a small difference from our convention.

Chapter 2

The mass-richness relation of optically selected clusters from weak gravitational lensing and abundance with Subaru HSC first-year data

2.1 Overview

In this chapter, we present constraints on the relation between the optical richness and halo mass of optically-selected HSC clusters in the redshift range $0.1 \leq z_{\rm cl} \leq 1.0$ (Oguri et al., 2018a) detected by the CAMIRA cluster-finding algorithm (Oguri, 2014). For this purpose, we conduct a joint analysis of the abundance and stacked lensing profiles from the first-year data catalogs of the Subaru HSC-SSP survey. For this work, we adapt and apply a pipeline developed in Murata et al. (2018), which was used for clusters at $0.1 \leq z_{\rm cl} \leq 0.33$ in the SDSS selected by the redMaPPer cluster-finding algorithm. We model the probability distribution of the richness for a given halo mass and redshift $P(\ln N|M,z)$ without informative prior distributions for richness-mass parameters. We then use Bayes theorem to calculate the mass-richness relation $P(\ln M|N)$ in each redshift bin. In order to accurately model the abundance and stacked lensing profiles, we use Dark Emulator (Nishimichi et al., 2019), which is constructed from a suite of high-resolution N-body simulations. We employ an analytic model for the covariance matrix describing statistical errors for the abundance and stacked lensing profiles. We validate the analytic covariance matrix against realistic mock shear and halo catalogs (Shirasaki et al., 2019).

The structure of this chapter is as follows. In Chapter 2.2, we briefly describe the Subaru HSC data and catalogs used in our richness-mass relation analysis. In Chapter 2.3, we describe measurements of the

cluster abundance and stacked cluster lensing profiles. In Chapter 2.4, we summarize model ingredients for our richness-mass relation analysis. In Chapter 2.5, we show the resulting constraints on the mass-richness relation. We discuss the robustness of our results in Chapter 2.6. We summarize in Chapter 2.7.

2.2 HSC first-year dataset

2.2.1 HSC-SSP survey

With its unique combination of a wide field-of-view, a large aperture of the primary mirror, and excellent image quality, HSC enables us to measure lensing signals out to a relatively high redshift. Under the HSC-SSP, the HSC is conducting a multi-band wide-field imaging survey over six years with 300 nights of Subaru time. The HSC-SSP survey consists of three layers: Wide, Deep, and UltraDeep. The Wide layer is designed for weak lensing science and aims at covering 1400 deg^2 of the sky with five broad bands, *grizy*, with a 5σ point-source depth of $r \sim 26$. The i-band images are taken when the seeing is better since i-band images are used for galaxy shape measurements for weak lensing analysis, resulting in a median point-spread function (PSF) full width at half maximum of $\sim 0.''58$ for i-band images for the HSC first-year shear catalog described in Chapter 2.2.3. The software pipelines that reduce the data are described in Bosch et al. (2018).

While the HSC-SSP Data Release 1 (Aihara et al., 2018b) is based on data taken on 61.5 nights between March 2014 and November 2015, in this chapter, we use HSC cluster, lensing shear, and photometric redshift catalogs based on the S16A internal release data of the HSC-SSP survey that was taken during March 2014 through April 2016, about 90 nights in total.

2.2.2 HSC CAMIRA cluster catalog

We use the CAMIRA cluster catalog from the S16A internal release data of the HSC-SSP Wide dataset presented in Oguri et al. (2018a), which was constructed using the CAMIRA algorithm (Oguri, 2014). In this chapter, we use the cluster catalog without applying a bright-star mask (Oguri et al., 2018a).

The catalog contains 1921 clusters of $0.1 \leq z_{\rm cl} \leq 1.1$ and richness $N \geq 15$ with almost uniform completeness and purity over the sky region. We use 1747 CAMIRA clusters with $15 \leq N \leq 200$ and $0.1 \leq z_{\rm cl} \leq 1.0$. The total area for the CAMIRA clusters is estimated to be $\Omega_{\rm tot} = 232.8$ deg^2 (Oguri et al., 2018a), which is larger than the area for the lensing shear catalog presented in Chapter 2.2.3. The CAMIRA algorithm calculates the mask area fraction $f_{\rm mask}$ to correct for the richness and adopts the minimum mask fraction value to reject detections (Oguri, 2014). Thus areas for clusters with lower redshifts are slightly smaller since the richness is defined within a circular aperture with a radius $R \lesssim 1\ h^{-1}$Mpc in physical coordinates and clusters at lower redshift have a higher rejection rate from the mask cut. We use a random catalog to estimate this effect by injecting clusters at the catalog level into the footprint to calculate the rejection rate from the masking cut as a function of cluster redshift. We then define a weighting function

to quantify the masking effect as

$$w_{\rm rand}(z_{\rm cl}) = \frac{n_{\rm sample}(z_{\rm cl})}{n_{\rm keep}(z_{\rm cl})}, \tag{2.1}$$

where $n_{\rm sample}(z_{\rm cl})$ and $n_{\rm keep}(z_{\rm cl})$ are the number of injected clusters and the number of clusters not rejected by the masking cut, respectively (similarly defined in Murata et al., 2018). In addition, we define the effective area of the CAMIRA cluster catalog at a given redshift as

$$\Omega_{\rm eff}(z_{\rm cl}) = \frac{\Omega_{\rm tot}}{w_{\rm rand}(z_{\rm cl})}, \tag{2.2}$$

to account for the detection efficiency as a function of redshift in measurements below, although this effect is not very large for the CAMIRA clusters with $w_{\rm rand}(z_{\rm cl} = 0.1) = 1.02$ at most. Here we note that $\Omega_{\rm eff}(z_{\rm cl}) \leq \Omega_{\rm tot}$. We use the same random catalog to measure lensing signals for the subtraction of systematics in Chapter 2.3.2.

2.2.3 HSC weak lensing shear catalog

We employ the HSC first-year shear catalog (Mandelbaum et al., 2018a,c) based on the S16A internal release data for weak lensing measurements around HSC CAMIRA clusters described in Chapter 2.2.2. The galaxy shapes are measured on coadded i-band images with the re-Gaussianization moment-based method (Hirata & Seljak, 2003) and fully described in Mandelbaum et al. (2018c)[1]. This method has been applied extensively to SDSS data, and thus the systematics of the method are well understood (Mandelbaum et al., 2005; Reyes et al., 2012; Mandelbaum et al., 2013). Both shape uncertainties and biases are estimated per galaxy with simulations created using an open source software package GalSim (Rowe et al., 2015) with galaxy samples from the *Hubble Space Telescope* COSMOS survey (see Mandelbaum et al., 2018c, for more details). More specifically, Mandelbaum et al. (2018c) estimate multiplicative bias m, additive bias (c_1, c_2), intrinsic root-mean-square ellipticity $e_{\rm rms}$, and shape measurement error σ_e for the galaxy ensemble in the simulation, and define interpolation functions to produce an estimate of that quantity for each galaxy in the real data. The systematic uncertainty in the overall shear calibration is estimated to be 0.01 in Mandelbaum et al. (2018c).

Mandelbaum et al. (2018a) applied a number of cuts to satisfy the requirements for carrying out first-year weak lensing cosmology analyses. For example, the catalog is constructed using regions of sky with approximately full depth in all five bands to ensure the homogeneity of the sample. Mandelbaum et al. (2018a) also limited the `cmodel` magnitude (see Bosch et al., 2018, for the definition of `cmodel` magnitude) with $i_{\rm cmodel} < 24.5$, which is conservative compared to the i-band magnitude limit of $\sim$26.4 (5σ for point sources; Aihara et al., 2018a). As a result, the first-year shear catalog covers $\Omega_{\rm lens} = 136.9$ deg^2 in total with six distinct fields (XMM, GAMA09H, GAMA15H, HECTOMAP, VVDS, and WIDE12H). We note

[1] In this method, galaxy shapes are defined in terms of distortion: $(e_1, e_2) = (e\cos 2\phi, e\sin 2\phi)$ with $e = (a^2 - b^2)/(a^2 + b^2)$ where a and b are the major and minor axes of galaxy shape respectively, and ϕ indicates the position angle with respect to the RA/dec coordinate system (Bernstein & Jarvis, 2002).

that the area coverage of the shear catalog is smaller than that of the CAMIRA clusters ($\Omega_{\rm tot} = 232.8$ deg^2) due to the conservative cuts for the shape measurements. Mandelbaum et al. (2018a), Oguri et al. (2018b), and Hikage et al. (2019) performed extensive null tests of the shear catalog to show that the shear catalog satisfies the requirements for HSC first-year weak lensing analyses using cosmic shear and galaxy-galaxy lensing. Even after relatively conservative cuts, the HSC first-year shear catalog includes galaxy shapes with a high source number density, 24.6 (raw) and 21.8 (effective) arcmin^{-2} (Mandelbaum et al., 2018a), which enables us to measure lensing signals around high redshift HSC CAMIRA clusters ($z_{\rm cl} \leq 1.0$).

2.2.4 HSC photometric redshift catalog

We use a photometric redshift (photo-z) catalog (Tanaka et al., 2018) for the source galaxies in Chapter 2.2.3 estimated from the S16A internal release data of the HSC five broadband photometry. In the HSC survey, several different codes are employed to estimate the photometric redshifts: a machine-learning code based on a self-organizing map (`MLZ`), a classical template-fitting code (`Mizuki`), an empirical polynomial fitting code (`DEmP`; Hsieh & Yee, 2014), an extended (re)weighing method to find the nearest neighbors in color/magnitude space from a reference spectroscopic redshift sample (`NNPZ`), a neural network code using PSF-matched aperture (afterburner) photometry (`Ephor AB`), and a hybrid code combining machine learning with template fitting (`FRANKEN-Z`; Speagle et al., 2019, Speagle et al. *in prep.*) The codes are trained, validated, and tested with spectroscopic and grism redshifts as well as COSMOS 30-band data with high accuracy photo-z (Ilbert et al., 2009; Laigle et al., 2016) in Tanaka et al. (2018). The photo-z estimation is most accurate in the range $0.2 \lesssim z \lesssim 1.5$, where the HSC filter set straddles the 4000Å break (Tanaka et al., 2018).

Among these catalogs from different codes, we choose `MLZ` as the fiducial photometric redshift catalog for the lensing measurement in Chapter 2.3.2, while we also use the other photometric redshift catalogs to check the robustness of our results to our choice of `MLZ` (see Chapter 2.6.1). In this chapter, we use the redshift probability distribution functions (PDFs), $P(z)$, and randomly (i.e., Monte Carlo) sampled point estimates drawn from the full PDFs, $z_{\rm mc}$ from Tanaka et al. (2018) for the lensing measurements and the source galaxy selection. We also use the best point estimates $z_{\rm best}$ (see section 4.2 of Tanaka et al., 2018) only for lensing covariance estimation as described in Appendix D.1. We correct for the effect of photometric redshift bias on the lensing measurements (More et al. *in prep*) using COSMOS 30-band photo-z data (see Chapter 2.3.2).

2.3 Measurement

We describe the measurement method for the cluster abundance in Chapter 2.3.1 and the stacked cluster lensing profile in Chapter 2.3.2.

2.3.1 Cluster abundance

We use the abundance of CAMIRA clusters in given richness and redshift bins as cluster observables to constrain the richness-mass relation of the clusters. We divide the CAMIRA clusters into 12 bins for the abundance measurements with four richness and three redshift bins as shown in Table 2.1. We use the point estimate of richness and redshift of the clusters to calculate the abundance (i.e., we ignore any errors in the richness estimation and the cluster photometric redshift).

We measure the abundance of the clusters in each bin corrected for the detection efficiency (Murata et al., 2018) as

$$\widehat{N}_{\alpha,\beta} = \sum_{l;N_l\in N_\alpha, z_l\in z_\beta} \frac{\Omega_{\rm tot}}{\Omega_{\rm eff}(z_l)}, \tag{2.3}$$

where N_α and z_β denote the α-th richness bin and β-th redshift bin in Table 2.1, respectively. The summation runs over all clusters in each richness and redshift bin. The factor $\Omega_{\rm tot}/\Omega_{\rm eff}$ corrects for the detection efficiency as discussed in Chapter **??**. Equation (2.3) gives an estimate of the abundance of the clusters we could observe for the survey area of $\Omega_{\rm tot}$ without the mask effect. We then do not need to include the mask effect in the model prediction given in Chapter 2.4.2.

The numbers of clusters in the α-th richness and β-th redshift bin before and after the detection efficiency correction are given in Table 2.1 by $N^{\rm uncorr}_{\alpha,\beta}$ and $\widehat{N}_{\alpha,\beta}$, respectively. The correction is less than $\sim$1% for all bins.

2.3.2 Stacked cluster lensing profile

We cross-correlate the positions of CAMIRA clusters with the shapes of background galaxies to measure the average excess mass density profile around the clusters (hereafter the stacked lensing profile). We follow the procedure in Mandelbaum et al. (2018a,c) to estimate the stacked lensing profile for a sample of CAMIRA clusters for α-th richness and β-th redshift bin in Table 2.1 as

$$\begin{aligned}\widehat{\Delta\Sigma}_{l,\alpha,\beta}(R) = \frac{1}{1+\widehat{m}_{l,\alpha,\beta}(R)} \Bigg[& \frac{1}{2\widehat{\mathcal{R}}_{l,\alpha,\beta}(R)} \\ & \times \frac{1}{N^{\alpha,\beta}_{ls}(R)} \sum_{l,s;N_l\in N_\alpha, z_l\in z_\beta} w_{ls} \left\langle \Sigma_{\rm cr}^{-1} \right\rangle^{-1}_{ls} e_+(\boldsymbol{\theta}_s) \Bigg|_{R=\chi_l|\boldsymbol{\theta}_l-\boldsymbol{\theta}_s|} \\ & - \frac{1}{N^{\alpha,\beta}_{ls}(R)} \sum_{l,s;N_l\in N_\alpha, z_l\in z_\beta} w_{ls} \left\langle \Sigma_{\rm cr}^{-1} \right\rangle^{-1}_{ls} c_+(\boldsymbol{\theta}_s) \Bigg|_{R=\chi_l|\boldsymbol{\theta}_l-\boldsymbol{\theta}_s|} \Bigg],\end{aligned} \tag{2.4}$$

where the subscripts l and s stand for *lens* (cluster) and *source*, respectively, and e_+ and c_+ are the tangential component of the source galaxy ellipticity and the additive bias with respect to the cluster center, respectively. The summation runs over all pairs of clusters and source galaxies after a source selection cut

Table 2.1 Binning scheme for the CAMIRA clusters and characteristics of each bin for the abundance and lensing measurements.*

Abundance bin	α	β	$N_{\rm min}$	$N_{\rm max}$	$\langle N\rangle$	$z_{\rm cl,min}$	$z_{\rm cl,max}$	$\langle z_{\rm cl}\rangle$	$N^{\rm uncorr}_{\alpha,\beta}$	$\widehat{N}_{\alpha,\beta}$
1	1	1	15	20	17.1	0.1	0.4	0.27	255	258.3
2	2	1	20	30	24.1	0.1	0.4	0.27	208	210.7
3	3	1	30	60	38.2	0.1	0.4	0.26	92	93.3
4	4	1	60	200	77.4	0.1	0.4	0.26	9	9.1
5	1	2	15	20	17.2	0.4	0.7	0.56	301	301.7
6	2	2	20	30	24.0	0.4	0.7	0.53	210	210.6
7	3	2	30	60	38.9	0.4	0.7	0.54	79	79.2
8	4	2	60	200	73.1	0.4	0.7	0.50	7	7.0
9	1	3	15	20	17.0	0.7	1.0	0.84	339	339.2
10	2	3	20	30	23.8	0.7	1.0	0.83	181	181.1
11	3	3	30	60	36.3	0.7	1.0	0.84	65	65.0
12	4	3	60	200	64.7	0.7	1.0	1.0	1	1.0

Lensing bin	α	β	$N_{\rm min}$	$N_{\rm max}$	$\langle N\rangle$	$z_{\rm cl,min}$	$z_{\rm cl,max}$	$\langle z_{\rm cl}\rangle$	$N^{\rm uncorr}_{\alpha,\beta}$	$\widehat{N}_{\alpha,\beta}$
1	1	1	15	20	17.1	0.1	0.4	0.27	255	258.3
2	2	1	20	30	24.1	0.1	0.4	0.27	208	210.7
3	3	1	30	200	41.7	0.1	0.4	0.26	101	102.4
4	1	2	15	20	17.2	0.4	0.7	0.56	301	301.7
5	2	2	20	30	24.0	0.4	0.7	0.53	210	210.6
6	3	2	30	200	41.6	0.4	0.7	0.53	86	86.2
7	1	3	15	20	17.0	0.7	1.0	0.84	339	339.2
8	2	3	20	30	23.8	0.7	1.0	0.83	181	181.1
9	3	3	30	200	36.7	0.7	1.0	0.84	66	66.0

* Here α and β denote the bin number for richness and redshift, respectively. Each bin is defined by $N_{\rm min}$, $N_{\rm max}$, $z_{\rm cl,min}$, and $z_{\rm cl,max}$, and $\langle N\rangle$ and $\langle z_{\rm cl}\rangle$ give the mean values of richness and redshift. $N^{\rm uncorr}_{\alpha,\beta}$ and $\widehat{N}_{\alpha,\beta}$ are the abundance measurements without and with the correction discussed in Chapter 2.3.1, respectively.

described below in a given comoving transverse separation bin of $R = \chi_l|\boldsymbol{\theta}_l - \boldsymbol{\theta}_s|$, where χ_l is the comoving distance to each cluster, and $\boldsymbol{\theta}_l$ and $\boldsymbol{\theta}_s$ are angular positions of the lenses and the sources, respectively. We use 11 radial bins that are equally spaced logarithmically from 0.42 h^{-1}Mpc to 14.0 h^{-1}Mpc in comoving coordinates. We use area-weighted mean values of comoving radii for the representative radial values. The value for the first inner bin is 0.51 h^{-1}Mpc. We do not use lensing profiles at $< 0.42h^{-1}$Mpc to avoid a possible dilution effect (Medezinski et al., 2018b) and an increased blending effect (Murata et al. *in prep.*) at such small radii.

The critical surface mass density is defined for a system of lens and source for a flat universe as

$$\Sigma_{\rm cr}^{-1}(z_l, z_s) = 4\pi G(1+z_l)\chi_l\left(1-\frac{\chi_l}{\chi_s}\right) \ (z_l \le z_s) \tag{2.5}$$

and 0 when $z_l > z_s$, where G is the gravitational constant. We average this over the source photometric redshift PDF for each lens-source pair as

$$\left\langle\Sigma_{\rm cr}^{-1}\right\rangle_{ls} = \int_{z_l}^{\infty} {\rm d}z_s \Sigma_{\rm cr}^{-1}(z_l, z_s)P(z_s). \tag{2.6}$$

In addition, the lens-source pair weight is given as

$$w_{ls} = \frac{\Omega_{\rm tot}}{\Omega_{\rm eff}(z_l)} \left\langle \Sigma_{\rm cr}^{-1} \right\rangle_{ls}^2 w_s, \tag{2.7}$$

and w_s is the source weight defined as

$$w_s = \frac{1}{\sigma_e^2 + e_{\rm rms}^2}, \tag{2.8}$$

where σ_e is the measurement error of galaxy ellipticity and $e_{\rm rms}$ is the intrinsic per-component root-mean-square ellipticity estimated in Mandelbaum et al. (2018c) for each source galaxy. The lensing weight factor $\Omega_{\rm tot}/\Omega_{\rm eff}(z_l)$ corrects for the effective area difference as a function of cluster redshift as in the abundance estimator in equation (2.3). We note that this correction to the lensing estimator is small (less than 1%) for all bins. The denominator in equation (2.4) is the weighted number of lens-source pairs in each separation bin computed as

$$N_{ls}^{\alpha,\beta}(R) = \sum_{l,s;N_l\in N_\alpha, z_l\in z_\beta} w_{ls} \Big|_{R=\chi_l|\boldsymbol{\theta}_l-\boldsymbol{\theta}_s|}. \tag{2.9}$$

The multiplicative bias correction is estimated as

$$\widehat{m}_{l,\alpha,\beta}(R) = \frac{\sum_{l,s;N_l\in N_\alpha, z_l\in z_\beta} m_s w_{ls} \Big|_{R=\chi_l|\boldsymbol{\theta}_l-\boldsymbol{\theta}_s|}}{\sum_{l,s;N_l\in N_\alpha, z_l\in z_\beta} w_{ls} \Big|_{R=\chi_l|\boldsymbol{\theta}_l-\boldsymbol{\theta}_s|}}, \tag{2.10}$$

where m_s is the estimated multiplicative bias for each source galaxy (Mandelbaum et al., 2018c). The shear responsivity factor represents the statistically-averaged response of galaxy distortions to small shears (Kaiser et al., 1995; Bernstein & Jarvis, 2002), and is measured as

$$\widehat{\mathcal{R}}_{l,\alpha,\beta}(R) = 1 - \frac{\sum_{l,s;N_l\in N_\alpha, z_l\in z_\beta} e_{\rm rms}^2 w_{ls} \Big|_{R=\chi_l|\boldsymbol{\theta}_l-\boldsymbol{\theta}_s|}}{\sum_{l,s;N_l\in N_\alpha, z_l\in z_\beta} w_{ls} \Big|_{R=\chi_l|\boldsymbol{\theta}_l-\boldsymbol{\theta}_s|}}, \tag{2.11}$$

which is found to be around 0.83 for all the bins.

Here we describe the source selection cut. As shown in e.g., Medezinski et al. (2018b), it is important to use a secure background galaxy sample for cluster weak lensing in order to minimize the dilution effect by cluster member galaxies especially at inner radii. We use the *Pcut* method (Oguri, 2014) as our fiducial background source selection cut. In the *Pcut* method, we select source galaxies whose photometric redshift PDFs lie mostly beyond the cluster redshift plus some threshold Δz: $\int_{z_l+\Delta z}^{\infty} {\rm d}z P(z) > 0.98$. We apply an additional cut on the randomly sampled redshift from PDFs, $z_{\rm mc} < 2.5$, for each lens-source pair in equa-

tion (2.4). We use $\Delta z = 0.1$ for the fiducial cut since Medezinski et al. (2018b) shows the possible dilution effect is negligible for the *Pcut* method with this threshold value at $R \gtrsim 0.5h^{-1}$Mpc. In Chapter 2.6.1, we also check the robustness of our choice of this source selection cut by using the *Pcut* method with $\Delta z = 0.2$ and the *color-color cut* in Medezinski et al. (2018b). The *color-color cut* uses the color-color space of $g-i$ vs $r-z$ for HSC, where cluster red-sequence member galaxies can be well isolated from background galaxies.

In addition, we correct for selection bias from the lower cut on the resolution factor at $R_2 = 0.3$ in the shape catalog (Mandelbaum et al., 2018c) as

$$\widehat{m}_{\mathrm{sel},l,\alpha,\beta}(R) = A_{\mathrm{sel}} p_{l,\alpha,\beta}(R_2 = 0.3; R), \tag{2.12}$$

where $A_{\mathrm{sel}} = 0.0087$ and $p_{l,\alpha,\beta}(R_2 = 0.3; R)$ is calculated by summation of lens-source weights, w_{ls}, in each of the radial, richness, and redshift bins. This correction is found to be $m_{\mathrm{sel}} \sim 0.01$ for all bins. We then correct for the redshift variation of the intrinsic shape noise (Mandelbaum et al., 2018c) by employing $m = 0.03$ for $1.0 \leq z_{\mathrm{best}} \leq 1.5$ and $m = -0.01$ for the other redshift ranges, and by averaging this over lens-source pairs in each bin. This correction is found to be a positive multiplicative bias, but less than 0.01 for all bins.

We also correct for systematic bias effects of the photometric redshift on the lensing measurements by comparing the critical surface mass density from the photometric redshift estimates against that from the accurate photometric redshifts in the COSMOS 30-band catalog (Ilbert et al., 2009; Laigle et al., 2016) with the weak lensing weight w_{ls} multiplied by a self-organizing map weight w_{SOM} which adjusts the COSMOS 30-band photo-z sample to mimic the HSC source galaxy sample (More et al. *in prep.*). We assume that the COSMOS 30-band photometric redshift estimates are sufficiently accurate due to the larger numbers of bands. This method is based on Nakajima et al. (2012) in which the method was applied to SDSS data, and was also applied in Miyatake et al. (2019) (see their equation 11 for more details). The debias factor is found to be $m \sim 0.01$ for CAMIRA clusters with $0.1 \leq z_{\mathrm{cl}} \leq 0.7$ and $m \sim 0.02$ for CAMIRA clusters with $0.7 \leq z_{\mathrm{cl}} \leq 1.0$ for the fiducial photo-z code `MLZ` and the fiducial *Pcut* with $\Delta z = 0.1$. The debias factor is similar for the other photo-z catalogs and photo-z cuts. Our result indicates that the photo-z bias correction is not very large when we average the critical surface mass density over the photo-z PDF in equation (2.6) with the *Pcut* method or the *color-color cut* for the shape catalog. We also estimate the uncertainties of these correction factors for each richness and redshift bin using the jackknife resampling technique (Efron, 1982) with ten subsamples of the COSMOS 30-band catalog, where we recalculate the SOM weight for each jackknife resampled subsample. We estimate the photo-z bias correction uncertainties as $\sigma_{\alpha,\beta,\mathrm{photoz}} \sim 0.001, 0.002, 0.004$ for $\beta = 1, 2, 3$, respectively, for the fiducial photo-z catalog and source selection cut. We note that we ignore the impact of photo-z biases, outliers, and the limited field variance of galaxies due to the small area in the COSMOS 30-band catalog, thus the uncertainties might be underestimated. These values are used for marginalization together with the

systematic uncertainty in the overall calibration of the shear $\sigma_{\rm shear} = 0.01$ (Mandelbaum et al., 2018c) in Chapter 2.4.3 [2].

After the above corrections for $\widehat{\Delta\Sigma}_{l,\alpha,\beta}(R)$, we also subtract the lensing measurement around random points as

$$\widehat{\Delta\Sigma}_{\alpha,\beta}(R) = \widehat{\Delta\Sigma}_{l,\alpha,\beta}(R) - \widehat{\Delta\Sigma}_{r,\alpha,\beta}(R), \tag{2.13}$$

where $\widehat{\Delta\Sigma}_{r,\alpha,\beta}(R)$ replaces the clusters with random points in the estimator for $\widehat{\Delta\Sigma}_{l,\alpha,\beta}(R)$. This subtraction allows us to measure the excess mass density profile with respect to the background density as stressed in Sheldon et al. (2004) and Mandelbaum et al. (2005) (also see Singh et al., 2017, for a recent detailed study). The random subtraction can also correct for an additive bias due to shear systematics including point-spread function ellipticity errors (Mandelbaum et al., 2005). We use a random catalog of the CAMIRA clusters presented in Chapter **??** with the same richness and redshift distributions as the data, and there are 100 times as many random points as real clusters in each redshift and richness bin.

2.4 Forward modeling of cluster observables

We adopt a *forward* modeling approach to model the abundance and stacked lensing profiles (e.g., Zu et al., 2014; Murata et al., 2018; Costanzi et al., 2018) for a fixed cosmological model. In this approach, we model the probability distribution of the richness for a given halo mass and redshift, $P(\ln N|M,z)$. An alternative approach models the probability distribution of halo mass for a given richness and redshift, $P(\ln M|N,z)$, as in some previous works (e.g., Baxter et al., 2016; Simet et al., 2017; Melchior et al., 2017; McClintock et al., 2019).

2.4.1 Richness-mass relation

Following Lima & Hu (2005), we assume that the probability distribution of the *observed* richness for halos with a fixed mass and redshift is given by a log-normal distribution as

$$P(\ln N|M,z) = \frac{1}{\sqrt{2\pi}\sigma_{\ln N|M,z}} \exp\left(-\frac{x^2(N,M,z)}{2\sigma^2_{\ln N|M,z}}\right), \tag{2.14}$$

where $x(N,M,z)$ models the mean relation of $\ln N$ parametrized by four model parameters, A, B, B_z, and C_z as

$$x(N,M,z) \equiv \ln N - \left[A + B\ln\left(\frac{M}{M_{\rm pivot}}\right) + B_z \ln\left(\frac{1+z}{1+z_{\rm pivot}}\right) + C_z\left[\ln\left(\frac{1+z}{1+z_{\rm pivot}}\right)\right]^2\right]. \tag{2.15}$$

[2] We note that we apply this photo-z correction for all photo-z catalogs except for `FRANKEN-Z` since we do not have the photo-z estimates for the galaxies with HSC photometry in the COSMOS 30-band catalog from `FRANKEN-Z`.

Hence $x(N, M, z) = 0$ gives the mean relation of $\ln N$ (also the median relation for N) as

$$\begin{aligned}\langle \ln N \rangle (M, z) &\equiv \int_{-\infty}^{+\infty} \mathrm{d} \ln N \; P(\ln N | M, z) \ln N \\ &= A + B \ln \left(\frac{M}{M_{\rm pivot}} \right) + B_z \ln \left(\frac{1+z}{1+z_{\rm pivot}} \right) + C_z \left[\ln \left(\frac{1+z}{1+z_{\rm pivot}} \right) \right]^2 . \end{aligned} \tag{2.16}$$

We adopt $M_{\rm pivot} = 3 \times 10^{14} h^{-1} M_\odot$ for the pivot mass scale and $z_{\rm pivot} = 0.6$ for the pivot cluster redshift. We discuss the validity of including redshift evolution parameters B_z and C_z in Chapter 2.6.3. In this work, we ignore errors on $z_{\rm cl}$ for simplicity given the small bias and scatter of the cluster redshifts (Oguri et al., 2018a) as described in Appendix A.

In addition, we assume that the scatter of the richness around the mean relation at a fixed halo mass and redshift can be parametrized by four parameters, σ_0, q, q_z, and p_z as

$$\sigma_{\ln N | M, z} = \sigma_0 + q \ln \left(\frac{M}{M_{\rm pivot}} \right) + q_z \ln \left(\frac{1+z}{1+z_{\rm pivot}} \right) + p_z \left[\ln \left(\frac{1+z}{1+z_{\rm pivot}} \right) \right]^2 . \tag{2.17}$$

We also discuss the validity of including redshift evolution parameters, q_z and p_z, in Chapter 2.6.3. We only consider the parameter regions of $\{\sigma_0, q, q_z, p_z\}$ that result in $\sigma_{\ln N | M, z} > 0$ for all halo mass and redshift for the parameter estimation. In this treatment, $\sigma_{\ln N | M, z}$ should be effectively regarded as a *total* scatter, including contributions from the intrinsic scatters, the richness measurement errors, the halo orientation effect (e.g., Dietrich et al., 2014), the projection effect (e.g., Costanzi et al., 2019), and any other source of observational scatter that may be present.

In summary, we model the richness-mass relation in equation (2.14) with eight model parameters. We constrain these parameters and check whether this model can reproduce measurements of the cluster abundance and stacked lensing profiles simultaneously with an acceptable value of $\chi^2_{\rm min}/{\rm dof}$.

2.4.2 Abundance in richness and redshift bins

Once we fix the richness-mass relation parameters of $P(\ln N | M, z)$, we can predict the abundance of CAMIRA clusters for a given cosmology. For the α-th richness bin ($N_{\alpha,\rm min} \leq N \leq N_{\alpha,\rm max}$) and the β-th redshift bin ($z_{\beta,\rm min} \leq z \leq z_{\beta,\rm max}$), the abundance of the clusters for the total survey area is given as

$$\begin{aligned} N_{\alpha,\beta} &= \Omega_{\rm tot} \int_{z_{\beta,\rm min}}^{z_{\beta,\rm max}} \mathrm{d}z \; \frac{\mathrm{d}^2 V}{\mathrm{d}z \mathrm{d}\Omega} \int_{M_{\rm min}}^{M_{\rm max}} \mathrm{d}M \; \frac{\mathrm{d}n}{\mathrm{d}M} \int_{\ln N_{\alpha,\rm min}}^{\ln N_{\alpha,\rm max}} \mathrm{d} \ln N \; P(\ln N | M, z) \\ &= \Omega_{\rm tot} \int_{z_{\beta,\rm min}}^{z_{\beta,\rm max}} \mathrm{d}z \; \frac{\chi^2(z)}{H(z)} \int_{M_{\rm min}}^{M_{\rm max}} \mathrm{d}M \; \frac{\mathrm{d}n}{\mathrm{d}M} \, S(M, z | N_{\alpha,\rm min}, N_{\alpha,\rm max}), \end{aligned} \tag{2.18}$$

where $\chi^2(z)/H(z)$ denotes the comoving volume per unit redshift interval and unit steradian, and $\mathrm{d}n/\mathrm{d}M$ is the halo mass function at redshift z for a fixed cosmological model. The selection function of halo mass at a fixed redshift in the richness bin is calculated by integrating the log-normal distribution of $P(\ln N | M, z)$

over the richness range as

$$\begin{aligned} S(M,z|N_{\alpha,\min},N_{\alpha,\max}) &\equiv \int_{\ln N_{\alpha,\min}}^{\ln N_{\alpha,\max}} \mathrm{d}\ln N\ P(\ln N|M,z) \\ &= \frac{1}{2}\left[\mathrm{erf}\left(\frac{x(N_{\alpha,\max},M,z)}{\sqrt{2}\sigma_{\ln N|M,z}}\right) - \mathrm{erf}\left(\frac{x(N_{\alpha,\min},M,z)}{\sqrt{2}\sigma_{\ln N|M,z}}\right)\right], \end{aligned} \tag{2.19}$$

where $\mathrm{erf}(x)$ is the error function.

2.4.3 Stacked cluster lensing profile in richness and redshift bins

The stacked lensing profile of halos with mass M at redshift z_l probes the average radial profile of the matter distribution around halos, $\rho_{\rm hm}(r;M,z_l)$. Assuming statistical isotropy in the cluster detections, the average matter distribution around the halos is one-dimensional as a function of separation from the halo center r, where r is in comoving coordinates. We express the average matter density profile with the cross-correlation function between the halo distribution and the matter density fluctuation field, $\xi_{\rm hm}(r;M,z_l)$, as

$$\rho_{\rm hm}(r;M,z_l) = \bar{\rho}_{\rm m0}\left[1+\xi_{\rm hm}(r;M,z_l)\right]. \tag{2.20}$$

We note that we use the present-day mean matter density, $\bar{\rho}_{\rm m0}$, since we use the comoving density. The cross-correlation function is connected to the cross-power spectrum, $P_{\rm hm}(k;M,z_l)$, via the Fourier transform as

$$\xi_{\rm hm}(r;M,z_l) = \int_0^\infty \frac{k^2\mathrm{d}k}{2\pi^2}\ P_{\rm hm}(k;M,z_l) j_0(kr), \tag{2.21}$$

where $j_0(x)$ is the zeroth-order spherical Bessel function. The surface mass density profile is obtained from a projection of the three-dimensional matter profile along the line-of-sight direction as

$$\begin{aligned} \Sigma(R;M,z_l) &= \bar{\rho}_{\rm m0}\int_{-\infty}^{\infty}\mathrm{d}\chi\ \xi_{\rm hm}\left(r=\sqrt{R^2+\chi^2};M,z_l\right) \\ &= \bar{\rho}_{\rm m0}\int_0^\infty \frac{k\mathrm{d}k}{2\pi}\ P_{\rm hm}(k;M,z_l)J_0(kR), \end{aligned} \tag{2.22}$$

where $J_0(x)$ is the zeroth-order Bessel function and R is the projected separation from the halo center in comoving coordinates. The excess surface mass density profile around halos, which is the direct observable from the stacked cluster lensing measurement, is given as

$$\begin{aligned} \Delta\Sigma(R;M,z_l) &= \langle\Sigma(R;M,z_l)\rangle_{<R} - \Sigma(R;M,z_l) \\ &= \bar{\rho}_{\rm m0}\int_0^\infty \frac{k\mathrm{d}k}{2\pi}\ P_{\rm hm}(k;M,z_l)J_2(kR), \end{aligned} \tag{2.23}$$

where $\langle\Sigma(R;M,z_l)\rangle_{<R}$ is the average of $\Sigma(R;M,z_l)$ within a circular aperture of radius R, and $J_2(x)$ is a second-order Bessel function.

We can compute the model prediction for the stacked lensing profile accounting for the distribution of halo masses and redshifts for CAMIRA clusters in the α-th richness and β-th redshift bin as

$$\begin{aligned}\Delta\Sigma_{\alpha,\beta}(R) &= \frac{1}{N_{\Delta\Sigma}^{\alpha,\beta}}\int_{z_{\beta,\min}}^{z_{\beta,\max}}\mathrm{d}z\frac{\chi^2(z)}{H(z)}w_l^{\alpha,\beta}(z)\int_{M_{\min}}^{M_{\max}}\mathrm{d}M\ \frac{\mathrm{d}n}{\mathrm{d}M}S(M,z|N_{\alpha,\min},N_{\alpha,\max}) \\ &\quad\times\Delta\Sigma(R;M,z)\left[1+\left\langle\frac{1}{\Sigma_{\rm cr}}\right\rangle_{\alpha,\beta}(R)\ \Sigma(R;M,z)\right]. \end{aligned} \tag{2.24}$$

The term in square brackets accounts for the non-linear contribution of reduced shear, which might not be negligible at very small radii (e.g., Johnston et al., 2007), where $\langle 1/\Sigma_{\rm cr}\rangle_{\alpha,\beta}(R)$ is measured from pairs of CAMIRA clusters and source galaxies in each radial bin for the α-th richness and β-th redshift cluster bin. The lens redshift weight of $w_l^{\alpha,\beta}(z)$ is introduced to account for the weight distribution of lens redshift in the lensing measurement, and is calculated as

$$w_l^{\alpha,\beta}(z) = \sum_{l,s;N_l\in N_\alpha,z_l\in z_\beta,z_l\in z} w_{ls}. \tag{2.25}$$

More specifically, we compute $w_l^{\alpha,\beta}(z)$ as follows. First we divide the lens-source pairs into 12 lens redshift bins for each α-th richness and β-th redshift bin, which are linearly spaced in $z_l \in [z_{\beta,\min}, z_{\beta,\max}]$. We then estimate the weight in equation (2.25) over all sources in each lens redshift bin. We interpolate the weight values linearly as a function of lens redshift. The normalization factor in the denominator of equation (2.24) is similar to the abundance prediction in equation (2.18), but is defined accounting for the lens redshift weight as

$$N_{\Delta\Sigma}^{\alpha,\beta} = \int_{z_{\beta,\min}}^{z_{\beta,\max}}\mathrm{d}z\ \frac{\chi^2(z)}{H(z)}w_l^{\alpha,\beta}(z)\int_{M_{\min}}^{M_{\max}}\mathrm{d}M\ \frac{\mathrm{d}n}{\mathrm{d}M}S(M,z|N_{\alpha,\min},N_{\alpha,\max}). \tag{2.26}$$

This lens redshift weight changes the model prediction by less than 1–2% in the lensing profile amplitude compared to that without accounting for the lens redshift weight.

The identified BCGs as cluster centers can be off-centered from the true halo centers (e.g., Lin et al., 2004; Rozo & Rykoff, 2014; Oguri, 2014; Oguri et al., 2018a). We marginalize over the effect of off-centered clusters on the lensing profiles in equation (2.24) by modifying the halo-matter cross-power spectrum in equations (2.22) and (2.23) for CAMIRA clusters in the α-th richness and β-th redshift bin as

$$P_{\rm hm}(k;M,z_l) \to \left[f_{\rm cen}^{\alpha,\beta} + (1-f_{\rm cen}^{\alpha,\beta})\tilde{p}_{\rm off}(k;R_{\beta,\rm off})\right]P_{\rm hm}(k;M,z_l), \tag{2.27}$$

following Oguri & Takada (2011) and Hikage et al. (2012, 2013). Here $f_{\rm cen}^{\alpha,\beta}$ is a parameter to model the fraction of centered clusters in the α-th richness and β-th redshift bin, and $(1-f_{\rm cen}^{\alpha,\beta})$ is the fraction of off-centered clusters. While Murata et al. (2018) assigned a model parameter describing the centering fraction independently for each lensing bin, we employ an empirical parametrization $f_{\rm cen}^{\alpha,\beta}$ that depends on

the average richness and redshift in each bin (see Table 2.1) to reduce the number of model parameters as

$$f_{\rm cen}^{\alpha,\beta} = f_0 + f_N \ln\left(\frac{\langle N\rangle_{\alpha,\beta}}{N_{\rm pivot}}\right) + f_z \ln\left(\frac{1+\langle z_{\rm cl}\rangle_{\alpha,\beta}}{1+z_{\rm pivot}}\right), \tag{2.28}$$

with three model parameters (f_0, f_N, and f_z), where we use $N_{\rm pivot} = 25$ and $z_{\rm pivot} = 0.6$ and we restrict the parameter regions of f_0, f_N, and f_z such that $0 < f_{\rm cen}^{\alpha,\beta} < 1$ for all richness and redshift bins. The function $p_{\rm off}(r; R_{\beta,\rm off})$ is the normalized one-dimensional radial profile of detected centers by the CAMIRA algorithm with respect to the true halo center, for which we assume a Gaussian distribution (e.g., Johnston et al., 2007; Oguri & Takada, 2011) given as $p_{\rm off}(r; R_{\beta,\rm off}) \propto \exp(-r^2/2R_{\beta,\rm off}^2)$, where $R_{\beta,\rm off}$ is a parameter to model the typical off-centering radius in the β-th lens redshift bins. The Fourier transform of this function is denoted as $\tilde{p}_{\rm off}(k; R_{\beta,\rm off}) = \exp(-k^2 R_{\beta,\rm off}^2/2)$. Since the aperture radius of CAMIRA clusters is independent of the richness, with aperture size of $\sim$1 h^{-1}Mpc in physical coordinates (Oguri et al., 2018a), we use one model parameter ($R_{\beta,\rm off}$) for each β-th redshift bin, which is common for all richness bins, with a flat prior from 10^{-3} to $0.5 \times (1 + \langle z_{\rm cl}\rangle_\beta) h^{-1}$Mpc. We note that Oguri et al. (2018a) investigated the offset distribution of centers detected using the CAMIRA algorithm from centers of matched X-ray clusters, and showed that in most cases the offset is less than $0.5h^{-1}$Mpc in physical transverse distances.

We also marginalize over the shape calibration and photometric redshift bias uncertainties by introducing a nuisance parameter $m_{\rm lens}$ following a Gaussian prior distribution with a mean of zero and a standard deviation of 0.01 to change the lensing model prediction as

$$\Delta\Sigma_{\alpha,\beta}(R) \to (1 + m_{\alpha,\beta})\Delta\Sigma_{\alpha,\beta}(R), \tag{2.29}$$

where $m_{\alpha,\beta} = m_{\rm lens} \times \sqrt{\sigma_{\rm shear}^2 + \sigma_{\alpha,\beta,\rm photoz}^2}/0.01$. Mandelbaum et al. (2018c) show that the systematic uncertainty in the overall calibration of the shear is $\sigma_{\rm shear} = 0.01$, and we use the photometric redshift bias uncertainty of $\sigma_{\alpha,\beta,\rm photoz}$ derived in Chapter 2.3.2. We expect a large correlation in the residual shape calibration and photometric redshift bias among different richness and redshift bins, and thus we conservatively use just one parameter $m_{\rm lens}$ for all bins.

Once the halo mass function $\mathrm{d}n(M,z)/\mathrm{d}M$ and the three-dimensional halo-matter cross-correlation $\xi_{\rm hm}(r; M, z)$ or $P_{\rm hm}(k; M, z)$ are provided for a given cosmological model (see Chapter 2.4.4), we can calculate the model prediction of the stacked lensing profile in each richness and redshift bin. The model is specified by 15 parameters in total for the entire cluster sample of $15 \le N \le 200$ and $0.1 \le z_{\rm cl} \le 1.0$: eight parameters $\{A, B, B_z, C_z, \sigma_0, q, q_z, p_z\}$ for the richness-mass relation $P(\ln N|M, z)$, six parameters $\{f_0, f_N, f_z, R_{1,\rm off}, R_{2,\rm off}, R_{3,\rm off}\}$ for the off-centering effect, and one nuisance parameter ($m_{\rm lens}$) for the uncertainty in lensing amplitudes. We use the FFTLog algorithm (Hamilton, 2000) for Fourier transforms, which allows a fast, but sufficiently accurate and precise computation of the model prediction.

2.4.4 N-body simulation based halo emulator for the mass function and the lensing profile

The model predictions must be accurate in order to estimate the model parameters in an unbiased way. For this purpose, cosmological N-body simulations are one of the methods commonly used in the literature. Here, we use the database generated by the Dark Quest campaign (Nishimichi et al., 2019) described in Appendix C to predict the halo mass function and the halo-matter cross-correlation function. The minimum halo mass of the emulator is $10^{12}h^{-1}M_{\odot}$. Throughout this chapter, we set $M_{\rm min} = 10^{12}h^{-1}M_{\odot}$ and $M_{\rm max} = 2\times10^{15}h^{-1}M_{\odot}$ for the minimum and maximum halo masses, respectively, to evaluate the halo mass integration in the model predictions of abundances and stacked lensing profiles.

For the *Planck* cosmological model, we use a simple interpolation scheme for a fixed cosmological model. Specifically, we employ exactly the same cosmological parameters as their fiducial cosmological model, for which 24 independent realizations of high-resolution runs are available. The relevant statistics are interpolated as a function of mass and redshift (see Murata et al., 2018). On the other hand, we use a halo emulator called Dark Emulator in Nishimichi et al. (2019) constructed from the Dark Quest campaign (see Appendix C for more details), to interpolate over the cosmological parameter space and compute the predictions for the *WMAP* cosmological model. This scheme relies on data compression based on Principal Component (PC) Analysis followed by Gaussian Process Regression for each PC coefficient. This is done for a subset of 80 cosmological models. Note that the realizations for the *Planck* cosmology are not used in the regression, but rather are used as part of the validation set to assess the performance of the emulator.

We estimate impacts of the uncertainties in the emulator on constraints of the mass-richness parameters as follows. For the *Planck* cosmology, we shift the halo mass function and the halo-matter cross-correlation function in each bin of halo mass, redshift, and separation length by one standard deviation uncertainty from the 24 realizations to opposite sides, and we calculate χ^2 at the best-fit mass-richness relation parameters for the fiducial analysis below. We find that $\chi^2 = 106.9$ while we have $\chi^2 = 107.0$ for the fiducial emulator as shown in Table 2.2, suggesting that the emulator precision for the *Planck* cosmology is high enough for our analysis. For the *WMAP* cosmology, we estimate the impacts using the outputs of Dark Emulator for the *Planck* cosmology by comparing it with the fiducial emulator for the *Planck* cosmology. Since the realizations for the *Planck* cosmology are not used in the regression, differences between the 24 realizations and the Dark Emulator reveal the typical impact of the uncertainties in the emulator from the Dark Emulator for the *WMAP* cosmology. The errors for the model parameters are consistent between the two emulators. On the other hand, a shift for the median value of A is ~ 0.35 compared to the error width, while shifts for the other parameters are smaller than ~ 0.15 compared to the error widths. This suggests that systematic uncertainties from the emulator for the *WMAP* cosmology increase the error for A by $\sim 6\%$ and the errors for other parameters by $\sim 1\%$. Since these impacts of the emulator precision do not change the constraints

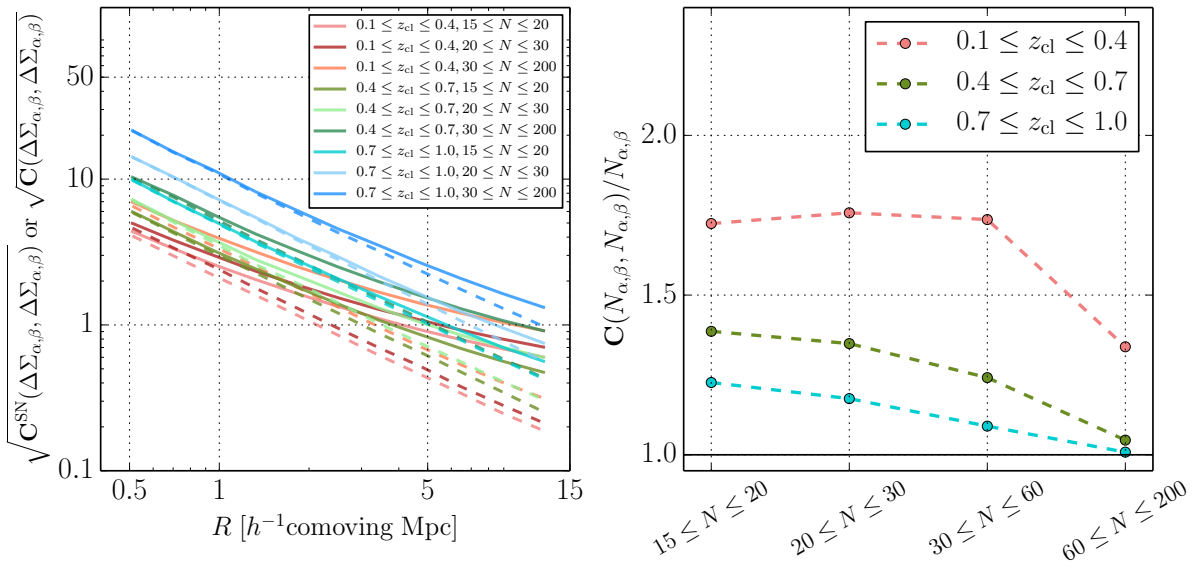

Figure 2.1 Diagonal components of the covariance matrix for the stacked lensing profiles and abundance measurements for CAMIRA clusters in the fiducial analysis with the photometric redshift catalog `MLZ`, the fiducial photometric redshift source selection *Pcut* with $\Delta z = 0.1$, and *Planck* cosmological parameters. We estimate the shape noise covariance $\mathbf{C}^{\rm SN}$ for the lensing measurements by randomly rotating the shapes in the real shape catalog, and we use analytic covariances to estimate other components of the sample covariance and Poisson noise where we use the richness-mass parameters of $\{A, B, B_z, C_z, \sigma_0, q, q_z, p_z\} = \{3.16, 0.92, -0.13, 4.17, 0.29, -0.12, -0.02, 0.52\}$, which are best-fit parameters with the simpler covariance (see Appendix D.1 for more details). Left: solid curves show the square root of the diagonal elements of the full covariance $\mathbf{C}$ for the lensing measurements in each redshift and richness bin and dashed curves show the shape noise contribution $\mathbf{C}^{\rm SN}$ for comparison. Right: the ratio of the full covariance of the abundances in each redshift and richness bin, relative to the Poisson contribution. The denominators come from the model prediction of the abundances $N_{\alpha,\beta}$ at the same richness-mass relation parameters as above: $N_{\alpha,1} = \{255.0, 191.2, 105.8, 17.0\}$, $N_{\alpha,2} = \{319.6, 198.4, 75.2, 5.0\}$, $N_{\alpha,3} = \{340.6, 185.2, 54.5, 2.0\}$.

on the mass-richness relation parameters very significantly, we ignore these uncertainties in this thesis for simplicity.

2.4.5 Covariance

We must estimate the covariance describing the statistical uncertainties of the stacked lensing profiles and the abundance. The covariance consists of shape noise covariance from the finite number of lens-source pairs, Poisson noise for the abundance from the finite number of the clusters, and sample covariance from an imperfect sampling of the fluctuations in large-scale structure within a finite survey volume (e.g., Hu & Kravtsov, 2003; Takada & Bridle, 2007; Oguri & Takada, 2011; Takada & Hu, 2013; Hikage & Oguri, 2016; Takahashi et al., 2018; Shirasaki & Takada, 2018). We estimate the shape noise covariance for the stacked lensing profiles directly from the data (e.g., Murata et al., 2018) by repeating lensing measurements (equation 2.4) for source galaxies with their orientations randomized 15,000 times. The shape noise covariance estimated in this manner accounts for the survey geometry and the inhomogeneous distribution of source galaxies. As discussed in Appendix D.1, we adopt an analytic halo model (Cooray

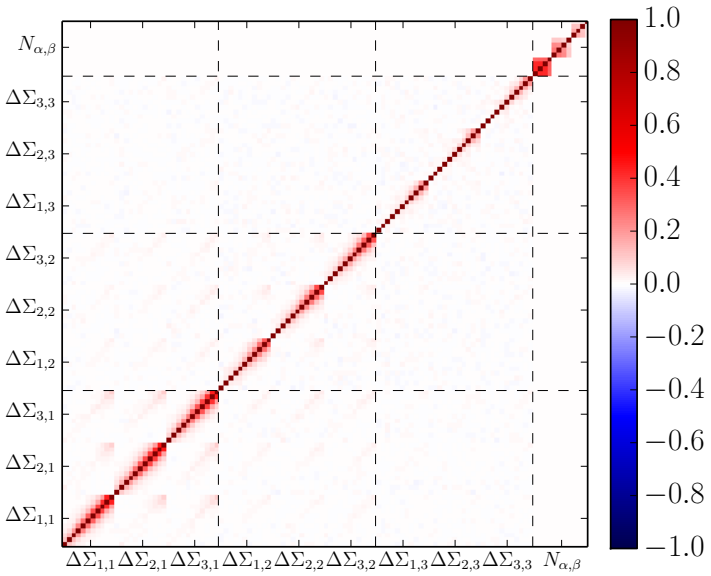

Figure 2.2 Correlation coefficient r_{ij} (equation 2.30) of the covariance matrix in Figure 2.1 for the fiducial setup. The order of data vectors for $N_{\alpha,\beta}$ is the same as in Table 2.1. In the fiducial analysis, we do not include the cross-covariance between the lensing and abundance measurements since its effect on parameter estimation is small. See Appendix D.1 for more details.

& Sheth, 2002) to compute the sample covariance and the covariance for the abundance assuming that the distribution of clusters and lensing fields obey a Gaussian distribution. We note that we compute the shape noise covariance and the sample covariance for each setup of cosmological parameters, photo-z catalog, and source selection cut as described in Appendix D.1.

In Appendix D.2, we validate the analytic covariance model for the sample covariance by comparing it with the covariance estimation from 2268 mock catalogs of the source galaxies and the CAMIRA clusters for the HSC footprint, which are generated from full-sky ray-tracing simulations with halo catalogs (Shirasaki et al., 2019) based on methods described in Shirasaki et al. (2017) (see also Shirasaki & Yoshida, 2014). The mock catalogs are based on full-sky, light-cone cosmological simulations constructed from sets of N-body simulations (Takahashi et al., 2017) with *WMAP* cosmological parameters (Hinshaw et al., 2013). The lensing effects at a given angular position are computed by a ray-tracing simulation through the foreground matter distribution from the multiple lens-plane algorithm (Hamana & Mellier, 2001; Shirasaki et al., 2015). Each source plane is given in HEALPix format (Górski et al., 2005) with an angular resolution of about 0.43 arcmin. The mock galaxy shape catalog accounts for various effects as in the real data, including survey geometry, the inhomogeneous angular distribution of source galaxies, statistical uncertainties in the photo-z estimation of each galaxy, and variations in the lensing weight from observational conditions and galaxy properties, since the mock catalog is constructed based on the *real* shape catalog (see Shirasaki et al., 2019,

for more details). We also construct mock catalogs of the CAMIRA clusters by using the catalog of halos in each light-cone simulation realization in Takahashi et al. (2017), which are identified with ROCKSTAR (Behroozi et al., 2013). We refer the readers to Appendix D.2 for more details.

Figure 2.1 shows the diagonal components of the covariance matrix for the fiducial analysis with *Planck* cosmological parameters, the fiducial photo-z catalog, and the fiducial source selection cut. The left panel compares the full covariance with the shape noise covariance for the stacked lensing profiles. The sample covariance starts to become the dominant contribution even from $R = 2h^{-1}$Mpc for the lowest redshift bin ($0.1 \leq z_{\rm cl} \leq 0.4$) due to the high source density of the HSC shear catalog (see also Miyatake et al., 2019). The right panel shows diagonal components of the covariance for the abundance compared to the Poisson term. The sample variance contributions in the abundance for the lower redshift bins are higher than those for the higher redshift bins.

Figure 2.2 shows the correlation coefficient matrix defined as

$$r_{ij} \equiv \frac{\mathbf{C}(D_i, D_j)}{\sqrt{\mathbf{C}(D_i, D_i)\mathbf{C}(D_j, D_j)}}, \tag{2.30}$$

where D_i is the i-th component of the data vector $\mathbf{D}$. There are large correlations among neighboring bins especially for large radii and lower redshift, since the same large-scale structure causes spatially-correlated fluctuations in the stacked lensing profile and the abundance measurements especially among neighboring radii or different richness bins for each redshift bin (Takada & Bridle, 2007; Oguri & Takada, 2011).

We then calculate the signal-to-noise ratio with the measurements and the covariance for the fiducial analysis with the *Planck* cosmological parameters. The total signal-to-noise ratio from the stacked lensing profiles and abundance measurements is 61.0, and the signal-to-noise ratios for the stacked lensing profiles and the abundance are 53.0 and 30.3, respectively. The lensing signal-to-noise ratios in each redshift bin are 36.6, 34.2, and 19.3 from the lowest to highest redshift bins.

2.5 Results

In this chapter, we show the posterior distribution of the parameters, the joint probability $P_\beta(\ln M, \ln N)$ in each redshift bin, the mass-richness relation $P_\beta(\ln M|N)$ in each redshift bin, and the richness-mass relation $P(\ln N|M, z)$, from the joint analysis of the model parameters based on the abundance and lensing profiles under the fiducial setups. In this work, we fix the cosmological parameters to the *Planck* cosmology (Planck Collaboration et al., 2016) or the *WMAP* cosmology (Hinshaw et al., 2013) as described in Chapter 1.6 to investigate how and to what degree the difference of the cosmological parameters affects the constraints on the mass-richness relation without informative priors on the parameters, and to gain insight into cluster cosmology by comparing the results.

2.5.1 Posterior distribution of parameters

We constrain the model parameters by comparing the model predictions with the measurements of the abundance and the lensing profiles. We perform Bayesian parameter estimation assuming a Gaussian form for the likelihood, $\mathcal{L} \propto |\mathbf{C}|^{-1/2} \exp(-\chi^2/2)$, with

$$\chi^2 = \sum_{i,j} \left[\mathbf{D} - \mathbf{D}^{\rm model}\right]_i \left(\mathbf{C}^{-1}\right)_{ij} \left[\mathbf{D} - \mathbf{D}^{\rm model}\right]_j, \tag{2.31}$$

where $\mathbf{D}$ is a data vector that consists of the lensing profiles and the abundance in different radial, richness, and redshift bins, $\mathbf{D}^{\rm model}$ is the model prediction, and $\mathbf{C}^{-1}$ is the inverse of the covariance matrix (see Chapter 2.4.5). We use 11 radial bins $\mathbf{R}$ in each richness and redshift bin for the stacked lensing profile. The indices i and j run from 1 to the total number of data points (111 for the fiducial analysis). We perform the parameter estimation with the affine-invariant Markov Chain Monte Carlo (hereafter MCMC) sampler of Goodman & Weare (2010) as implemented in the python package EMCEE (Foreman-Mackey et al., 2013).

In Table 2.2, we summarize the results of the parameter estimation, including a description of each parameter, priors, the median and 68% credible level interval after removing the burn-in chains and marginalizing over the other parameters, and $\chi^2_{\rm min}$/dof to show goodness-of-fit under *Planck* or *WMAP* cosmology. In fitting we employ uninformative flat priors for all of the richness-mass relation parameters and the off-centering parameters. We also show the 68% and 95% credible level contours in each two-parameter subspace, and one-dimensional posterior distributions in Appendix F. Each richness-mass relation parameter is well constrained by the joint analysis compared to its prior. From Table 2.2 and Appendix F, we find that constraints on A, σ_0 and q are systematically different between *Planck* and *WMAP* cosmologies mainly due to the differences in their halo mass functions. On the other hand, constraints on the other parameters are similar to each other. The result for the *WMAP* cosmology prefers a higher mean normalization A and lower scatter normalization σ_0 than for the *Planck* cosmology. In addition, the result for *Planck* cosmology prefers negative q values (i.e., larger scatter at the lower halo mass) more significantly than the *WMAP* cosmology, although it is still a $< 2\sigma$ preference. For both cosmological models, off-centering parameters are constrained well compared to their priors. The centering fraction at the pivot richness and redshift is constrained as $f_0 = 0.68^{+0.05}_{-0.06}$, which is consistent with $f_{\rm cen} = 0.68 \pm 0.09$ in the analysis of Oguri et al. (2018a), who estimated the centering fraction without redshift or richness dependences by comparing CAMIRA cluster centers with X-ray centroids. The richness dependence of the off-centering fraction f_N prefers positive values with a high significance, indicating that the higher richness clusters are centered better than the lower richness clusters. This might be partly because CAMIRA obtained lower richness values for off-centered clusters given that the richness is computed around the identified BCG using a circular aperture. On the other hand, the redshift dependence parameter f_z is consistent with zero. The off-centering radius parameter for each redshift bin $R_{\beta,{\rm off}}$ is constrained compared to its prior, but only marginally.

We check the validity of our model by monitoring the χ^2 of the best-fitting models. Since the posterior distribution of the nuisance parameter $m_{\rm lens}$ for lensing amplitudes is strongly determined by its prior, we do not include it as a parameter when calculating the number of degrees-of-freedom, thus dof $= 111 - 14 = 97$ where 111 is the total number of data points for the fitting and 14 is the total number of richness-mass relation parameters and off-centering parameters. We find that $\chi^2_{\rm min}/{\rm dof} = 107.0/97$ (p-value $= 0.23$) for the *Planck* cosmology, and $\chi^2_{\rm min}/{\rm dof} = 106.6/97$ (p-value $= 0.24$) for the *WMAP* cosmology, both of which are acceptable p-values. This indicates that we cannot distinguish between *Planck* and *WMAP* cosmologies from the abundance and lensing measurements, partly because of our adoption of a flexible richness-mass relation.

We also show the comparison of the model predictions from the MCMC chains with the measurements of the lensing profiles and abundance in Figures 2.3 and 2.4 for *Planck* and *WMAP* cosmologies, respectively. The figures show that the model predictions reproduce the lensing profiles and abundance simultaneously for both sets of cosmological parameters with the fiducial richness-mass relation model.

Table 2.2 The model parameters, priors, and parameter estimations from our joint analysis of lensing and abundance measurements.*

Parameter	Description	Prior	Median and Error *Planck*	Median and Error *WMAP*
A	$\langle \ln N \rangle$ at pivot mass scale and pivot redshift	flat$[2, 5]$	$3.15^{+0.07}_{-0.08}$	$3.36^{+0.05}_{-0.06}$
B	Coefficient of halo mass dependence in $\langle \ln N \rangle$	flat$[0, 2]$	$0.86^{+0.05}_{-0.05}$	$0.83^{+0.03}_{-0.03}$
B_z	Coefficient of linear redshift dependence in $\langle \ln N \rangle$	flat$[-50, 50]$	$-0.21^{+0.35}_{-0.42}$	$-0.20^{+0.26}_{-0.34}$
C_z	Coefficient of square redshift dependence in $\langle \ln N \rangle$	flat$[-50, 50]$	$3.61^{+1.96}_{-2.23}$	$3.51^{+1.32}_{-1.59}$
σ_0	$\sigma_{\ln N\|M,z}$ at pivot mass scale and pivot redshift	flat$[0, 1.5]$	$0.32^{+0.06}_{-0.06}$	$0.19^{+0.07}_{-0.07}$
q	Coefficient of halo mass dependence in $\sigma_{\ln N\|M,z}$	flat$[-1.5, 1.5]$	$-0.08^{+0.05}_{-0.04}$	$-0.02^{+0.03}_{-0.03}$
q_z	Coefficient of linear redshift dependence in $\sigma_{\ln N\|M,z}$	flat$[-50, 50]$	$0.03^{+0.31}_{-0.30}$	$0.23^{+0.37}_{-0.35}$
p_z	Coefficient of square redshift dependence in $\sigma_{\ln N\|M,z}$	flat$[-50, 50]$	$0.70^{+1.71}_{-1.60}$	$1.26^{+1.77}_{-1.49}$
f_0	Centering fraction at pivot richness and redshift	$0 < f_{\rm cen}^{\alpha,\beta} < 1$	$0.68^{+0.05}_{-0.06}$	$0.68^{+0.05}_{-0.06}$
f_N	Coefficient of richness dependence in $f_{\rm cen}^{\alpha,\beta}$	$0 < f_{\rm cen}^{\alpha,\beta} < 1$	$0.33^{+0.10}_{-0.09}$	$0.33^{+0.10}_{-0.09}$
f_z	Coefficient of redshift dependence in $f_{\rm cen}^{\alpha,\beta}$	$0 < f_{\rm cen}^{\alpha,\beta} < 1$	$-0.14^{+0.35}_{-0.34}$	$-0.19^{+0.34}_{-0.34}$
$R_{1,\rm off}$	Off-centering radius for the first redshift bin	flat$[10^{-3}, 0.64]$	$0.39^{+0.10}_{-0.09}$	$0.38^{+0.10}_{-0.09}$
$R_{2,\rm off}$	Off-centering radius for the second redshift bin	flat$[10^{-3}, 0.78]$	$0.55^{+0.12}_{-0.11}$	$0.52^{+0.12}_{-0.10}$
$R_{3,\rm off}$	Off-centering radius for the third redshift bin	flat$[10^{-3}, 0.92]$	$0.59^{+0.17}_{-0.17}$	$0.58^{+0.17}_{-0.15}$
$m_{\rm lens}$	Marginalization parameter of the lensing amplitudes	Gauss$(0, 0.01)$	$0.00^{+0.01}_{-0.01}$	$0.00^{+0.01}_{-0.01}$
$\chi^2_{\rm min}$/dof			107.0/97	106.6/97

* In the fiducial analysis, we vary 15 parameters while fixing the cosmological parameters to either *Planck* or *WMAP*. We use flat priors for all richness-mass parameters and off-centering parameters, denoted as flat$[x, y]$, with the region between x and y. We use a Gaussian prior for marginalizing over parameters of the lensing amplitudes, with mean value 0 and standard deviation 0.01 (see around equation 2.29 for more details on the implementation). We additionally restrict the scatter parameter space to $\sigma_{\ln N|M,z} > 0$ for the range of halo masses and redshifts we consider, $10^{12} \leq M/[h^{-1}M_\odot] \leq 2 \times 10^{15}$ and $0.1 \leq z \leq 1.0$. We also restrict the off-centering fraction parameters space to $0 < f_{\rm cen}^{\alpha,\beta} < 1$ for all richness and redshift bins. The maximum ranges of priors for the off-centering radii correspond to $R < 0.5h^{-1}$Mpc in physical coordinates using the mean redshift value in each redshift bin from Table 2.1. The column labeled as "Median and Error" denotes the median and the 16th and 84th percentiles of the posterior distribution. We also show the minimum chi-square ($\chi^2_{\rm min}$) with the number of degrees of freedom (dof) at the bottom row. Since the lensing marginalization parameter is determined strongly by the prior above, we do not include it as a free parameter when calculating dof (i.e., dof$= 97 = 111 - 14$, where 111 is the total number of data points and 14 is the total number of richness-mass relation parameters and off-centering parameters). The correlations among the parameters are shown in Appendix F. We adapt $M_{\rm pivot} = 3 \times 10^{14}h^{-1}M_\odot$, $z_{\rm pivot} = 0.6$, and $N_{\rm pivot} = 25$ for the pivot values.

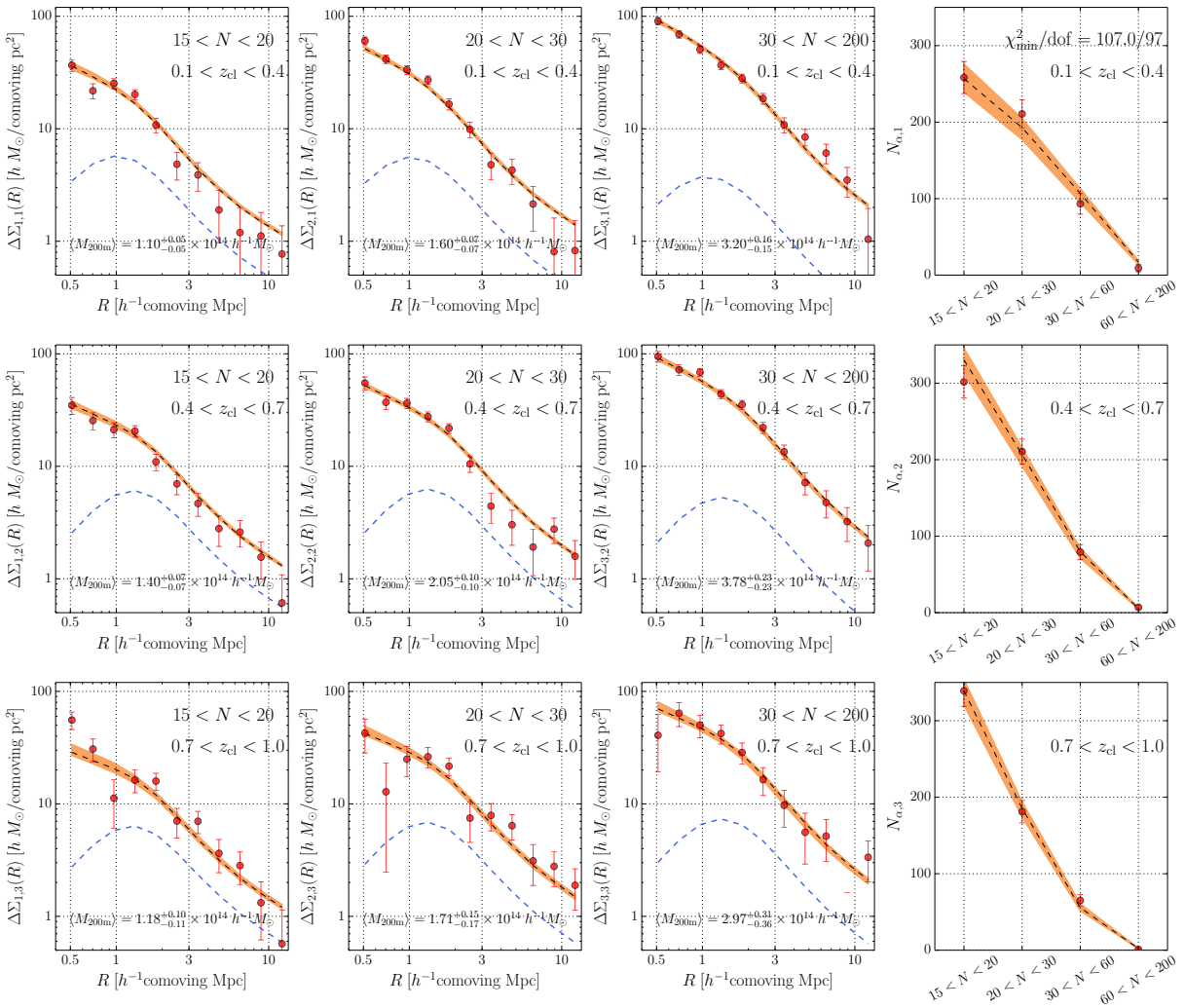

Figure 2.3 The measurements and fitting results of the stacked lensing and abundance with the *Planck* cosmological parameters. Points with error bars show the measurements, and the shaded regions show the 16th and 84th percentiles of the model predictions from the MCMC chains. The error bars denote the diagonal components of the covariance matrix (see also Figure 2.1). The black dashed curves show the model predictions at the best-fit parameters. The light-blue dashed curves show contributions from off-centered clusters to lensing profiles at the best-fit model parameters. We show the minimum value of the reduced chi-square in the upper-right corner. We also give 16th, 50th (median), and 84th percentiles of the mean mass $\langle M_{200\mathrm{m}}\rangle$ in each lensing panel from the MCMC chains.

2.5.2 Joint probability $P_\beta(\ln M, \ln N)$ and mass-richness relation $P_\beta(\ln M|N)$

We then calculate the joint probability distribution of halo mass and richness in each redshift bin after averaging over the redshift range with volume weight $\mathrm{d}^2V/\mathrm{d}z\mathrm{d}\Omega = \chi^2(z)/H(z)$ as

$$\begin{aligned} P_\beta(\ln M, \ln N) &\propto \int_{z_{\beta,\min}}^{z_{\beta,\max}} \mathrm{d}z\ \frac{\chi^2(z)}{H(z)} P(\ln N|M,z) P(\ln M|z) \\ &\propto \int_{z_{\beta,\min}}^{z_{\beta,\max}} \mathrm{d}z\ \frac{\chi^2(z)}{H(z)} P(\ln N|M,z) \frac{\mathrm{d}n(M,z)}{\mathrm{d}\ln M} \end{aligned} \tag{2.32}$$

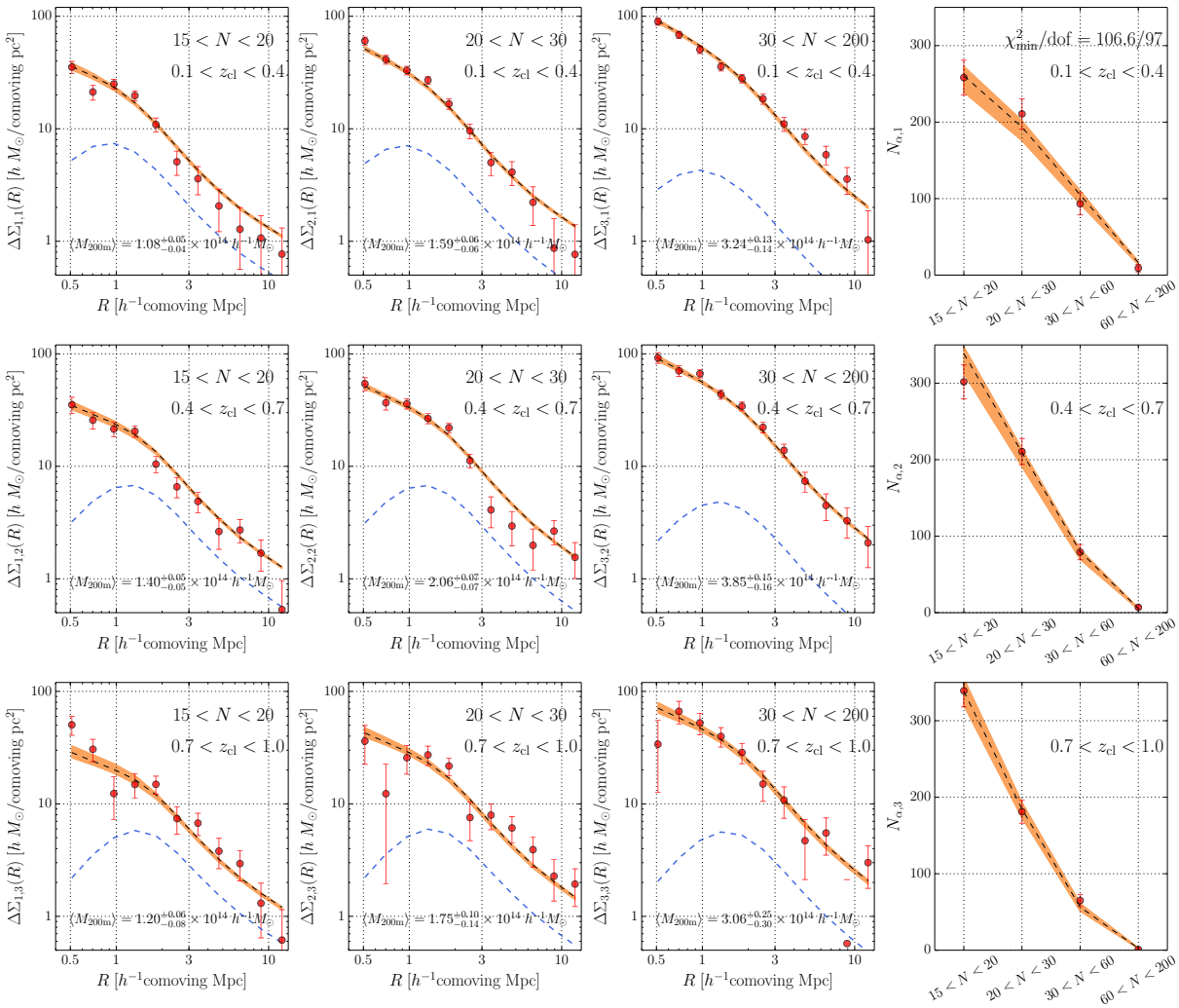

Figure 2.4 Same as Figure 2.3, but for the *WMAP* cosmological parameters.

where $P(\ln M|z)$ is the probability distribution of the halo mass for a given redshift, and thus is proportional to the halo mass function $\mathrm{d}n(M,z)/\mathrm{d}\ln M$. The normalization factor is determined in the range of $10^{12} \leq M/[h^{-1}M_\odot] \leq 2\times10^{15}$ and $15 \leq N \leq 200$, and we restrict the domain of the joint probability to this range. We use the best-fit model parameters of the fiducial analysis in Table 2.2 for $P(\ln N|M,z)$. The contours in Figure 2.5 show the joint probability distribution (equation 2.32) in each redshift bin for the *Planck* or *WMAP* cosmological parameters. We obtain the distribution of $\ln N$ and $\ln M$ in the range of richness ($N_{\rm min} = 15$, $N_{\rm max} = 200$) for each redshift bin by integrating the joint probability distribution along the halo mass and the richness directions respectively as

$$P_\beta(\ln N|M_{\rm min} \leq M \leq M_{\rm max}) = \int_{\ln M_{\rm min}}^{\ln M_{\rm max}} \mathrm{d}\ln M \; P_\beta(\ln M, \ln N) \tag{2.33}$$

and

$$P_\beta(\ln M|N_{\rm min} \leq N \leq N_{\rm max}) = \int_{\ln N_{\rm min}}^{\ln N_{\rm max}} \mathrm{d}\ln N \; P_\beta(\ln M, \ln N). \tag{2.34}$$

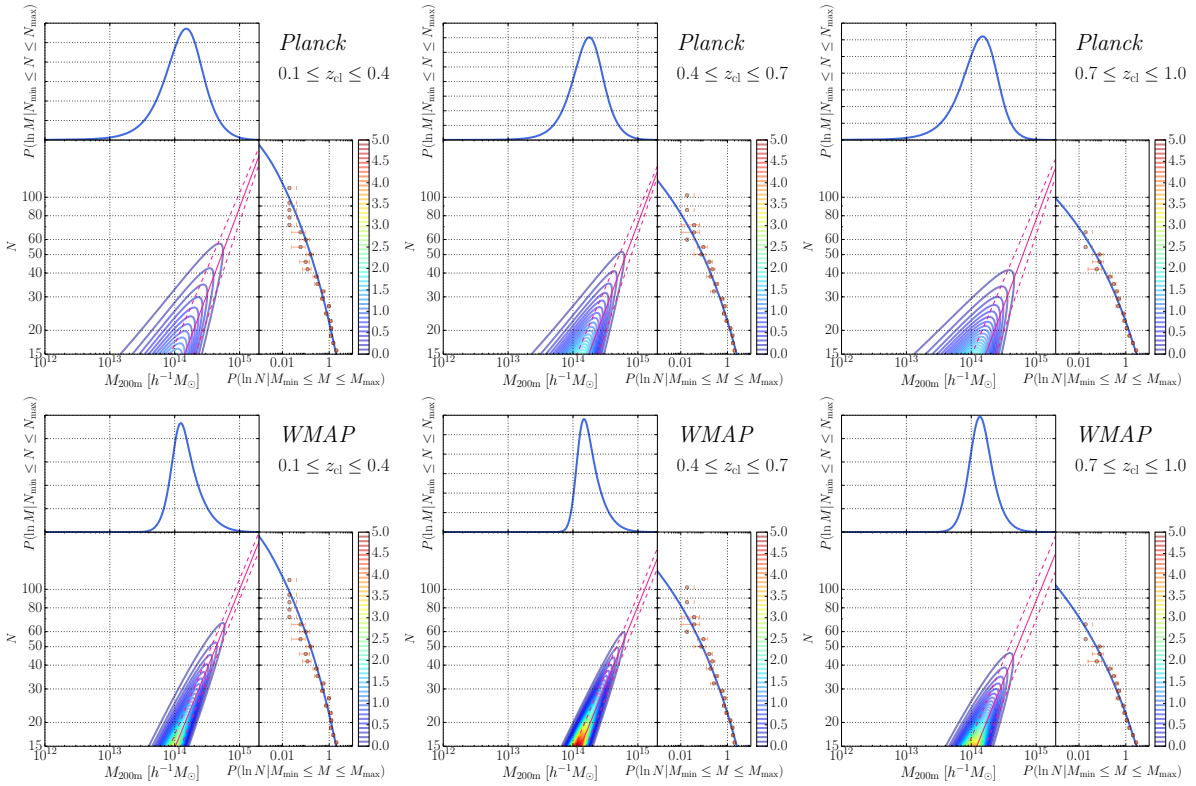

Figure 2.5 Joint probability distribution $P_\beta(\ln M, \ln N)$ defined in equation (2.32) from the best-fit parameters in the fiducial analysis in Figures 2.3 and 2.4. The upper panels show the result for the *Planck* cosmological parameters for each redshift bin, whereas the lower panels show the result for the *WMAP* cosmological parameters. The solid line shows the best-fit model of $\langle \ln N \rangle (M, z)$ and the dashed lines show the 16th and 84th percentiles of the richness distribution at a fixed mass (i.e., the width of $\sigma_{\ln N|M,z}$). Here, for simplicity, we use $z = 0.3, 0.6, 0.9$ as representative values for the redshift bins. The solid line in the right panel of each plot shows the probability distribution of the richness defined in equation (2.33), and points with error-bars denote measurements with Poisson errors in finer richness binning. The top panel of each plot shows the probability distribution of the halo mass defined in equation (2.34).

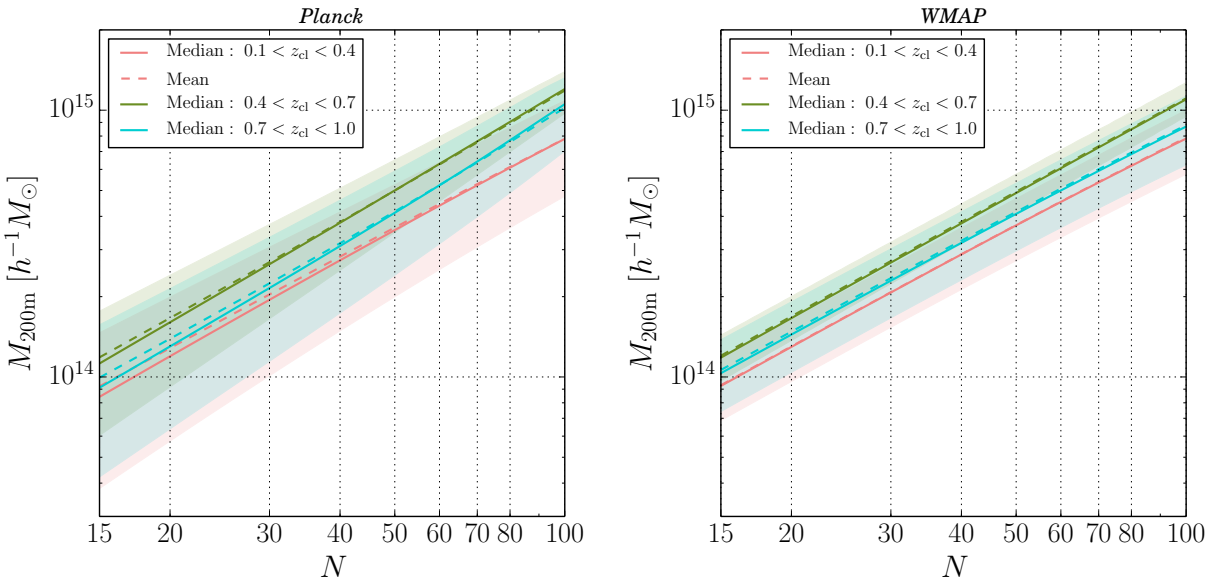

Figure 2.6 Conditional probability distribution $P_\beta(\ln M|N)$ defined in equation (2.36) from the best-fit richness-mass relation parameters from the fiducial analysis, for all three redshift bins. Left and right panels show results for *Planck* and *WMAP* cosmological parameters, respectively. The solid line denotes the median of the mass distribution at a fixed richness for each redshift bin, and the dashed lines denote the mean mass at a fixed richness $\langle M|N\rangle$ (see equation 2.37). The shaded regions show the range of the 16th and 84th percentiles of the mass distribution at a fixed richness.

The richness distributions $P_\beta(\ln N|M_{\rm min} \leq M \leq M_{\rm max})$ shown in Figure 2.5 indicate that the model reproduces the observed richness function at much finer bins than those used for the analysis. The joint probability contours in Figure 2.5 show that scatter widths of the mass at a given fixed richness for the *WMAP* cosmology are smaller than those for the *Planck* cosmology for all redshift bins, and that the widths for the middle redshift bin ($0.4 \leq z_{\rm cl} \leq 0.7$) are the smallest among the redshift bins for both cosmologies. We discuss the origin of these results in Chapter 2.6.3.

Since we constrain the richness-mass relation $P(\ln N|M,z)$ from a joint analysis, we can compute the mass-richness relation $P(\ln M|N,z)$ using Bayes theorem as

$$\begin{aligned} P(\ln M|N,z) &= \frac{P(\ln N|M,z)P(\ln M|z)}{\int_{\ln M_{\rm min}}^{\ln M_{\rm max}} {\rm d}\ln M\ P(\ln N|M,z)P(\ln M|z)} \\ &= \frac{P(\ln N|M,z)\dfrac{{\rm d}n(M,z)}{{\rm d}\ln M}}{\int_{\ln M_{\rm min}}^{\ln M_{\rm max}} {\rm d}\ln M\ P(\ln N|M,z)\dfrac{{\rm d}n(M,z)}{{\rm d}\ln M}} \end{aligned} \tag{2.35}$$

where we use the halo mass function for $P(\ln M|z)$. We then average the mass-richness relation over the

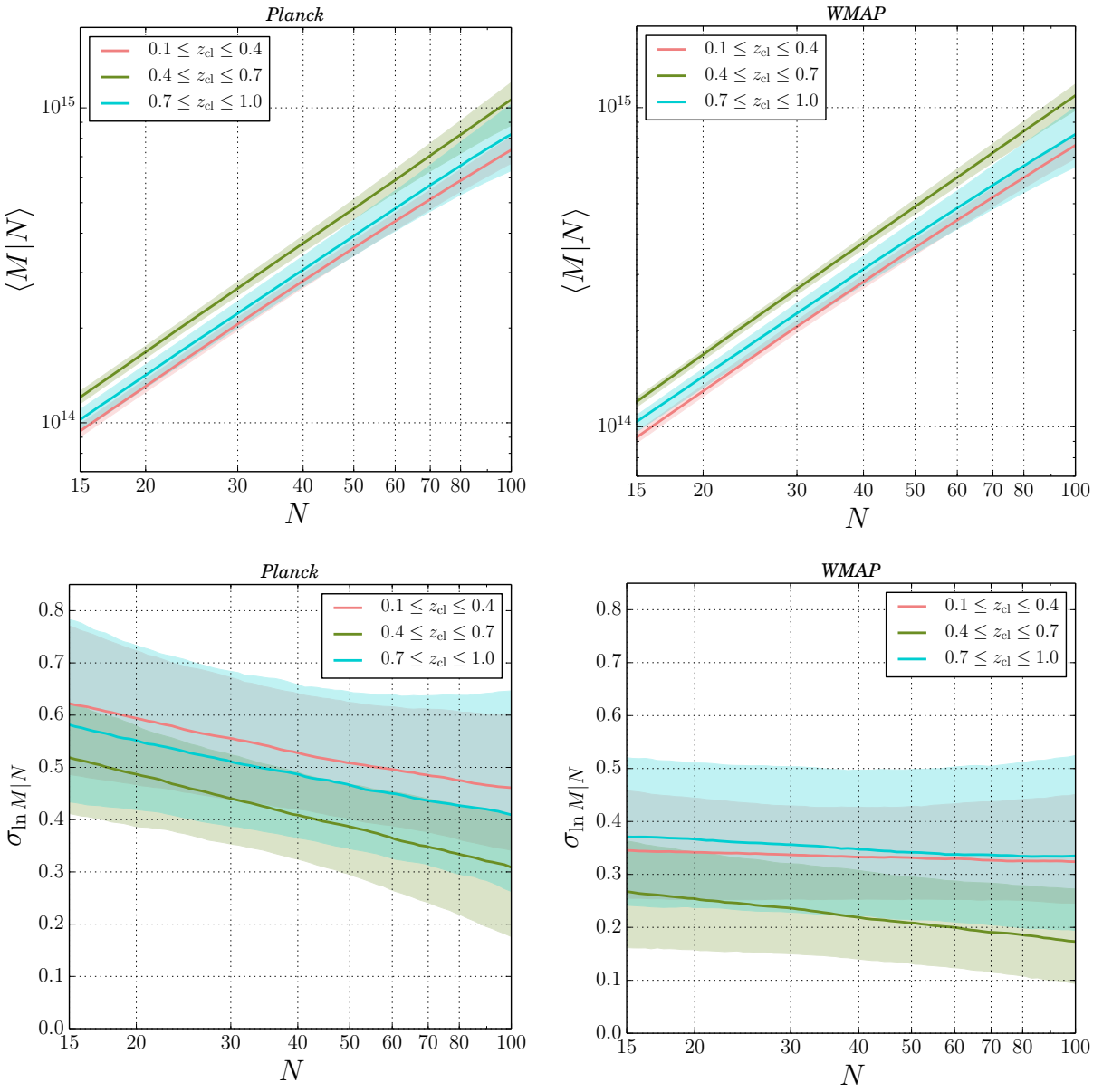

Figure 2.7 The median and the 16th and 84th percentiles of the mean and scatter values of $\langle M|N \rangle$ and $\sigma_{\ln M|N}$ from the MCMC chains for the fiducial analysis, for all three redshift bins. Note that this figure differs from Figure 2.6, which shows $\langle M|N \rangle$ and $\sigma_{\ln M|N}$ at the best-fit parameters only. The left panels show the results for the *Planck* cosmological parameters and the right panels for the *WMAP* cosmological parameters. We note that $\sigma_{\ln M|N}$ is defined by the half width of the 68% percentile region of the mass distribution at a fixed richness (see text for more details).

redshift range with volume weight for each redshift bin as

$$P_\beta(\ln M|N) = \frac{\int_{z_{\beta,\min}}^{z_{\beta,\max}} \mathrm{d}z \ \frac{\chi^2(z)}{H(z)} P(\ln M|N,z)}{\int_{z_{\beta,\min}}^{z_{\beta,\max}} \mathrm{d}z \ \frac{\chi^2(z)}{H(z)}}. \tag{2.36}$$

We obtain the mean mass for a given richness in each redshift bin as

$$\langle M|N\rangle_\beta = \int_{\ln M_{\min}}^{\ln M_{\max}} \mathrm{d}\ln M \ P_\beta(\ln M|N) M. \tag{2.37}$$

Figure 2.6 shows the median, mean, and 16% and 84% percentile region of the mass distribution at fixed richness values in each redshift bin for *Planck* and *WMAP* cosmologies, using the best-fit richness-mass relation parameters of the fiducial analysis. In Appendix E, as a sanity check, we have confirmed that our constraints are reasonably consistent with the Sunyaev–Zel'dovich (SZ) masses of eight massive clusters in Miyatake et al. (2019).

We also show the constraint on the mean relation computed in equation (2.37) and the scatter relation $\sigma_{\ln M|N}$ in Figure 2.7 from the MCMC chains after marginalizing over the model parameters (i.e., not only at the best-fit parameters as shown in Figure 2.6). Since the model generally predicts a skewed distribution of halo mass for a fixed richness value in $\ln M$ space, we define $\sigma_{\ln M|N}$ as the half width of the 68% percentile region of $P_\beta(\ln M|N)$ for each redshift bin as $\sigma_{\ln M|N} = (\ln M_{84} - \ln M_{16})/2$, where M_{84} and M_{16} are masses corresponding to the 84th and 16th percentiles of $P_\beta(\ln M|N)$ at a fixed richness, respectively. The mean relations for *Planck* and *WMAP* cosmologies are consistent with each other given the error bars for all the redshift bins, and the mean relation of $0.4 \leq z_{\rm cl} \leq 0.7$ has a larger amplitude than in the other redshift bins for both cosmologies with relatively high significance given the error bars. We constrain the mean relations at $N = 25$ with $\sim 4\%$ precision for $0.1 \leq z_{\rm cl} \leq 0.4$ and $0.4 \leq z_{\rm cl} \leq 0.7$, and $\sim 8\%$ precision for $0.7 \leq z_{\rm cl} \leq 1.0$. The scatter relation for the *Planck* cosmology increases toward lower richness values for all redshift bins, whereas the scatter for the *WMAP* cosmology is consistent with a constant value as a function of richness for all redshift bins. The scatter values for the *Planck* cosmology are systematically larger than those for the *WMAP* cosmology. This result is qualitatively consistent with the one obtained from cosmological analysis of SDSS redMaPPer clusters in Costanzi et al. (2018), which shows larger scatter values for larger $S_8 = \sigma_8(\Omega_{\rm m}/0.3)^{0.5}$ values ($S_8 = 0.85$ for the *Planck* and $S_8 = 0.79$ for the *WMAP* cosmology in this work), although the scatter modeling method is different from ours. The scatter values in the middle redshift bin ($0.4 \leq z_{\rm cl} \leq 0.7$) are also lower than those in the other redshift bins. We discuss the origin of this result in Chapter 2.6.3.

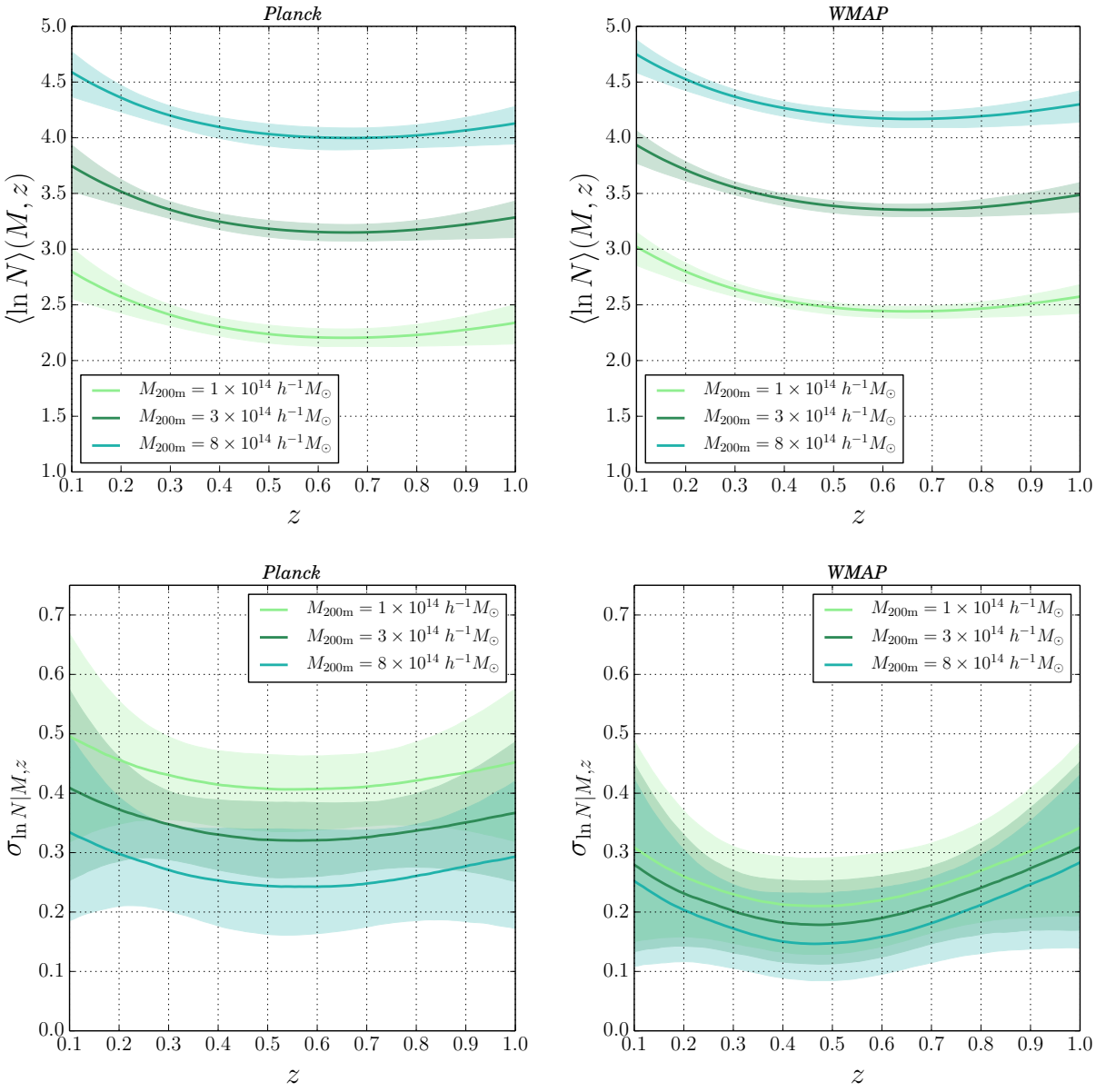

Figure 2.8 The mean and scatter relations of the richness distribution given halo masses as a function of redshift. The left panels show the results for the *Planck* cosmological parameters and the right panels for the *WMAP* cosmological parameters. We show the results for $M/(10^{14}h^{-1}M_\odot) = 1, 3, 8$ as representative halo masses. The solid lines show the median values at fixed redshift and the shaded regions show the 16th and 84th percentiles from the MCMC chains.

2.5.3 Richness-mass relation $P(\ln N|M,z)$

As complementary results to Figure 2.7 on $P_\beta(\ln M|N)$, we show the mean and scatter relations in equations (2.16) and (2.17) of the richness-mass relation $P(\ln N|M,z)$ in Figure 2.8 for typical masses as a function of redshift. We find that, for both *Planck* and *WMAP* cosmologies, the mean relation has a minimum around $z \sim 0.5$ for all typical masses. This is also true for the scatter relation especially for *WMAP* cosmology. We also discuss the origin of these constraints in Chapter 2.6.3.

2.6 Discussion

We discuss the robustness of the fiducial results in Chapter 2.6.1, and the complementarity of lensing profile and abundance measurements to constrain the richness-mass relation parameters in Chapter 2.6.2. In Chapter 2.6.3, we discuss redshift evolution in the richness-mass relation and the difference between the middle redshift bin versus the lower and higher redshift bins shown in Chapters 2.5.2 and 2.5.3.

2.6.1 Robustness of our results

Shape and photometric redshift measurement uncertainties

In the fiducial analysis, we marginalize over the shape and photometric redshift uncertainties on the lensing measurements by including the nuisance parameter $m_{\rm lens}$ in equation (2.29). To check how these uncertainties affect the model parameter constraints, we repeat the MCMC analysis ignoring these errors (i.e., setting $m_{\rm lens} = 0$) for the *Planck* cosmology with the same measurements and covariance as in the fiducial analysis. We find no significant shift in the best-fit parameters with $\chi^2_{\rm min} = 106.9$ compared to $\chi^2_{\rm min} = 107.0$ for the fiducial analysis with $m_{\rm lens}$. We also find the 68% percentile error widths do not change significantly from the fiducial analysis. Specifically, the difference between the error widths in this modified versus the fiducial analysis is smaller than 5% of the error widths in the fiducial analysis for all parameters. This result shows that the impact of these shape and photometric redshift measurement errors on the joint analysis of current lensing and abundance measurements is negligible when constraining the richness-mass relation.

Different photometric redshift catalogs or different photometric redshift cuts

We use the photometric catalog `MLZ` and the photometric redshift cuts of *Pcut* with $\Delta z = 0.1$ for the fiducial analysis in Chapter **??**. We check the robustness of our results by using different photometric redshift catalogs (see Chapter 2.2.4) or different photometric redshift cuts (see Chapter 2.3.2) for the lensing measurements. Here we assume the *Planck* cosmological parameters for this test, using the same model parameters and priors as shown in Table 2.2. We repeat the same procedure for the lensing measurements and lensing covariance calculation for different photometric redshift catalogs or cuts to constrain the model parameters by jointly fitting to the lensing and abundance measurements.

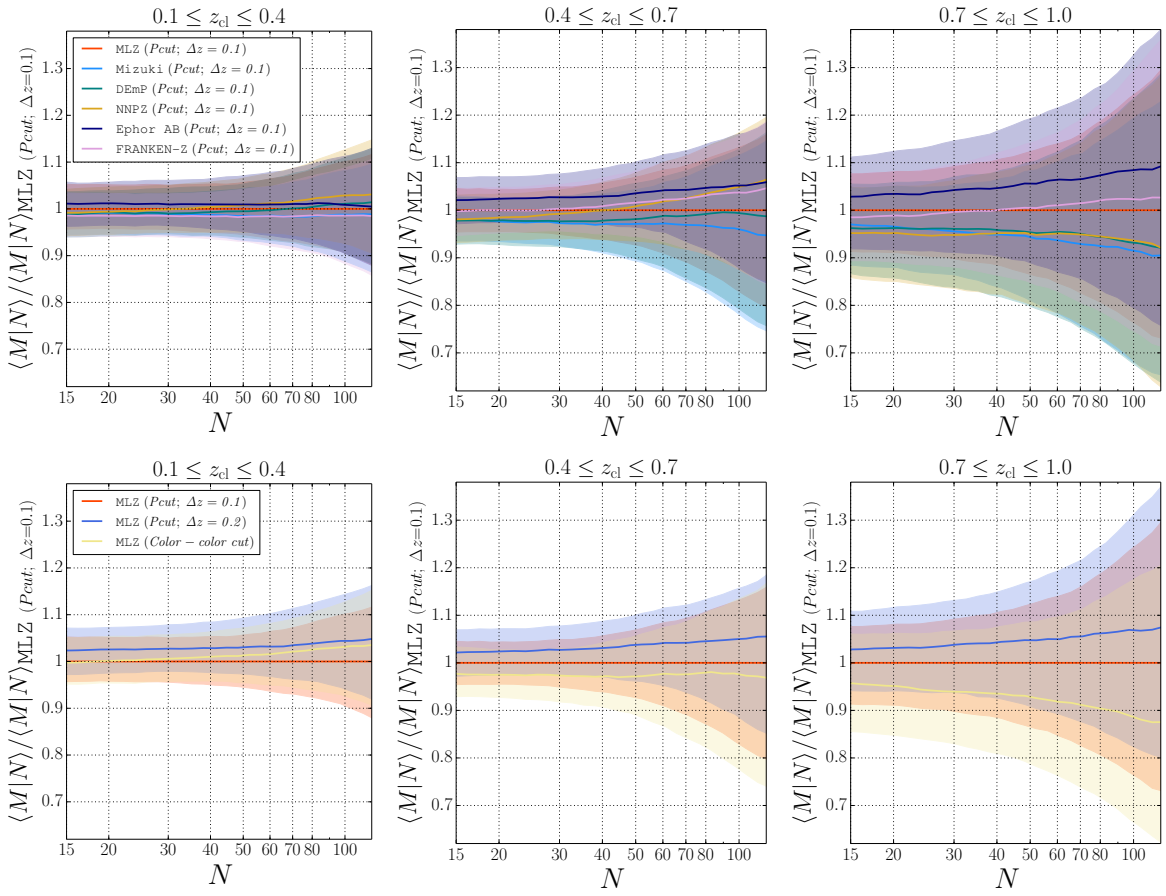

Figure 2.9 Comparison of the mean mass relation $\langle M|N\rangle$ defined in equation (2.37) for each redshift bin among the different photometric redshift catalogs (upper panels) or the different source selection cuts (lower panels) with the *Planck* cosmological parameters. We show the median and the 16th and 84th percentiles from the MCMC chains, with respect to the median values of $\langle M|N\rangle$ for the fiducial catalog `MLZ` and the fiducial cut *Pcut* with $\Delta z = 0.1$.

In Figure 2.9, we show the median and the 16th and 84th percentiles of the mean relation $\langle M|N\rangle$ for each redshift bin with respect to the median from the fiducial result of `MLZ` and the *Pcut* method with $\Delta z = 0.1$. The top panels in Figure 2.9 show the results with different photometric redshift catalogs, but with the same photometric redshift cuts of the *Pcut* method with $\Delta z = 0.1$. We show that the mean relation $\langle M|N\rangle$ is consistent between the difference photometric redshift catalogs for all redshift bins. The lower panels in Figure 2.9 show the results with different photometric redshift cuts, but with the same photometric redshift catalog `MLZ`, showing that the results are consistent with each other given the error bars for all of the redshift bins. This is partly due to our conservative choice of the radial range from $0.5h^{-1}$Mpc in comoving coordinates for the lensing measurements to avoid possible dilution effects on the lensing measurement based on Medezinski et al. (2018b). These results show the robustness of our result to photo-z differences.

2.6.2 Complementarity of abundance and stacked lensing profile measurements

We constrained the model parameters by jointly fitting to the lensing profiles and abundance measurements in Chapter 2.5. Here we study how lensing profile or abundance measurements alone constrain the model parameters, which helps explain how the joint analysis lifts the model parameter degeneracies. We note that we use the same measurements and covariance matrix as in the fiducial analysis.

Figure 2.10 shows the 68% and 95% credible level contours in each two-parameter subspace of the richness-mass relation parameters. The figure shows that the two observables are complementary to each other, which is why their combination can efficiently lift model parameter degeneracies. The lensing measurements constrain the mean normalization parameter A better than the abundance measurements, mainly because the lensing measurements are more sensitive to the mass scale in each redshift and richness bin. The lensing measurements also constrain the scatter normalization parameter σ_0 better than the abundance. On the other hand, other parameters such as the mass dependence parameter B and the redshift evolution parameters B_z, C_z in the mean relation are relatively better constrained by the abundance measurements. In summary, the two observables combine effectively to break complex degeneracies in the model parameters.

2.6.3 Redshift evolution in the richness-mass relation

In this chapter, we use the richness-mass relation model with linear and square redshift evolution parameters (B_z, C_z, q_z, and p_z) in the fiducial analysis. When we use the richness-mass relation model without any redshift evolution parameters (i.e., without B_z, C_z, q_z, and p_z) we obtain $\chi^2_{\rm min}/{\rm dof} = 151.3/101$ (p-value $= 8\times10^{-4}$), and when we adopt the model without square redshift evolution parameters (i.e., without C_z and p_z) we obtain $\chi^2_{\rm min}/{\rm dof} = 138.6/99$ (p-value $= 5\times10^{-3}$), both of which are unacceptable p-values. Here we use the *Planck* cosmological parameters with the same covariance as the fiducial analysis for these analyses. Given the acceptable p-value of $\chi^2_{\rm min}/{\rm dof} = 107.0/97$ in Table 2.2, we use the richness-mass model

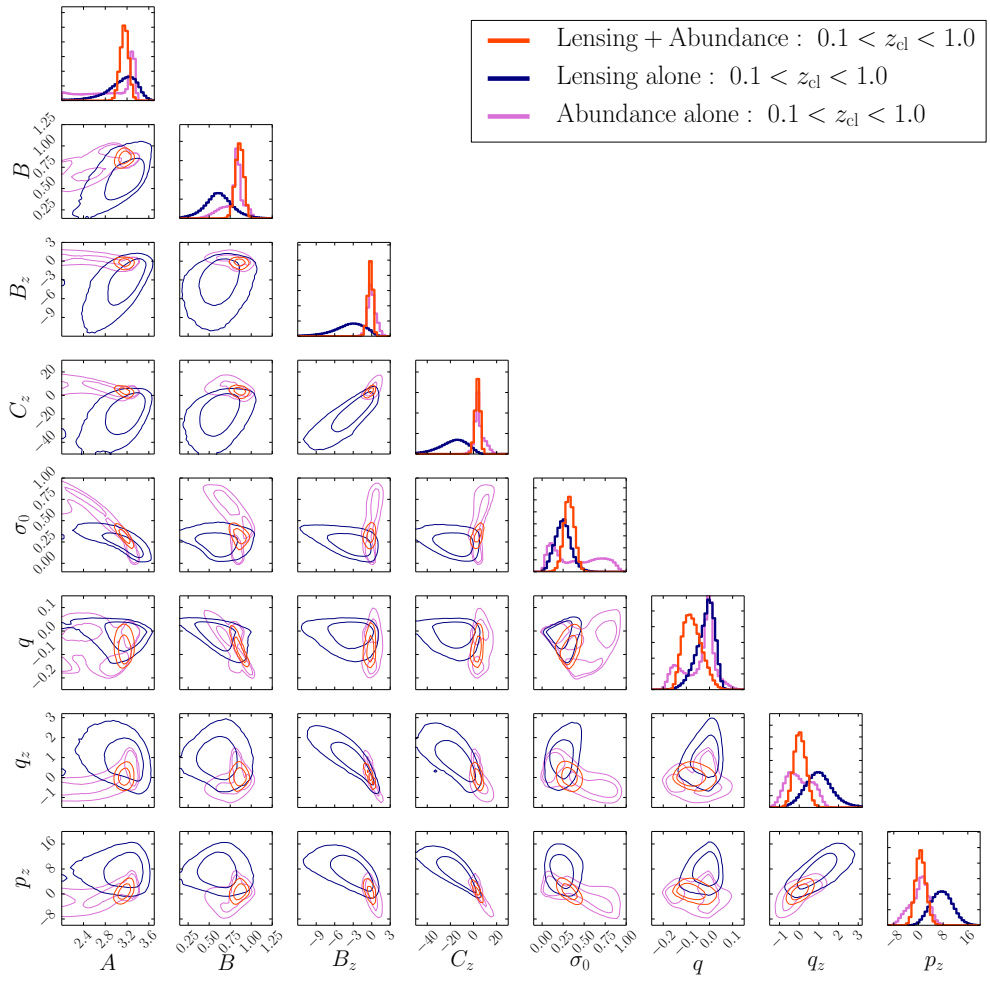

Figure 2.10 Posterior distributions of the richness-mass relation parameters and the 68% and 95% credible level intervals in each two-parameter subspace from the MCMC chains of the fiducial (red), lensing-alone (navy), and abundance-alone (magenta) analyses with the *Planck* cosmological parameters. The minimal prior range of the parameter A is conservatively set to be 2 as shown in Table 2.2, but the abundance-alone analysis has a tail of the distribution at the minimum value of A, mainly due to the substantial flexibility in the adopted model for the richness-mass relation and the weaker constraining power of the abundance on the mean normalization A.

with both linear and square redshift evolution parameters in the fiducial analysis.

With such linear and square redshift evolution parameters, the model prediction can include a non-monotonic dependence on redshift for a fixed mass in $P(\ln N|M,z)$ or a fixed richness in $P_\beta(\ln M|N)$. These non-monotonic behaviors in $P(\ln N|M,z)$ and $P_\beta(\ln M|N)$ are preferred given the significant improvements of $\chi^2_{\rm min}$ by adding the redshift evolution parameters as shown in Figures 2.5, 2.6, 2.7 and 2.8. More specifically, the mean relation $\langle M|N\rangle$ for the middle redshift bin ($0.4 \leq z_{\rm cl} \leq 0.7$) has the $\sim$20% higher amplitude than those for the other redshift bins for both the *Planck* and *WMAP* cosmologies as shown in Figure 2.7 with relatively high significance, whereas the scatter relation $\sigma_{\ln M|N}$ for the middle redshift bin is slightly smaller than those for the other redshift bins. In addition, Figure 2.8 shows the non-monotonic behaviors in the mean and scatter relations of $P(\ln N|M,z)$ as a function of redshift.

A possible explanation for the non-monotonic behavior as a function of redshift is different impacts of

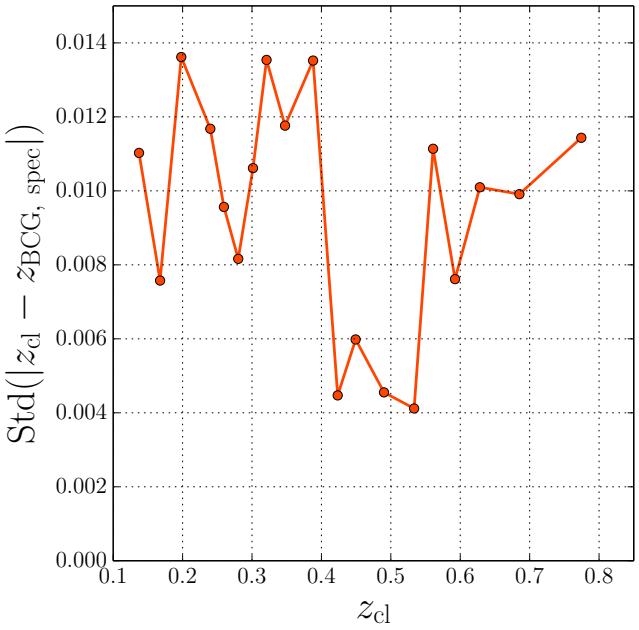

Figure 2.11 Comparison between the photometric cluster redshifts from the CAMIRA algorithm and the available spectroscopic redshifts of BCGs without any clipping. We show standard deviations of the difference between the photometric and spectroscopic redshifts in each photometric redshift bin. Here we use 841 clusters with $N \geq 15$, $0.1 \leq z_{\mathrm{cl}} \leq 1.0$, and spectroscopic redshifts. We use 19 bins that are defined such that each bin includes almost the same number of clusters. The standard deviations around $0.4 \leq z_{\mathrm{cl}} \leq 0.55$ are smaller than those in the lower and higher redshift bins (see text for more details).

projection effects at different cluster redshifts. To illustrate this point, in Figure 2.11 we show a comparison between the photometric cluster redshifts measured from the CAMIRA algorithm and the available spectroscopic redshifts of BCGs without the 4σ clipping done in Oguri et al. (2018a). The standard deviations of the difference between the photometric and spectroscopic redshifts are smaller around $0.4 \leq z_{\mathrm{cl}} \leq 0.55$ than for lower and higher cluster redshifts, which is also a non-monotonic behavior in terms of redshift. The larger errors at high redshifts can be understood by larger errors on galaxy magnitudes, whereas the larger errors at low redshifts are most likely due to the lack of u-band in the HSC survey as well as too-bright galaxy magnitudes (leading to the saturation in some cases) for such low redshifts.

Optical cluster-finding algorithms in imaging surveys essentially use photometric redshifts of individual galaxies to identify cluster member galaxies. The larger cluster photometric redshift errors imply that photometric redshift errors of individual galaxies are also larger, leading to larger contaminations of non-member galaxies along the line-of-sight direction in estimating the cluster richness. Since the photometric redshift errors in the middle redshift bin ($0.4 \leq z_{\mathrm{cl}} \leq 0.7$) are smaller than in the other redshift bins, we expect that CAMIRA separates true member galaxies from non-member galaxies along the line-of-sight direction more effectively in the middle redshift bin. In this case, the mean richness values $\langle \ln N(M,z) \rangle$ should be smaller than those in the other redshift bins for a fixed mass even when non-monotonic behaviors in terms of redshift do not exist for intrinsic richness values (i.e., without non-member galaxies along the line-of-sight direction). This is consistent with the result in Figure 2.8 for the mean relation $\langle \ln N(M,z) \rangle$ for

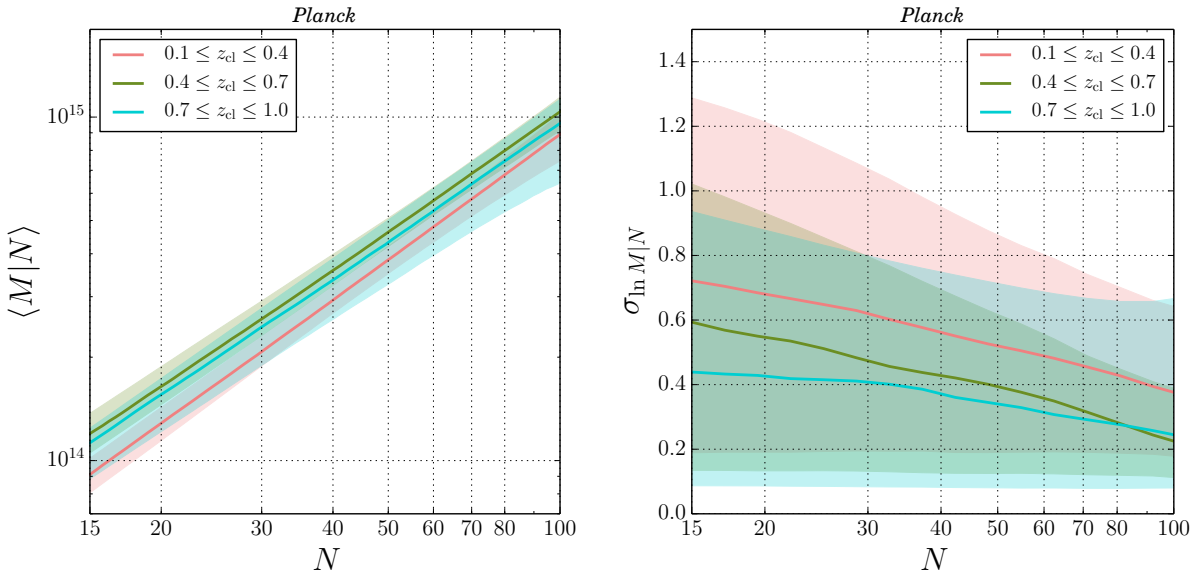

Figure 2.12 The median and the 16th and 84th percentiles of $\langle M|N\rangle$ and $\sigma_{\ln M|N}$ from the analysis of individual redshift bins without redshift evolution parameters in the richness-mass relation, assuming *Planck* cosmology. These results are consistent with the result of our fiducial analysis shown in Figure 2.7.

the typical masses. In addition, the non-monotonic behaviors in the order of the mean relation $P_\beta(\ln M|N)$ in Figure 2.7 might also be interpreted by the explanation above. Specifically, the smaller observed richness for a fixed mass leads to the higher mass for a fixed richness, since we expect a smaller contribution of non-member galaxies to observed richness values at the redshift with smaller photometric redshift errors.

The projection effect modifies not only the mean relation but also the scatter of the richness-mass relation. In particular, the larger projection effect implies larger scatter because the projection effect depends sensitively on the projection direction such that a large projection effect is expected when it is projected along the direction of the filamentary structure. This is also consistent with the results in Figures 2.7 and 2.8, which show slightly smaller scatter values $\sigma_{\ln M|N}$ in the middle redshift bin than the lower and higher redshift bins, and smaller scatter values $\sigma_{\ln N|M,z}$ around $z_{\rm cl} \sim 0.5$ for typical masses, respectively.

To check the robustness of the fiducial result to its parametrization for the redshift evolution, we repeat the MCMC analysis by using only one of the three redshift bins with a simpler richness-mass relation model without redshift evolution parameters (i.e., only A, B, σ_0, and q for the richness mass relation), assuming *Planck* cosmology with the same covariances as the fiducial analysis. This model is similar to the one used in Murata et al. (2018) for SDSS redMaPPer clusters over $0.10 \leq z_{\rm cl} \leq 0.33$. Table 2.3 shows the parameter constraint from this model for each redshift bin. We find that the p-values are acceptable for all redshift bins. Figure 2.12 shows the median and the 16th and 84th percentiles of $\langle M|N\rangle$ and $\sigma_{\ln M|N}$ from the parameter constraints shown in Table 2.3. The mean and scatter constraints shown in Figure 2.12 are consistent with the fiducial result shown in Figure 2.7 within the errors. It is worth noting that the mean relation in the middle redshift bin also favors higher values than for the lower and higher redshift bins, which is similar to

Table 2.3 The median and 68% percentile uncertainties of the model parameters with the *Planck* cosmological parameters when we use the measurements only from one redshift bin. *

Parameter	Low-z	Middle-z	High-z
A	$3.34^{+0.25}_{-0.20}$	$3.19^{+0.20}_{-0.15}$	$3.31^{+0.15}_{-0.26}$
B	$0.85^{+0.08}_{-0.07}$	$0.94^{+0.09}_{-0.07}$	$0.88^{+0.08}_{-0.05}$
σ_0	$0.36^{+0.07}_{-0.21}$	$0.33^{+0.06}_{-0.21}$	$0.27^{+0.14}_{-0.20}$
q	$-0.06^{+0.09}_{-0.11}$	$-0.08^{+0.09}_{-0.09}$	$-0.03^{+0.04}_{-0.11}$
$f_{\rm cen}^{1,\beta}$	$0.52^{+0.18}_{-0.27}$	$0.43^{+0.12}_{-0.21}$	$0.64^{+0.21}_{-0.17}$
$f_{\rm cen}^{2,\beta}$	$0.75^{+0.13}_{-0.35}$	$0.62^{+0.13}_{-0.16}$	$0.39^{+0.20}_{-0.21}$
$f_{\rm cen}^{3,\beta}$	$0.73^{+0.13}_{-0.45}$	$0.86^{+0.09}_{-0.12}$	$0.62^{+0.19}_{-0.24}$
$R_{1,\rm off}$	$0.33^{+0.20}_{-0.24}$	—	—
$R_{2,\rm off}$	—	$0.47^{+0.19}_{-0.20}$	—
$R_{3,\rm off}$	—	—	$0.50^{+0.22}_{-0.25}$
$m_{\rm lens}$	$0.00^{+0.01}_{-0.01}$	$0.00^{+0.01}_{-0.01}$	$0.00^{+0.01}_{-0.01}$
$\chi^2_{\rm min}/{\rm dof}$	30.6/29	25.2/29	34.4/29

* The "Low-z" column shows the results from the lensing and abundance measurements only from $0.1 \leq z_{\rm cl} \leq 0.4$ ($\beta = 1$), "Middle-z" only from $0.4 \leq z_{\rm cl} \leq 0.7$ ($\beta = 2$), and "High-z" only from $0.7 \leq z_{\rm cl} \leq 1.0$ ($\beta = 3$). Here we use the same prior ranges for the model parameters shown in Table 2.2 for the model parameters, whereas we use different parameters of $f_{\rm cen}^{1,\beta}$, $f_{\rm cen}^{2,\beta}$ and $f_{\rm cen}^{3,\beta}$ in equation (2.28) instead of f_0, f_N, and f_z in Table 2.2. We use a flat prior between 0 and 1 for $f_{\rm cen}^{1,\beta}$, $f_{\rm cen}^{2,\beta}$ and $f_{\rm cen}^{3,\beta}$. For these analyses we do not include redshift evolution parameters when fitting the richness-mass relation.

the fiducial results. This result supports the non-monotonic redshift evolution of the richness-mass relation found in our fiducial analysis, although the significance is not very high given the larger errors.

2.7 Chapter summary

In this chapter, we present the results of the richness-mass relation analysis of 1747 HSC CAMIRA clusters in a wide redshift range ($0.1 \leq z_{\rm cl} \leq 1.0$) with a richness range of $N \geq 15$ by jointly fitting to the stacked weak lensing profiles and abundance measurements from the HSC-SSP first-year data ($\sim$232 deg^2 for the cluster catalog and $\sim$140 deg^2 for the shear catalog). The exquisite depth and image quality of the HSC survey enables us to measure stacked weak lensing signals even for high-redshift clusters at $0.7 \leq z_{\rm cl} \leq 1.0$ with a total signal-to-noise ratio of 19.

We constrain the richness-mass relation defined in equations (2.16) and (2.17) assuming a log-normal distribution for the relation $P(\ln N|M, z)$ for both the *Planck* and *WMAP* cosmological parameters, based on a forward modeling method. We constrain the richness-mass relation parameters without informative priors when marginalizing over off-centering effects on the stacked lensing profiles. We employ an N-body simulation-based halo emulator for theoretical predictions of the halo mass function and the lensing profiles. We also use an analytic model for the sample covariance matrix, which is validated against the HSC mock shear and halo catalogs. We find that our model simultaneously fits the stacked lensing profiles and abundance measurements quite well for both the *Planck* and *WMAP* cosmological parameters with $\chi^2_{\rm min}/{\rm dof} = 107.0/97$ and $\chi^2_{\rm min}/{\rm dof} = 106.6/97$, respectively. We check the robustness of the results against the choice of different photo-z catalogs and source selection cuts. We also show how the stacked lensing and

abundance measurements individually constrain the model parameters, and show that the joint analysis efficiently breaks the richness-mass parameter degeneracies.

We then derive the mass-richness relation $P_\beta(\ln M|N)$ in each redshift bin, using Bayes theorem from the constraint on $P(\ln M|N,z)$. We show that the mean relations $\langle M|N\rangle$ in each redshift bin are consistent between the *Planck* and *WMAP* cosmological parameters within the errors, but the scatter relation values $\sigma_{\ln M|N}$ for the *Planck* cosmological model are larger than those for the *WMAP* model. In addition, scatter values for the *Planck* model increase toward lower richness values, whereas those for the *WMAP* model are consistent with constant values as a function of richness.

We also show that we need to include the linear and square redshift-dependent parameters in terms of $\ln(1+z)$ for the mean and scatter relations in $P(\ln N|M,z)$ to have acceptable p-values. The models without such redshift-dependent parameters resulted in much worse p-values. By including the square redshift-dependent parameters, we show that the mean relation $\langle M|N\rangle$ in the middle redshift bin has $\sim$20% higher amplitude than in the lower and higher redshift bins, whereas the scatter relation $\sigma_{\ln M|N}$ in the middle redshift bin is slightly smaller than in the other bins. We ascribe this non-monotonic redshift dependence to the non-monotonic behavior of the projection effect as a function of redshift, which is supported by the redshift dependence of cluster photometric redshift errors. Redshift evolution in the mean relation $\langle M|N\rangle$ should be properly accounted for when one uses the stacked weak lensing signals around the HSC CAMIRA clusters to validate shear and photo-z catalogs, or to define source selection cuts (e.g., Medezinski et al., 2018b), by matching the cluster weight distributions in terms of cluster redshift and richness values. We also check the consistency of our fiducial results based on the richness-mass relation including the redshift-dependent parameters with those from the analysis of individual redshift bins without redshift-dependent parameters.

Our results indicate that we cannot distinguish between *Planck* and *WMAP* cosmological models from the current abundance and lensing profile measurements. This is partly because of our choice of a flexible richness-mass relation model without any informative prior constraints on the model parameters. However, we find that the predicted scatter values are clearly different between *Planck* and *WMAP* cosmologies, suggesting that any additional constraints on the scatter of the mass-richness relation may break the degeneracy between these two cosmological models. For instance, one could add other independent probes (e.g., X-ray temperature, the Sunyaev–Zel'dovich effect, or lensing magnification effect) for constraining the scatter values in order to distinguish cosmological models from cluster observables. The analysis of lensing magnification effect might provide complementary information, and will constrain the richness-mass relation of the HSC CAMIRA clusters (Chiu et al. *in prep.*).

Another possible observable to break the degeneracy is spatial clustering of clusters. Here we briefly investigate the difference of the real-space three-dimensional halo-halo correlation function $\xi_{\rm hh}(r)$ in each redshift and richness bin between the *Planck* and *WMAP* models by using the best-fit richness-mass relation parameters from the fiducial analyses in this chapter, to roughly assess its power to break the degeneracy.

We find that the predicted amplitudes of the halo-halo correlation function for the *WMAP* model are ∼20–30% larger than those for the *Planck* model for all richness and redshift bins at $3 \lesssim r \lesssim 50h^{-1}$Mpc. This implies that clustering of clusters adds useful information that is complementary to abundance and lensing, although careful investigations of cluster photo-z accuracy, redshift-space distortions, and projection effects should be conducted in order to combine our results with the cluster clustering analysis to obtain tight cosmological constraints. We leave this exploration for future work.

In addition, our result should be useful for other cluster-related observational studies (e.g., Lin et al., 2017; Jian et al., 2018; Nishizawa et al., 2018; Miyaoka et al., 2018; Ota et al., 2018; Hashimoto et al., 2019), including galaxy formation in cluster regions and the mass scale estimation for clusters detected via strong-lensing, X-ray, and Sunyaev–Zel'dovich effect with richness values. We can also use our constraint on $P(\ln N|M, z)$ to construct mock CAMIRA cluster catalogs with richness values by using halo mass and redshift in N-body simulations, which may be useful for testing the performance of cluster-finding algorithms with simulations (e.g., Dietrich et al., 2014; Oguri et al., 2018a; Costanzi et al., 2019).

Our analysis involves several assumptions. Most critically, we have assumed that the CAMIRA clusters are randomly oriented with respect to the line-of-sight direction in the forward modeling method to compute the cluster observables from the mass function and the spherically averaged halo-matter cross-correlation function from N-body simulation outputs. However, this assumption is inaccurate if the CAMIRA clusters are affected by projections effects such as misidentification of non-member galaxies along the line-of-sight direction as member galaxies in the richness estimation (e.g., Cohn et al., 2007; Zu et al., 2017; Busch & White, 2017; Costanzi et al., 2019; Sunayama & More, 2019). Since our cluster selection is based on richness values, CAMIRA could preferentially detect clusters with filamentary structure along the line-of-sight direction. Given the correlation between the halo orientation and surrounding large-scale structure, this effect can change the lensing profile from the spherically-symmetric case (Osato et al., 2018). This investigation is beyond the scope of this thesis. Further careful investigations of projection effects for the mass-richness relation are warranted. In order to properly address the projection effects, we need to construct realistic mock catalogs of the CAMIRA clusters with intrinsic richness values and to derive cluster observables accounting for the projection effects. Our results might be useful to check the consistency of such simulation setups with the observations by comparing our measurements and constraints on the mean and scatter relations with ones from such mock catalogs with projection effects.

We have presented a richness-mass relation analysis from HSC first-year data. We will have ∼1000 deg^2 area for cluster and shear catalogs when the HSC-SSP survey is complete in 2020. The final HSC cluster analysis has the potential to provide stronger constraints on the richness-mass relation and its better applications for cosmological, galaxy formation, and cluster-related studies particularly when combined with other probes. There is also room for improving the measurement methods e.g., improving the shear measurement technique to include more galaxy shapes, and increasing the sample of galaxies with spectroscopic redshifts independent from the COSMOS 30-band catalog to improve and understand the accuracy

of cluster photometric redshifts, and also improving the model framework by further accounting for possible systematic effects such as projection effects.

Chapter 3

The splashback radius of optically selected clusters with Subaru HSC Second Public Data Release

We refer to Murata et al. (2020) for this chapter in this censored version of the thesis.

Chapter 4

Summary and Conclusion

Recent observational constraints in the last five years on the splashback radius around optically selected galaxy clusters from the redMaPPer cluster-finding algorithm have shown that the observed splashback radius is $\sim 20\%$ smaller than that predicted by N-body simulations under the ΛCDM standard cosmological model at a high significance ($\sim 4\sigma$), with the help of the mass-richness relation from weak gravitational lensing effects.

In this thesis, we have presented observational and statistical studies of optically selected galaxy clusters on the mass-richness relation and the splashback radius as a test of the ΛCDM model with simplified mock simulation analyses to investigate the selection bias effects of the CAMIRA and redMaPPer cluster-finding algorithms on the splashback radius in observations.

For this purpose, we employ the data catalogs from the ongoing HSC-SSP for optically selected galaxy clusters, weak lensing analyses, and photometric galaxies. We use ~ 2000 optically selected galaxy clusters from the independent cluster-finding algorithm CAMIRA at a wide cluster redshift range of $0.1 < z_{\rm cl} < 1.0$ thanks to deep and high-resolution HSC images, whereas previous observational works in the literature on the mass-richness relation and the splashback radius are limited to $z_{\rm cl} \lesssim 0.7$.

We firstly list our main findings and achievements in Chapter 2 as follows:

- We measure stacked weak lensing profiles around the HSC CAMIRA clusters over the wide redshift range and we detect lensing signals around high-redshift clusters at $0.7 < z_{\rm cl} < 1.0$ with a signal-to-noise ratio of 19.

- We constrain the richness-mass relations $P(\ln N|M, z_{\rm cl})$ of the HSC CAMIRA clusters assuming a log-normal distribution without informative priors on model parameters, by jointly fitting to the lensing profiles and abundance measurements under two different sets of cosmological parameters for the ΛCDM model based on the CMB measurements from the *Planck* and *WMAP* satellites.

- We show that constraints on the mean relation $\langle M|N\rangle$ with a precision of $\sim 5\%$ for each model are consistent between the *Planck* and *WMAP* models, whereas the scatter values $\sigma_{\ln M|N}$ for the

Planck model are systematically larger than those for the *WMAP* model, which is consistent with the literature. Furthermore, we show that the scatter values for the *Planck* model increase toward lower richness values when employing our flexible parametrization for the mass-richness relation, whereas those for the *WMAP* model are consistent with constant values as a function of richness. This result highlights the importance of the scatter in the mass-richness relation to constrain the cosmological parameters from galaxy clusters.

- Our constraint on the mass-richness relation is useful to infer masses of observed galaxy clusters as a bridge between theories and observations.

We secondly list our main findings and achievements in Chapter 3 with the help of the results of Chapter 2 as follows:

- We detect the splashback feature from the projected cross-correlation measurements between the clusters and photometric galaxies over the wide redshift range, including for high redshift clusters at $0.7 < z_{\rm cl} < 1.0$, thanks to deep HSC images. We investigate the dependence of splashback features on cluster redshift, richness, galaxy magnitude limits, and galaxy colors over the wide redshift range.

- We find that constraints from red galaxy populations only are more precise than those without any color cut, leading to 1σ precisions of $\sim 15\%$ for cluster samples at $0.4 < z_{\rm cl} < 0.7$ and $0.7 < z_{\rm cl} < 1.0$. We also find that these constraints at $0.4 < z_{\rm cl} < 0.7$ and $0.7 < z_{\rm cl} < 1.0$ are more consistent with our model predictions in the ΛCDM model with the help of our mass-richness relation ($\lesssim 1\sigma$) than their 20% smaller values as suggested by the previous studies based on redMaPPer clusters ($\sim 2\sigma$ for CAMIRA clusters).

- We establish a methodology to investigate selection effects of simplified optical cluster-finding algorithms on the observed splashback features in mock simulations by creating a mock galaxy catalog from a halo occupation distribution model and for the first time closely resembling the procedure in data analyses and model prediction calculations with the real data. With this methodology, we find that such effects are insignificant for the simplified CAMIRA cluster-finding algorithm within our statistical errors in the observational data analyses. We also find that the redMaPPer-like cluster-finding algorithm induces a smaller inferred splashback radius in our mock catalog at the level of $\sim 15\%$, which well explains smaller splashback radii in the literature, whereas these biases are significantly reduced when increasing its aperture size. This finding suggests that aperture sizes of optical cluster finders that are smaller than splashback feature scales should induce significant biases on the inferred location of splashback radius.

Based on our findings, for the first time we conclude that the observed splashback radii are consistent with the theoretical predictions based on the ΛCDM standard cosmological model and our mass-richness relation from weak lensing effects for the HSC CAMIRA clusters at our precisions over the wide redshift range

($\sim 15\%$ for each bin of $0.1 < z_{\rm cl} < 0.4$, $0.4 < z_{\rm cl} < 0.7$, and $0.7 < z_{\rm cl} < 1.0$), and this is also the case for the redMaPPer clusters in the literature when accounting for the selection bias effects of the redMaPPer cluster-finding algorithm, which we find in our mock simulation analyses.

We can improve the precisions on measurements to explore the consistency with the ΛCDM model more precisely by employing the upcoming full HSC survey data or other future survey data in various wavelengths including X-ray and radio, in order to study cosmological and astrophysical aspects of galaxy clusters and the Universe itself in more detail. Our observational results with the CAMIRA clusters and our analysis frameworks and methodology are informative to conduct such analyses with properly accounting for the selection effects in the near future.

Acknowledgements

This thesis would not have been realized without the support and published works of many people.

I would like to express my deepest gratitude and respect to my mentors Professor Masamune Oguri and Professor Surhud More for their continuous support and encouragement over my research period in various aspects, and their valuable comments and feedback for the original paper drafts. I also acknowledge my supervisor Professor Masahiro Takada, who introduced me to this exciting research field five years ago.

I would also like to thank the other collaborators, Rachel Mandelbaum, Takahiro Nishimichi, Atsushi J. Nishizawa, Ken Osato, Masato Shirasaki, and Tomomi Sunayama, for fruitful discussions with me and their comments on the original paper drafts.

I would like to thank simulation contributions of Japanese researchers in their published papers to construct the halo emulator, the halo catalog, and the full-sky gravitational lensing map, which I employ in the original papers and this thesis. I acknowledge Tomomi Sunayama for creating mock galaxy cluster catalogs from a galaxy catalog which I create in Chapter 3 to investigate projection effects on the splashback radius with a method developed in her published work with Surhud More for my subsequent analyses.

I sincerely acknowledge Dominik Zürcher for sharing his codes developed for his published work with Surhud More before further developments by myself for the original paper and this thesis.

I express my sincere gratitude to the contributions of many people for their published works related to this thesis on their hardware developments, telescope maintenance, survey design, observations, image analysis pipeline developments, data validations, database management, and galaxy, cluster, galaxy lensing shear, and galaxy photometric redshift catalog constructions. The Hyper Suprime-Cam (HSC) collaboration includes the astronomical communities of Japan and Taiwan, and Princeton University. The HSC instrumentation and software were developed by the National Astronomical Observatory of Japan (NAOJ), the Kavli Institute for the Physics and Mathematics of the Universe (Kavli IPMU), the University of Tokyo, the High Energy Accelerator Research Organization (KEK), the Academia Sinica Institute for Astronomy and Astrophysics in Taiwan (ASIAA), and Princeton University. Funding was contributed by the FIRST program from Japanese Cabinet Office, the Ministry of Education, Culture, Sports, Science and Technology (MEXT), the Japan Society for the Promotion of Science (JSPS), Japan Science and Technology Agency (JST), the Toray Science Foundation, NAOJ, Kavli IPMU, KEK, ASIAA, and Princeton University. This paper makes use of software developed for the Large Synoptic Survey Telescope. We thank the LSST Project

for making their code available as free software at http://dm.lsst.org. The Pan-STARRS1 Surveys (PS1) have been made possible through contributions of the Institute for Astronomy, the University of Hawaii, the Pan-STARRS Project Office, the Max-Planck Society and its participating institutes, the Max Planck Institute for Astronomy, Heidelberg and the Max Planck Institute for Extraterrestrial Physics, Garching, The Johns Hopkins University, Durham University, the University of Edinburgh, Queen's University Belfast, the Harvard-Smithsonian Center for Astrophysics, the Las Cumbres Observatory Global Telescope Network Incorporated, the National Central University of Taiwan, the Space Telescope Science Institute, the National Aeronautics and Space Administration under Grant No. NNX08AR22G issued through the Planetary Science Division of the NASA Science Mission Directorate, the National Science Foundation under Grant No. AST-1238877, the University of Maryland, and Eotvos Lorand University (ELTE) and the Los Alamos National Laboratory. Based on data collected at the Subaru Telescope and retrieved from the HSC data archive system, which is operated by Subaru Telescope and Astronomy Data Center, National Astronomical Observatory of Japan.

I acknowledge financial support from the University of Tokyo-Princeton strategic partnership grant, Advanced Leading Graduate Course for Photon Science (ALPS), Research Fellowships of the Japan Society for the Promotion of Science for Young Scientists (JSPS), and JSPS Overseas Challenge Program for Young Researchers in order to accomplish the original paper drafts for this thesis. This work was supported by JSPS KAKENHI Grant Numbers JP17J00658. This work was supported by World Premier International Research Center Initiative (WPI Initiative), MEXT, Japan. Numerical computations were in part carried out on Cray XC30 and XC50 at Center for Computational Astrophysics, National Astronomical Observatory of Japan.

I also thank Hiroko Niikura, Xiangchong Li, and Masataka Aizawa for encouragement over my research period at Kavli IPMU or Hongo.

I also express my deep gratitude to Professor Naoki Yasuda, and Tatsuhiro Thomas Yano and the IT team at Kavli IPMU, who enable me to use data analysis servers, which are indispensable to this thesis.

I also sincerely appreciate Professor Akira Furusawa as my ALPS advisor, who have spent more than thirty minutes whenever I talk with him on some issues when I have or my career with continuous warm encouragement.

I would sincerely appreciate the Professors in my thesis refereeing committee, Fujihiro Hamba, Kipp Cannon, Akito Kusaka, Masami Ouchi, and Masahiro Teshima, for their helpful comments and suggestions that improved the quality of this thesis.

Finally, I am very grateful to my family and relatives for supporting me financially in the past and mentally. I also thank all people who have always supported me to continue my research. Especially I greatly thank Ayako Yamamoto for being with me throughout my days for more than fifteen years. This thesis would have never been accomplished without her support and smile. This thesis is dedicated to the memory of my dear mother with my sincere and deepest gratitude.

Appendix A

Optical cluster-finding algorithm

The CAMIRA algorithm (Oguri, 2014; Oguri et al., 2018a) is a red-sequence cluster finder based on a stellar population synthesis model (Bruzual & Charlot, 2003) to predict colors of red-sequence galaxies at a given redshift and to compute likelihoods of being red-sequence galaxies as a function of redshift. The stellar population synthesis model gives us how to interpret the observed spectral energy distribution from a given galaxy based on the theory of stellar evolution. In addition, Oguri et al. (2018a) calibrated the stellar population synthesis model with spectroscopic galaxies to improve its accuracy (see Figures A.1, A.2, and A.3 below for more details).

In the CAMIRA algorithm, the richness corresponds to the number of red member galaxies with stellar mass $M_* \gtrsim 10^{10.2} M_\odot$ (roughly corresponding to a luminosity range of $L \gtrsim 0.2 L_*$) within a circular aperture with radius $R \lesssim 1\ h^{-1}$Mpc in physical coordinates. This luminosity range is based on the result in Rykoff et al. (2012) by minimizing the scatter of X-ray luminosity at a fixed richness for massive clusters with X-ray images. The CAMIRA algorithm does not include a richness-dependent scale radius to define the richness, unlike the redMaPPer algorithm (Rykoff et al., 2012). The HSC images are deep enough to detect cluster member galaxies down to $M_* \sim 10^{10.2} M_\odot$ even at a cluster redshift $z_{\rm cl} \sim 1$, which allows a reliable cluster detection at such high redshifts without a richness incompleteness correction. The algorithm employs a spatially-compensated filter such that the background level is automatically subtracted in deriving the richness as shown Figure A.4.

The CAMIRA algorithm identifies the brightest cluster galaxy (BCG) for each cluster candidate that is defined by a peak in the three-dimensional richness map in RA, dec, and redshift space (Oguri, 2014; Oguri et al., 2018a). The cluster centers are defined as the locations of the identified BCGs. The mask-corrected richness N and cluster photometric redshift $z_{\rm cl}$ are refined iteratively during the BCG identification process. The offset of BCG positions from matched X-ray cluster centers is investigated in Oguri et al. (2018a). The bias and scatter in photometric cluster redshifts of $\Delta z_{\rm cl}/(1+z_{\rm cl})$ are shown to be better than 0.005 and 0.01 respectively with 4σ clipping over most of the redshift range by using available spectroscopic redshifts of BCGs.

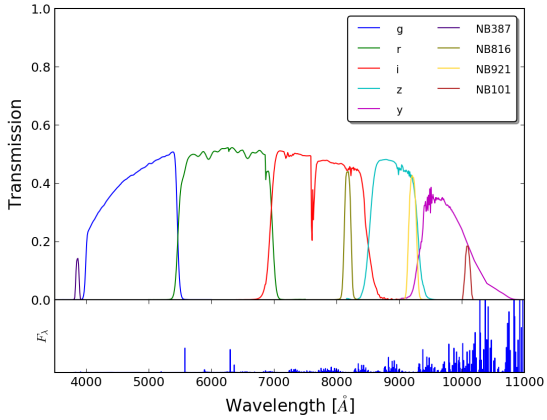

Figure A.1 The HSC bandpasses. This figure accounts for the reflectivity of all mirrors, transmission of all optics, filters, the response of CCD, and a typical atmosphere. The lower panel shows the spectrum of sky emission lines. In this thesis, we use data catalogs related to the five broadbands: *grizy*. Redshifted wavelengths of the 4000Å break in the spectrum of galaxies correspond to the filter transitions at $z_{\rm cl} \simeq 0.4$ (from g-band to r-band), $z_{\rm cl} \simeq 0.7$ (from r-band to i-band), and $z_{\rm cl} \simeq 1.0$ (from i-band to z-band). The 4000Å break is a pronounced discontinuity in the spectra of stellar populations due to the absorption of high energy radiation from metals in the stellar atmospheres and the lack of hot young stars as the main feature of galaxy spectra. The amplitude of the 4000Å break depends on the mean stellar age and metallicity of a galaxy. This figure is reproduced from Figure 2 in Aihara et al. (2018a).

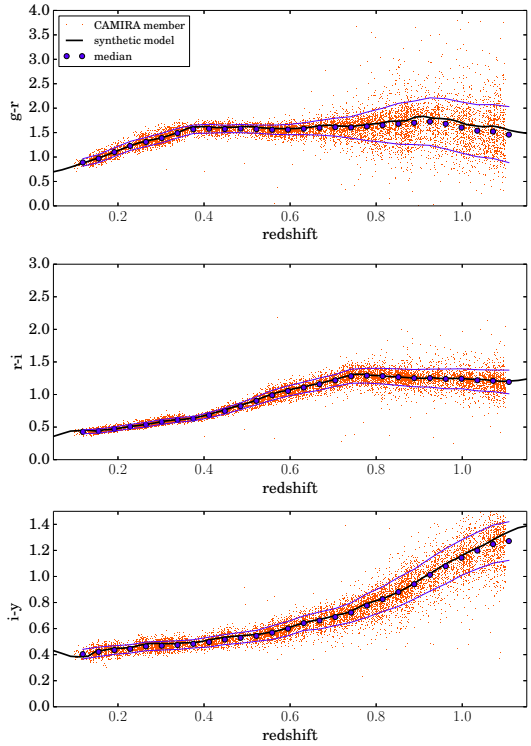

Figure A.2 The relation between redshift and color of red-sequence member galaxies identified by the CAMIRA cluster-finding algorithm. Red points are CAMIRA cluster member galaxies. The thick solid lines are the model colors from the stellar population synthesis model (Bruzual & Charlot, 2003) after calibrations with available spectroscopic redshifts (Oguri et al., 2018a). The median colors of g–r, r–i, and i–y change rapidly at cluster redshifts $0.1 < z_{\rm cl} < 0.4$, $0.4 < z_{\rm cl} < 0.7$, and $0.7 < z_{\rm cl} < 1.0$ since the HSC filter set in Figure A.1 straddles redshifted wavelengths of the 4000Å break. Then, these color combinations for each redshift bin above have information to estimate cluster redshifts based on the calibrated stellar population synthesis model, as shown in red points for the CAMIRA member galaxies. This figure is reproduced from Figure 2 in Nishizawa et al. (2018).

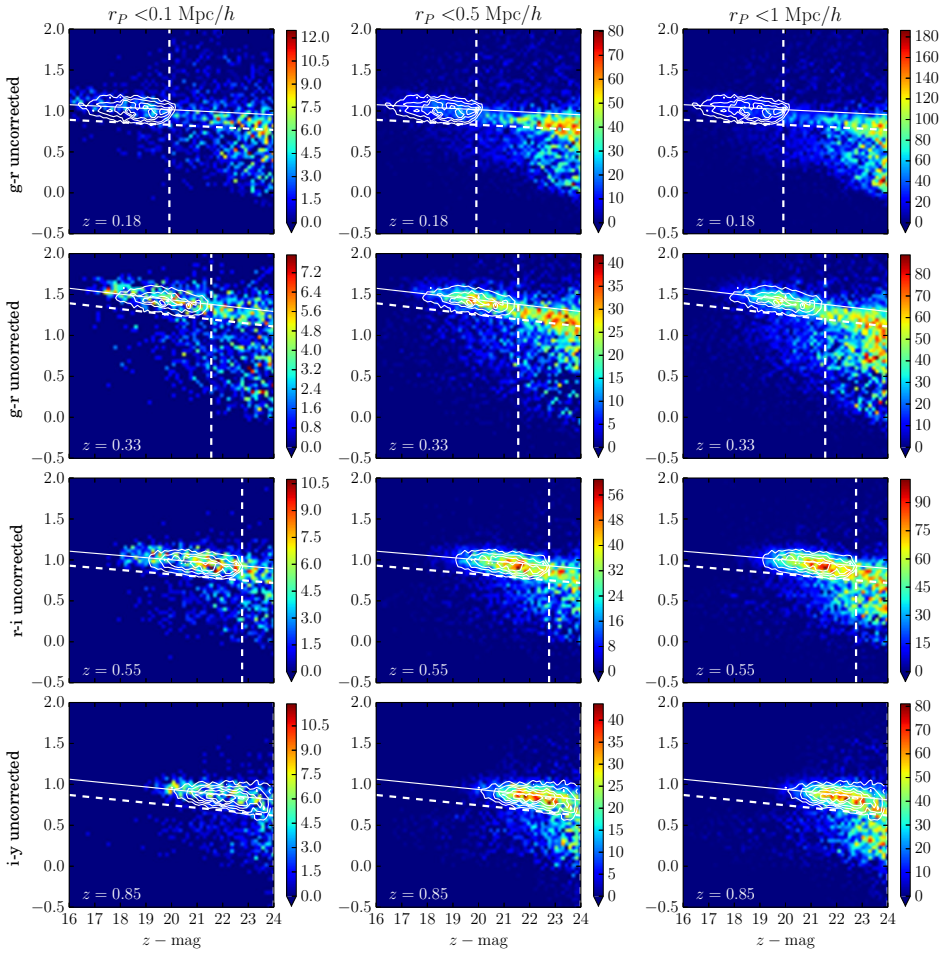

Figure A.3 Color-magnitude diagrams that are derived by stacking photometric galaxies around all CAMIRA clusters in Nishizawa et al. (2018) at different cluster redshifts and radial ranges from centers of galaxy clusters. Color levels show the number of correlated galaxies around CAMIRA galaxy clusters. Overlaid contours in each panel show the distribution of red-sequence cluster member galaxies identified by CAMIRA. In this thesis, we define red and blue galaxy populations for each redshift bin by those above and below the dashed line (a line 2σ below the solid line), respectively, in Chapter **??** based on Nishizawa et al. (2018). Vertical dotted lines are an apparent magnitude cut employed in Nishizawa et al. (2018). This figure is reproduced from Figure 3 in Nishizawa et al. (2018).

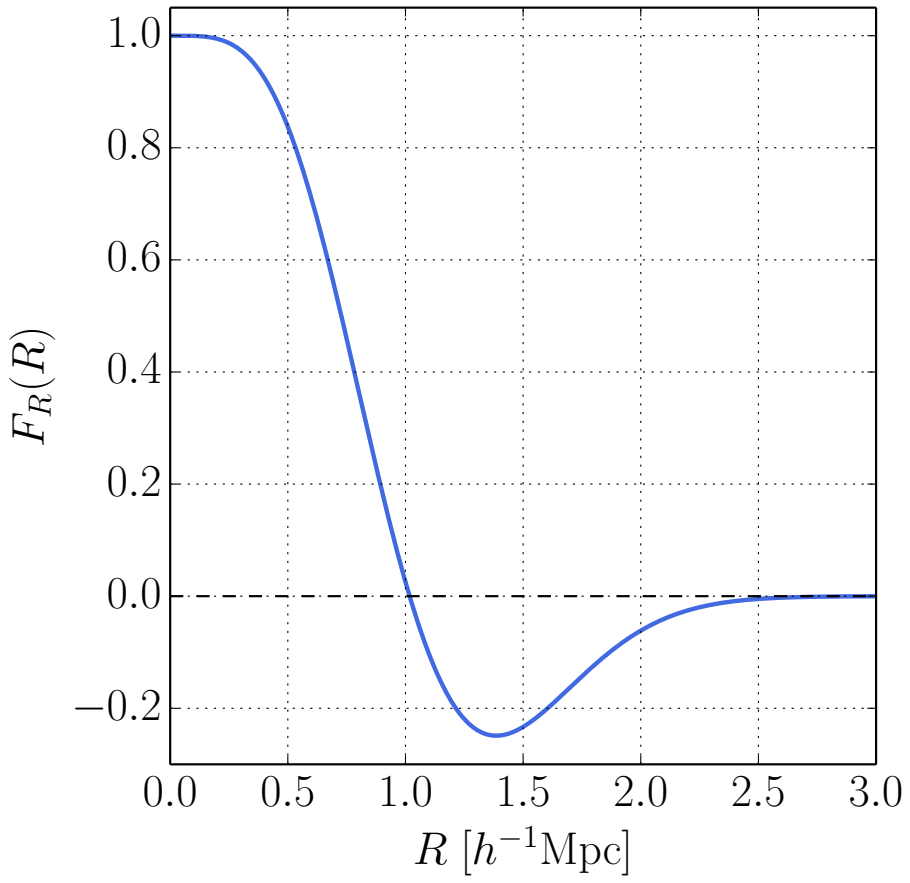

Figure A.4 The radial filter (a weighting function) for the CAMIRA cluster-finding algorithm in equation (**??**) to count red-sequence galaxies around estimated centers of galaxy clusters in the optical cluster-finding. Note that the x-axis shows a distance from estimated centers of galaxy clusters in physical coordinates.

Appendix B

Weak gravitational lensing

We briefly review the weak gravitational lensing. We use weak gravitational lensing measurements around the CAMIRA clusters in Chapter 2 to constrain the mass-richness relation of the CAMIRA clusters. We refer to review papers, e.g., Bartelmann & Schneider (2001), Schneider (2006), Kilbinger (2015), and Mandelbaum (2018b) for more details.

B.1 Overview

Gravitational lensing is the unique means of unveiling the distribution of dark matter in the universe. This effect is based on General Relativity. The gravitational field along line-of-sight directions bends the path of light rays by distorting space-time. Consequently, the gravitational lensing causes a coherent distortion in observed images of galaxies, since the degree of lensing effects is stronger for light rays closer to gravitational sources (e.g., galaxy clusters) in projected lengths even within a galaxy image. Thus, by measuring the coherent distortion pattern in the galaxy shapes of background galaxies, we can recover the distribution of the foreground matter, including both baryon and dark matter, and we can estimate masses of galaxy clusters for the mass-richness relation for instance. The effect is independent of the nature and dynamical state of matter, allowing us to estimate masses of dark matter halos with weaker assumptions than other methods (e.g., hydrodynamical masses from X-ray). With the gravitational lensing effects, we can probe dark matter directly via gravitational fields with telescopes though dark matter does not emit light like stars and galaxies.

In general, there are two regimes of gravitational lensing: strong and weak. In strong lensing, the background image is strongly distorted into rings or arcs, when the source, lens, and the observer are closely aligned. In this case, the lensing can divide the images into multiple ones. In weak lensing, there are only the effects of small systematic distortion on the single source in response to foreground gravitational fields. Hence, this effect cannot be distinguished on an individual galaxy basis, since the lensing effect is typically smaller than the intrinsic shape of the source. After stacking (averaging) over these effects from many

background galaxies, we can recover these weak lensing signals by reducing the intrinsic shape noise.

In this thesis, we focus on weak gravitational lensing to constrain the mass-richness relation of the CAMIRA clusters in Chapter 2. The weak gravitational lensing can map the spatial distribution around galaxy clusters at scales from $\sim 0.1\ h^{-1}$Mpc to $\sim 50\ h^{-1}$Mpc in the angular comoving distance. Thus, we can employ this phenomenon to study the mass and density profile of galaxy clusters (i.e., their host dark matter halos), especially to constrain the mass-richness relation in Chapter 2 for the splashback feature analyses in Chapter 3.

B.2 Lens equation

In the thin lens approximation, where the light is deflected only at the lens plane, and Born approximation, the deflection of light by a point object of mass M is given as,

$$\begin{aligned}\hat{\alpha} &= -2\frac{\partial}{\partial\xi}\int_{-\infty}^{\infty}\mathrm{d}z\frac{GM}{\sqrt{\xi^2+z^2}} \\ &= \frac{4GM}{\xi} \\ &= 1.75''\left(\frac{M}{M_\odot}\right)\left(\frac{\xi}{R_\odot}\right)^{-1} \\ &= 2\hat{\alpha}_N, \end{aligned} \tag{B.1}$$

where ξ is the impact parameter (the distance between the light and the lens at the lens plane), $\hat{\alpha}_N$ is the prediction of the Newtonian value, and the direction of z is along with the line-of-sight direction from observers (i.e., telescopes and us). The thin lens approximation is, in general, a valid assumption since a typical size of galaxy clusters ($\sim 1\ h^{-1}$Mpc) is much smaller than a typical distance from background galaxies to us ($\sim 1\ h^{-1}$Gpc). Figure B.1 shows this configuration.

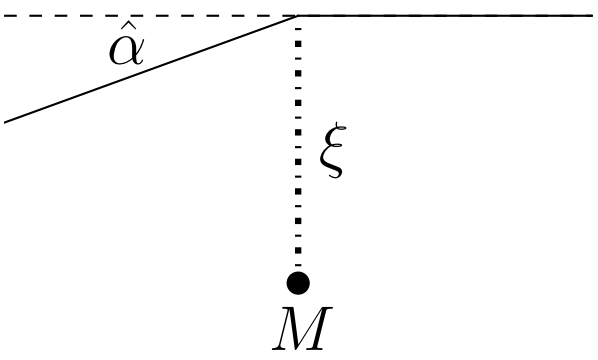

Figure B.1 The deflection angle by the lensing from a point mass. The mass is M. The impact parameter is ξ. The gravitational field induced by the point mass causes the deflection denoted by $\hat{\alpha}$. Note that the deflection angle $\hat{\alpha}$ in this figure is larger than the reality for the visualization.

In the case of weak gravitational field (i.e., small deflection angles), the deflection angle of a light with spatial trajectory $\vec{r} = (\xi_1(\lambda), \xi_2(\lambda), r_3(\lambda))$ with the affine parameter λ passing though the three-dimensional

mass density $\rho(\vec{r'})$ is given from the generalization of equation (B.1) as,

$$\vec{\hat{\alpha}}(\vec{\xi}) = 4G \int \mathrm{d}^2\xi' \int \mathrm{d}r_3' \; \rho(\xi_1', \xi_2', r_3') \frac{\vec{\xi} - \vec{\xi'}}{|\vec{\xi} - \vec{\xi'}|^2}. \tag{B.2}$$

The surface mass density is defined as the projected mass density on to the lens plane:

$$\Sigma(\vec{\xi}) = \int \mathrm{d}r_3 \; \rho(\xi_1, \xi_2, r_3). \tag{B.3}$$

Then, equation (B.2) can be written as,

$$\vec{\hat{\alpha}}(\vec{\xi}) = 4G \int \mathrm{d}^2\xi' \Sigma(\vec{\xi'}) \frac{\vec{\xi} - \vec{\xi'}}{|\vec{\xi} - \vec{\xi'}|^2}. \tag{B.4}$$

From the simple geometry and a tiny value of the deflection angle in equation (B.1), the relation between the angular coordinates on the source and lens planes are calculated:

$$\vec{\beta} = \vec{\theta} - \vec{\alpha}(\vec{\theta}), \tag{B.5}$$

where $\vec{\beta}$ is the angular position of the source, $\vec{\theta}$ is the observed angular position of the image, and $\vec{\alpha}(\vec{\theta})$ is the scaled deflection angle :

$$\vec{\alpha}(\vec{\theta}) \equiv \frac{D_{\mathrm{ds}}}{D_{\mathrm{s}}} \vec{\hat{\alpha}}(D_{\mathrm{d}}\vec{\theta}). \tag{B.6}$$

Here we define the angular diameter distance between the observer, as one with the lens (D_{d}), one between the observer and the source (D_{s}), and one between the lens and the source (D_{ds}). Figure B.2 shows the configuration.

From equations (B.4) and (B.6), the scaled deflection angle is given as follows,

$$\vec{\alpha}(\vec{\theta}) = \frac{1}{\pi} \int \mathrm{d}^2\theta' \kappa(\theta') \frac{\vec{\theta} - \vec{\theta'}}{|\vec{\theta} - \vec{\theta'}|^2}, \tag{B.7}$$

where convergence and critical surface mass density are given as respectively,

$$\kappa(\vec{\theta}) = \frac{\Sigma(D_{\mathrm{d}}\vec{\theta})}{\Sigma_{\mathrm{cr}}}, \tag{B.8}$$

and

$$\Sigma_{\mathrm{cr}} = \frac{1}{4\pi G} \frac{D_{\mathrm{s}}}{D_{\mathrm{d}} D_{\mathrm{ds}}}. \tag{B.9}$$

In the weak lensing regime, $|\kappa| \ll 1$. From $\vec{\nabla} \ln|\vec{\theta}| = \vec{\theta}/|\vec{\theta}^2|$, where $\vec{\nabla} \equiv \vec{\nabla}_{\vec{\theta}}$, we can introduce a scalar lens potential $\psi(\vec{\theta})$:

$$\vec{\alpha}(\vec{\theta}) = \vec{\nabla}\psi(\vec{\theta}), \tag{B.10}$$

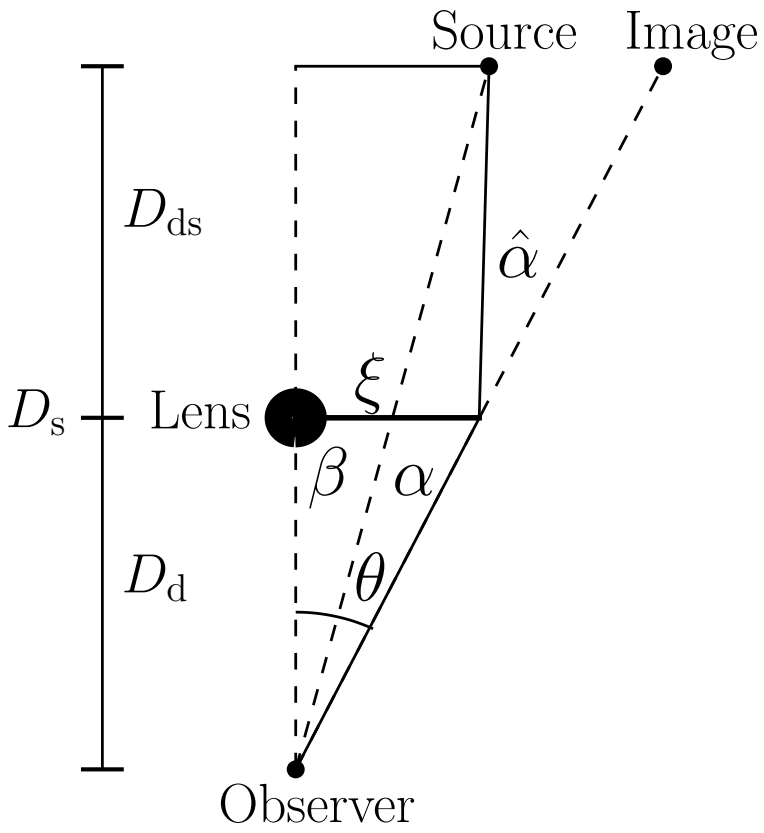

Figure B.2 The configuration of the lens system in equation (B.5). Note that the deflection angle $\hat{\alpha}$ in this figure is larger than the reality for the visualization.

where

$$\psi(\vec{\theta}) = \frac{1}{\pi}\int \mathrm{d}^2\vec{\theta}'\,\kappa(\vec{\theta}')\ln|\vec{\theta}-\vec{\theta}'|. \tag{B.11}$$

Since $\ln|\vec{\theta}|$ is the Green function, the convergence is related to the second derivative of the lens potential:

$$\kappa = \frac{1}{2}(\psi_{,11}+\psi_{,22}) = \frac{1}{2}\nabla^2\psi, \tag{B.12}$$

where ",1" and ",2" denote the derivation with respect to θ_1 and θ_2, respectively.

B.3 Distortion of finite image sizes: shear

The change of shape by the lensing is described by the Jacobian matrix:

$$\mathcal{A}(\vec{\theta}) = \frac{\partial\vec{\beta}}{\partial\vec{\theta}} \tag{B.13}$$

with the components $\mathcal{A}_{ij} = \partial\beta_i/\partial\theta_j$. From equation (B.5), we obtain

$$\begin{aligned}\mathcal{A} &= \begin{pmatrix} 1-\kappa-\gamma_1 & -\gamma_2 \\ -\gamma_2 & 1-\kappa+\gamma_1 \end{pmatrix}, \\ &= \begin{pmatrix} 1-\kappa & 0 \\ 0 & 1-\kappa \end{pmatrix} + \begin{pmatrix} -\gamma_1 & 0 \\ 0 & \gamma_1 \end{pmatrix} + \begin{pmatrix} 0 & -\gamma_2 \\ -\gamma_2 & 0 \end{pmatrix}, \end{aligned} \tag{B.14}$$

where γ_1 and γ_2 are the two components of shear,

$$\begin{aligned}\gamma &\equiv \gamma_1 + i\gamma_2 = |\gamma| e^{2i\varphi}, \\ \gamma_1 &= \gamma\cos 2\varphi, \\ \gamma_2 &= \gamma\sin 2\varphi, \end{aligned} \tag{B.15}$$

where φ is the angle of the shape direction with respect to the θ_1-axis, and they are related to the second derivative of the lens potential as the convergence in equation (B.12):

$$\gamma_1 = \frac{1}{2}(\psi_{,11} - \psi_{,22}) \tag{B.16}$$

$$\gamma_2 = \psi_{,12}. \tag{B.17}$$

As shown in Figure B.3, the convergence κ describes the zooming and scaling, the γ_1 describes the plus mode and the γ_2 describes the cross mode in the reference frame.

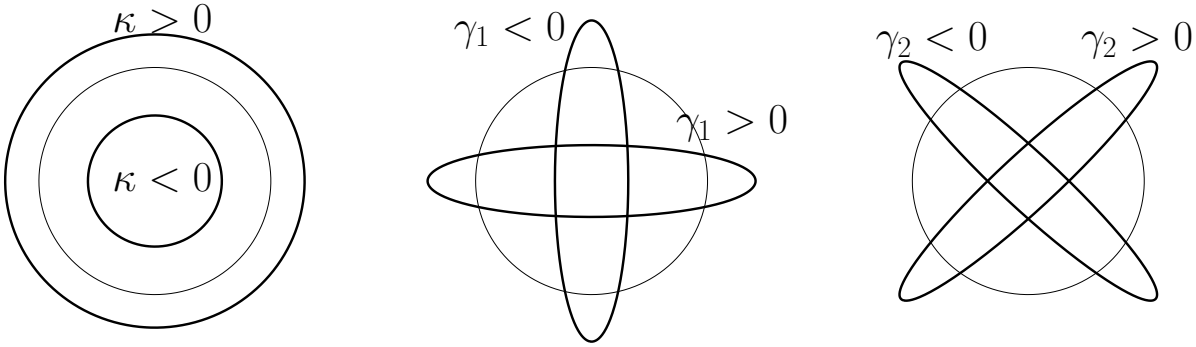

Figure B.3 The effects of convergence and shear on a circle. The convergence describes zooming and scaling. The γ_1 describes the plus mode, and the γ_2 describes the cross mode. The shear depends on the choice of the frame. Note that the distortion from shear is emphasized for the weak lensing.

The conservation of the surface brightness before and after the lensing is described as,

$$I(\vec{\theta}) = I^{(s)}[\vec{\beta}(\vec{\theta})], \tag{B.18}$$

where I and $I^{(s)}$ are the surface brightness of the observed image and the intrinsic source image before the lensing effect. In the weak lensing regime, the Jacobi matrix $\mathcal{A}$ is close to the unit matrix. Hence, the local linear approximation of equation (B.13) around the source position $\vec{\beta}_0$ and the corresponding image positions $\vec{\theta}_0$ gives,

$$\vec{\beta} - \vec{\beta}_0 \simeq \mathcal{A}(\vec{\theta}_0) \cdot (\vec{\theta} - \vec{\theta}_0). \tag{B.19}$$

From the eigenvalues of the equatoin (B.14), a major and minor axis after the lensing effect for a intrinsic small circle with a radius R are given as,

$$a \equiv \frac{R}{1-\kappa-|\gamma|} = \frac{R}{(1-\kappa)(1-|g|)}, \tag{B.20}$$

$$b \equiv \frac{R}{1-\kappa+|\gamma|} = \frac{R}{(1-\kappa)(1+|g|)}, \tag{B.21}$$

respectively. The reduced shear is defined by,

$$g(\vec{\theta}) = \frac{\gamma(\vec{\theta})}{1-\kappa(\vec{\theta})} = \frac{|\gamma|}{1-\kappa} e^{2i\varphi}. \tag{B.22}$$

The axis ratio is calculated as,

$$r = \frac{b}{a} = \frac{1-|g|}{1+|g|}. \tag{B.23}$$

From this equation, we can obtain the reduced shear from the measured shape after the lensing:

$$|g| = \frac{1-r}{1+r}. \tag{B.24}$$

Figure B.4 shows this configuration.

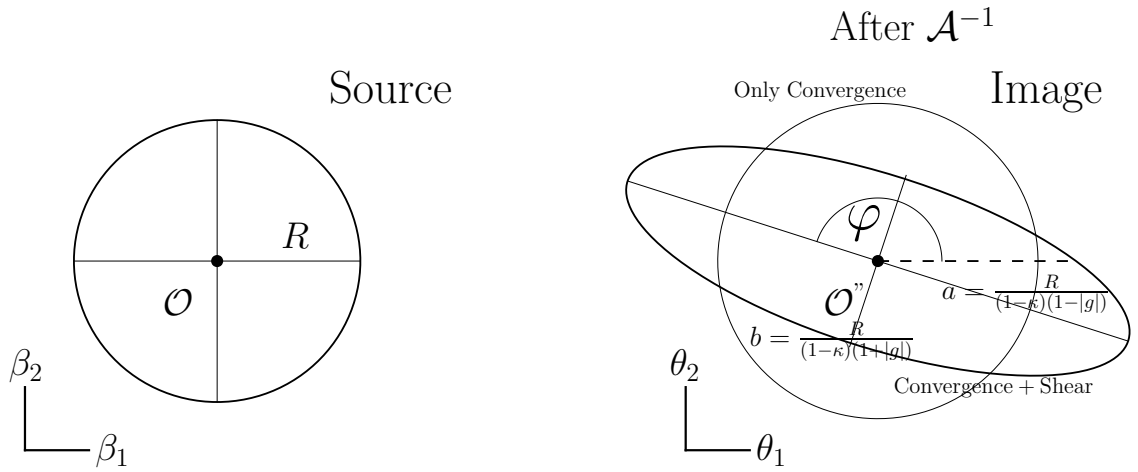

Figure B.4 The lensing mapping by lensing effects. A small circular source is mapped into an ellipse with axis ratio $r = (1-|g|)/(1+|g|)$. The direction of the ellipse is determined by the phase of $\gamma = |\gamma|e^{2i\varphi}$. In reality, the shape before lensing is not circle. Thus, what we observe on the sky is the sum of the intrinsic shape and the lensing effects on the source galaxies.

Hence, if all the galaxies have a round shape, we can measure the reduced shear from the measured

axis ratio after the lensing effects. However, obviously, source galaxies have their intrinsic shapes. Thus, in the weak lensing regime, the shape distortion is so weak that this effect cannot be observed by individual images. Hence, we need to average the shapes over a sample of background galaxies to reduce these intrinsic shape noises.

B.4 Estimator

The two definitions of the shape of elliptical isophotes are commonly used with the axis ratio $r = b/a$ and the major axis φ. The shear and distortion are respectively defined for elliptical isophotes:

$$\epsilon \equiv \frac{1-r}{1+r} e^{2i\varphi}, \tag{B.25}$$

$$\chi \equiv \frac{1-r^2}{1+r^2} e^{2i\varphi}. \tag{B.26}$$

The shear and distortion are related to each other:

$$\epsilon = \frac{\chi}{1+\sqrt{1-|\chi|^2}} \tag{B.27}$$

$$\chi = \frac{2\epsilon}{1+|\epsilon|^2}. \tag{B.28}$$

With equation (B.19), the shear and ellipticity are converted from the intrinsic ones ($\epsilon^{(s)}$, $\chi^{(s)}$) by the lensing effects to the observed ones (ϵ, χ),

$$\epsilon = \frac{\epsilon^{(s)} + g}{1 + g^* \epsilon^{(s)}}, \tag{B.29}$$

$$\chi = \frac{\chi^{(s)} + 2g + g^2 \chi^{(s)*}}{1 + |g|^2 + 2\mathcal{R}e(g\chi^{(s)*})}, \tag{B.30}$$

where $*$ denotes the complex conjugation. Since, the source galaxies have the intrinsic shapes (i.e., $\epsilon^{(s)} \neq 0$), the observed shape contains the shape noise in addition to the reduced lensing shear g.

For the general brightness profile $I(\vec{\theta})$, the center is defined by,

$$\bar{\theta} = \frac{\int \mathrm{d}^2\theta \; q_I[I(\vec{\theta})] I(\vec{\theta}) \vec{\theta}}{\int \mathrm{d}^2\theta \; q_I[I(\vec{\theta})] I(\vec{\theta})}, \tag{B.31}$$

where $q_I(I)$ is the weight function. The second-order brightness moments are defined as,

$$Q_{ij} = \frac{\int \mathrm{d}^2\theta \; q_I[I(\vec{\theta})] I(\vec{\theta}) (\theta_i - \bar{\theta}_i)(\theta_j - \bar{\theta}_j)}{\int \mathrm{d}^2\theta \; q_I[I(\vec{\theta})] I(\vec{\theta})}. \tag{B.32}$$

For circle image, $Q_{11} = Q_{22}$, $Q_{12} = 0$. The size is described by tr$Q$. Using the second-order brightness

moments, the definition of shear and ellipticity are generalized as,

$$\chi = \frac{Q_{11} - Q_{22} + 2iQ_{12}}{Q_{11} + Q_{22}}, \tag{B.33}$$

$$\epsilon = \frac{Q_{11} - Q_{22} + 2iQ_{12}}{Q_{11} + Q_{22} + 2\sqrt{Q_{11}Q_{22} - Q_{12}^2}}. \tag{B.34}$$

The $Q_{ij}^{(s)}$, $\chi^{(s)}$ and $\epsilon^{(s)}$ for the intrinsic shapes are defined in the same way:

$$Q_{ij}^{(s)} = \frac{\int \mathrm{d}^2\beta \; q_I[I^{(s)}(\vec{\beta})]I^{(s)}(\vec{\theta})(\beta_i - \bar{\beta}_i)(\beta_j - \bar{\beta}_j)}{\int \mathrm{d}^2\beta \; q_I[I^{(s)}(\vec{\beta})]I^{(s)}(\vec{\theta})}. \tag{B.35}$$

From $\mathrm{d}^2\beta = \det\mathcal{A} \; \mathrm{d}^2\theta$, $\beta_i - \bar{\beta}_i = \mathcal{A}_{im}(\theta_m - \bar{\theta}_m)$ and $\mathcal{A} \equiv \mathcal{A}(\bar{\theta})$, the relation before and after the lensing is derived at the first order as,

$$Q^{(s)} = \mathcal{A}Q\mathcal{A}^T = \mathcal{A}Q\mathcal{A}, \tag{B.36}$$

which also is the generalization of equation (B.29).

We assume the intrinsic orientation of the sources is random, thus the expectation value of the shape vanish:

$$\mathrm{E}(\chi^{(s)}) = \mathrm{E}(\epsilon^{(s)}) = 0. \tag{B.37}$$

Hence, the expectation values of equation (B.29) give us:

$$\hat{g} = \mathrm{E}(\epsilon), \tag{B.38}$$

which is the unbias estimator of the reduced lensing shear. On the other hand, the definition of χ is not the unbias estimator of the reduced lensing shear. We need to correct by the lensing responsivity as we do for Chapter 2, since the definition of the HSC lensing shear catalog is based on this.

B.5 Tangential shear with respect to galaxy clusters

The γ_1, γ_2 depend on the reference coordinate systems. When there is the lens object, the shear is orientated tangent to the radius vector from the center of the lens. The tangential and cross components are defined by the a direction ϕ with respect to the lens positions:

$$\gamma_+ = -\mathcal{R}e[\gamma e^{-2i\phi}] = -\gamma_1 \cos 2\phi - \gamma_2 \sin 2\phi, \tag{B.39}$$

$$\gamma_\times = -\mathcal{I}m[\gamma e^{-2i\phi}] = \gamma_1 \sin 2\phi - \gamma_2 \cos 2\phi. \tag{B.40}$$

Figure B.5 shows the example of the coordinate transformation around the lens system. Since the gravitational lensing comes from the scalar perturbation, at the first order the gravitational lensing effects exist only in the tangential shear. The cross components are used to check the residual systematics errors.

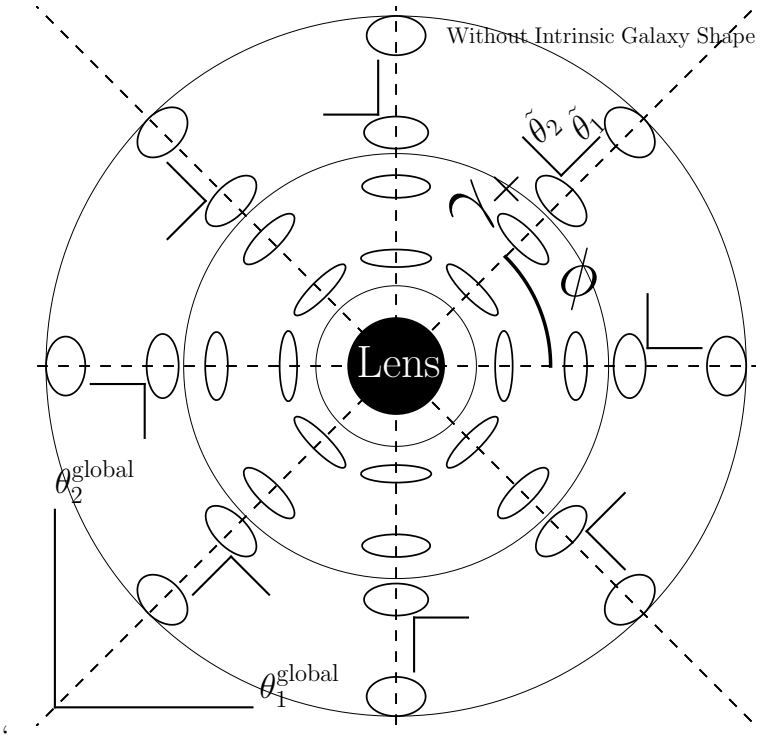

Figure B.5 The lens system and the gravitational lensing effects on the circles. Thus, we ignore the intrinsic galaxy shape noise on this figure. To get the tangential shear, we need to rotate the coordinate systems as equation (B.39) from the global coordinate system. After measuring the tangential shear, we can get the information on the mass distribution through equation (B.47).

For the general mass distribution, we can derive the relation between the mean tangential shear on circles and the convergence as follows. We use Gauss's theorem:

$$\int_0^\theta \mathrm{d}^2\vartheta\ \nabla\cdot\nabla\psi = \theta \oint \mathrm{d}\varphi\ \nabla\psi\cdot\vec{n}, \tag{B.41}$$

where ψ is an arbitrary scalar function and $\vec{n}$ is the outward directed normal vector on the integration circle. We can take ψ to be the deflection potential in equation (B.11). From equation (B.12), we obtain:

$$m(\theta) \equiv \frac{1}{\pi}\int_0^\theta \mathrm{d}^2\vartheta\ \kappa(\vec{\vartheta}) = \frac{\theta}{2\pi}\oint \mathrm{d}\varphi\ \frac{\partial\psi}{\partial\theta}, \tag{B.42}$$

where we use $\nabla\psi\cdot\vec{n} = \psi_{,\theta}$. By differentiating this equation with respect to θ gives,

$$\frac{\mathrm{d}m}{\mathrm{d}\theta} = \frac{m}{\theta} + \frac{\theta}{2\pi}\oint \mathrm{d}\varphi\ \frac{\partial^2\psi}{\partial\theta^2}. \tag{B.43}$$

When we consider the point on the θ_1 axis ($\phi = 0$), $\psi_{,\theta\theta} = \psi_{11} = \kappa + \gamma_1 = \kappa - \gamma_+$. This expression is independent of the reference coordinates. Thus, this relation is valid for all φ in the integrated. Hence, equation (B.43) gives the relation on the mean of the convergence and tangential shear:

$$\frac{\mathrm{d}m}{\mathrm{d}\theta} = \frac{m}{\theta} + \theta\left[\langle\kappa(\theta)\rangle - \langle\gamma_+\rangle\right]. \tag{B.44}$$

On the other hand, equaton (B.42) denotes that,

$$
\begin{aligned}
m(\theta) &= \theta^2\bar{\kappa}(\theta) \equiv 2\int_0^\theta \mathrm{d}\vartheta\ \vartheta\langle\kappa(\vartheta)\rangle, \\
\frac{\mathrm{d}m}{\mathrm{d}\theta} &= 2\theta\langle\kappa(\theta)\rangle. \qquad \text{(B.45)} \\
& \qquad \text{(B.46)}
\end{aligned}
$$

Thus, equation (B.44) gives,

$$
\begin{aligned}
2\theta\langle\kappa(\theta)\rangle &= \theta\bar{\kappa}(\theta) + \theta\left[\langle\kappa(\theta)\rangle - \langle\gamma_+\rangle\right], \\
\langle\gamma_+(\theta)\rangle &= \bar{\kappa}(\theta) - \langle\kappa(\theta)\rangle. \qquad \text{(B.47)}
\end{aligned}
$$

Thus, from the measurements of the average of the tangential shear in a circle, we can measure the convergence values, which is related to the mass profile of lenses, even if the density is not axi-symmetric.

B.6 Stacked cluster-galaxy lensing

It is difficult to measure the tangential shear around a cluster with a high signal-to-noise ratio. Thus, we need to average over a sample of clusters to increase the signal-to-noise ratio. For example, if we are interested in the mass profile in a richness bin, we stack the clusters in the richness bin. This cross-correlation between the positions of cluster and source galaxies is called stacked cluster-galaxy lensing.

By averaging over the shear measurements around the clusters can probe their average of (projected) mass profile:

$$
\begin{aligned}
\langle\Delta\Sigma(R)\rangle &\equiv \Sigma_{\mathrm{cr}}[\bar{\kappa}(R/D_{\mathrm{d}}) - \langle\kappa\rangle(R/D_{\mathrm{d}})] \\
&= \bar{\Sigma}(R) - \langle\Sigma\rangle(R). \qquad \text{(B.48)}
\end{aligned}
$$

If the selection is unbias in terms of the cluster direction, we can assume the three-dimensional spherical symmetry: $\rho(\vec{r}) = \rho(r)$. In this case, the tangential shear is related to this three-dimensional density profile in the thin lens approximation thorough,

$$
\begin{aligned}
\langle\Sigma(R)\rangle &= 2\int_0^\infty \mathrm{d}z\ \rho(r = \sqrt{R^2 + z^2}), \qquad \text{(B.49)} \\
\bar{\Sigma}(R) &= \frac{2}{R^2}\int_0^R R^{'}\mathrm{d}R^{'}\ \Sigma(R^{'}). \qquad \text{(B.50)}
\end{aligned}
$$

Using this assumption, we can reconstruct the mean of matter density around clusters by fitting with the assumed matter density profile. This relation between the matter density profile and weak lensing measurements is useful to constrain the mass-richness relation described in Chapter 2.

B.7 Possible systematic errors

Since the weak lensing effects are smaller than the intrinsic shape, we need to be careful about the systematics. In the presence of systematics, the relation between the shape measurements and the lensing shear becomes more complicated in reality.

B.7.1 Point-spread function

One of the main systematics is PSF. It describes the smearing of the image by the sky and telescope optics, and it changes the observed image profile by a convolution with the PSF function as

$$I^{\rm obs}(\vec{\theta}) = \int {\rm d}^2\vartheta \; I(\vec{\vartheta})P(\vec{\theta}-\vec{\vartheta}). \tag{B.51}$$

The typical size of PSF of the ground-based telescope is larger than faint galaxies. This increases the size of the observed image and makes the image rounder than the true image with the lensing effects. In addition, the PSF is not always circular, thus the observed image can be distorted by its anisotropies like the lensing shear. The PSF is estimated from the interpolation of the images of stars since their image should be circle if there are no PSF effects. In the HSC lensing shear catalog, the PSF effects are calibrated with image simulations assuming a galaxy sample detected in the Hubble Space Telescope with a smaller PSF effect (Mandelbaum et al., 2018a,c).

B.7.2 Redshift estimation

To calculate the projected mass density profile in equatoin (B.48), we need to calculate $\Sigma_{\rm cr}(z_l, z_s)$ in equation (B.9) from the estimated lens and source redshift. In the case of the cluster-galaxy lensing, the error of redshift estimation for the clusters is around 0.01 from the red-sequence technique. However, as the redshift of the lens system increases, the uncertainty of redshift for the available source galaxies increases due to $z_l < z_s$. Thus, we need to be careful about the redshift estimation to avoid significant biases in lensing measurements. Since it is generally difficult to earn spectroscopic redshift for such many and faint galaxies in surveys, we use redshift estimation based on photometries in several bands (e.g., *grizy*). Specifically, we use the HSC photometric redshift catalog for galaxies in the HSC lensing shear catalog in Chapter 2 derived from several codes and methods, which generally employs characteristic features in galaxies such as the 4000Å break, in Tanaka et al. (2018). These photometric redshifts are validated by a small sample of spectroscopic redshifts from other surveys to check the performance of the photometric redshifts in Tanaka et al. (2018).

B.7.3 Off-centering

As the redshift of the cluster increases, it becomes more difficult to estimate the center of the clusters from the optical data. With off-centering effects, the observed tangential profile is smeared at the inner radius. We marginalized over this off-centering effects on the lensing profiles in Chapter 2 when constraining the mass-richness relation from weak lensing effects by assuming the Gaussian distribution for the off-centering distribution from true centers of galaxy clusters.

B.7.4 Dilution effect

Near the center of the lens object, the foreground galaxies can be misidentified as the source galaxies from the error of the redshift. There is no lensing effect in the foreground galaxies. Hence, this dilution effect biases the normalization of the lensing measurements. In Chapter 2, we conservatively select source galaxies for our lensing measurements to mitigate these dilution effects by employing a probability distribution function of photometric redshift for each source galaxy.

Appendix C

N-body simulation-based halo emulator: Dark Emulator

Cosmological N-body simulations are one of the methods commonly used in the literature to model predictions of halo statistics. We use the database generated by the Dark Quest campaign (Nishimichi et al., 2019) to predict the halo mass function and the halo-matter cross-correlation[1], both of which are important ingredients for our model predictions in the mass-richness analysis in Chapter 2 for the abundance and the lensing profiles and the splashback feature analysis in Chapter 3 for the splashback radius locations. Nishimichi et al. (2019) developed a scheme called Dark Emulator to predict statistical quantities of halos, including the mass function and the halo-matter cross-correlation function as a function of halo mass, redshift, separation length, and cosmological parameters, based on a series of high-resolution, cosmological N-body simulations in the Dark Quest campaign (Nishimichi et al., 2019).

The simulation suite is composed of cosmological N-body simulations for 101 cosmological models within a flat wCDM framework. The simulations trace the nonlinear evolution of 2048^3 particles in a box size of 1 or $2h^{-1}$Gpc on a side with mass resolution of $\simeq 10^{10}h^{-1}M_\odot$ or $\simeq 8\times10^{10}h^{-1}M_\odot$, respectively. There are 21 redshift slices for each simulation realization across the range $0 \leq z \leq 1.47$. Nishimichi et al. (2019) employed Rockstar (Behroozi et al., 2013) to identify dark matter halos. The halo mass definition in the simulations includes all particles within a distance of $R_{200\mathrm{m}}$ from the halo center. The minimum halo mass of the emulator is $10^{12}h^{-1}M_\odot$. Note that we also use a halo catalog from one of these simulations to investigate projection effects on the observational constraints for the splashback features in Chapter **??**. Dark Emulator relies on data compression based on Principal Component (PC) Analysis followed by Gaussian Process Regression for each PC coefficient from a subset of 80 cosmological models. Nishimichi et al. (2019) used the other subsets as a validation set to assess the performance of the emulator. We note

[1]We define the halo-matter cross-correlation function $\xi^{\mathrm{3D}}_{\mathrm{hm}}(r;M,z)$ as $\rho(r;M,z) = \bar{\rho}_{\mathrm{m0}}[1+\xi^{\mathrm{3D}}_{\mathrm{hm}}(r;M,z)]$, where $\rho(r;M,z)$ is the average matter density profile around halos with mass M at redshift z and $\bar{\rho}_{\mathrm{m0}}$ is the present-day mean matter density. We note that we use the present-day mean matter density since we use the comoving coordinate for the radius and density in this thesis.

that Nishimichi et al. (2019) did not use the realizations for the *Planck* cosmology in the regression.

Appendix D

Covariance for abundance and lensing measurements

We describe the covariance for the mass-richness relation in Chapter 2 as follows. We use analytic calculations of the sampling variance contribution to the covariances, assuming that the distribution of clusters and lensing fields obeys the Gaussian statistics. We describe the analytic model and the detailed estimation procedure in Appendix D.1, and validate it against realistic shear and cluster mock catalogs in Appendix D.2. We also use an analytic model for Poisson shot noise in the abundance covariance. On the other hand, we do not use an analytic model for the shape noise covariance in the lensing profiles, but rather estimate it directly from the data catalogs as described below.

D.1 Analytic model of the covariance matrix

We employ an analytic covariance model for cluster abundances (Hu & Kravtsov, 2003; Takada & Bridle, 2007; Oguri & Takada, 2011) as

$$\mathbf{C}[N_{\alpha,\beta}, N_{\alpha',\beta'}] = N_{\alpha,\beta}\delta^K_{\alpha\alpha'}\delta^K_{\beta\beta'} + S_{\beta,\alpha\alpha'}\delta^K_{\beta\beta'}, \tag{D.1}$$

where $\delta^K_{\alpha\alpha'}$ denotes the Kronecker delta function. The first term denotes the Poisson shot noise from the finite number of available clusters and the second term gives the sample covariance as

$$S_{\beta,\alpha\alpha'} = N_{\alpha,\beta}N_{\alpha',\beta}\int_{z_{\beta,\min}}^{z_{\beta,\max}}\frac{\mathrm{d}z}{H(z)}W^{\rm h}_{\alpha,\beta}(z)W^{\rm h}_{\alpha',\beta}(z)\chi^{-2}(z)\int\frac{\ell\mathrm{d}\ell}{2\pi}\left|\tilde{W}_s(\ell\Theta_s)\right|^2 P^{\rm L}_{\rm mm}\left(k=\frac{\ell}{\chi};z\right), \tag{D.2}$$

where $\tilde{W}_s(\ell\Theta_s)$ is the Fourier transform of the survey window function, for which we assume a circular survey geometry with survey area $\Omega_{\rm tot} = \pi\Theta_s^2$ for simplicity: $\tilde{W}_s(\ell\Theta_s) = 2J_1(\ell\Theta_s)/(\ell\Theta_s)$. We use CAMB (Lewis et al., 2000) for computing the linear matter power spectrum $P^{\rm L}_{\rm mm}(k;z)$. The halo weight function

is defined as

$$W^{\rm h}_{\alpha,\beta}(z) = \frac{\Omega_{\rm tot}}{N_{\alpha,\beta}}\chi^2(z)\int {\rm d}M \frac{{\rm d}n}{{\rm d}M} S(M,z|N_{\alpha,\rm min},N_{\alpha,\rm max}) b_{\rm h}(M;z). \tag{D.3}$$

Here $b_{\rm h}(M;z)$ is the bias parameter for halos with mass M at redshift z, for which we employ a halo bias function presented in Tinker et al. (2010) calculated using the *colossus* package (Diemer, 2018).

We calculate the covariance model for the stacked lensing profiles among different redshift, richness, and radial bins by decomposing it into the shape noise covariance $\mathbf{C}^{\rm SN}$ and the sample covariance $\mathbf{C}^{\rm SV}$ as

$$\mathbf{C} = \mathbf{C}^{\rm SN} + \mathbf{C}^{\rm SV}, \tag{D.4}$$

where we compute the shape noise covariance by randomly rotating background galaxies (e.g., Murata et al., 2018). More specifically, we measure the lensing estimators around the clusters in the data catalog with all the multiplicative biases after randomly rotating background shapes in the HSC data catalog, repeating the process 15,000 times. We then calculate the covariance among different richness, redshift, and radial bins based on these measurements.

For the sample covariance of the lensing profiles, we use a Gaussian covariance (Oguri & Takada, 2011; Shirasaki & Takada, 2018) as

$$\begin{aligned}
&\mathbf{C}^{\rm SV}[\Delta\Sigma_{\alpha,\beta}(R_m),\Delta\Sigma_{\alpha',\beta'}(R_n)] \\
=\ & \frac{1}{\Omega_{\rm lens}\langle\chi_{l,\beta}\rangle\langle\chi_{l,\beta'}\rangle}\int\frac{k{\rm d}k}{2\pi}\left[C^{mn}_{\kappa\kappa,\alpha\alpha'\beta}(k)C^{\rm obs}_{\rm hh,\alpha\alpha'\beta}(k)\delta^K_{\beta\beta'} + C_{\Delta\Sigma,\alpha\beta}(k)C_{\Delta\Sigma,\alpha'\beta'}(k)\right]\widehat{J}_2(kR_m)\widehat{J}_2(kR_n),
\end{aligned} \tag{D.5}$$

where the power spectrum of convergence fields with $\langle\Sigma_{\rm cr}\rangle_{ls}$ terms are defined as

$$C^{mn}_{\kappa\kappa,\alpha\alpha'\beta}(k) = \langle\Sigma_{\rm cr}\rangle_{ls,\alpha\beta}(R_m)\langle\Sigma_{\rm cr}\rangle_{ls,\alpha'\beta}(R_n)\int\frac{{\rm d}z}{H(z)}\left(\bar{\rho}_{\rm m0}\Sigma^{-1}_{\rm cr}(z,z_{s,\beta})\frac{\langle\chi_{l,\beta}\rangle}{\chi(z)}\right)^2 P_{\rm mm}\left(k'=\frac{\langle\chi_{l,\beta}\rangle}{\chi(z)}k,z\right), \tag{D.6}$$

and $\langle\chi_{l,\beta}\rangle$ is the average of $\chi(z)$ in β-th cluster redshift bin from the data with $N\geq 15$. Here $z_{s,\beta}$ is the weighted mean of $z_{s,\rm best}$ ($z_{\rm best}$ for a source galaxy, s) in β-th cluster redshift bin over all the radial bins as

$$z_{s,\beta} = \frac{\sum\limits_{l,s;z_l\in z_\beta} z_{s,\rm best}w_{ls}}{\sum\limits_{l,s;z_l\in z_\beta} w_{ls}}. \tag{D.7}$$

We find $z_{s,1}=1.09$, $z_{s,2}=1.30$, and $z_{s,3}=1.57$ for the fiducial photo-z catalog and source selection cut

with the *Planck* cosmological parameters. The weighted mean critical surface mass density is calculated as

$$\langle\Sigma_{\rm cr}\rangle_{ls,\alpha\beta}\left(R\right)=\frac{\sum\limits_{l,s;N_l\in N_\alpha,z_l\in z_\beta}\left\langle\Sigma_{\rm cr}^{-1}\right\rangle_{ls}^{-1}w_{ls}\Big|_{R=\chi_l|\boldsymbol{\theta}_l-\boldsymbol{\theta}_s|}}{\sum\limits_{l,s;N_l\in N_\alpha,z_l\in z_\beta}w_{ls}\Big|_{R=\chi_l|\boldsymbol{\theta}_l-\boldsymbol{\theta}_s|}}. \tag{D.8}$$

We use HALOFIT (Smith et al., 2003) for the nonlinear matter power spectrum based on Takahashi et al. (2012). The terms $C^{\rm obs}_{{\rm hh},\alpha\alpha'\beta}$ and $C_{\Delta\Sigma,\alpha\beta}$ are defined as

$$C^{\rm obs}_{{\rm hh},\alpha\alpha'\beta}(k)=C_{{\rm hh},\alpha\alpha'\beta}(k)+\frac{\langle\chi_{l,\beta}\rangle^2\Omega_{\rm tot}}{N_{\alpha,\beta}}\delta^K_{\alpha\alpha'}, \tag{D.9}$$

with

$$C_{{\rm hh},\alpha\alpha'\beta}(k)=\int_{z_{\beta,\rm min}}^{z_{\beta,\rm max}}\frac{{\rm d}z}{H(z)}W^{\rm h}_{\alpha,\beta}(z)W^{\rm h}_{\alpha',\beta}(z)P^{\rm L}_{\rm mm}(k;z), \tag{D.10}$$

and

$$C_{\Delta\Sigma,\alpha\beta}(k)=\frac{\Omega_{\rm tot}}{N_{\alpha,\beta}}\bar{\rho}_{\rm m0}\int_{z_{\beta,\rm min}}^{z_{\beta,\rm max}}\frac{{\rm d}z}{H(z)}\,\chi^2(z)\int{\rm d}M\frac{{\rm d}n}{{\rm d}M}S(M,z|N_{\alpha,\rm min},N_{\alpha,\rm max})P_{\rm hm}(k;M,z). \tag{D.11}$$

The second-order Bessel function after averaging within radial bins is given as

$$\widehat{J}_2(kR_n)=\frac{2}{R^2_{n,\rm max}-R^2_{n,\rm min}}\int_{R_{n,\rm min}}^{R_{n,\rm max}}{\rm d}R\;R\;J_2(kR). \tag{D.12}$$

We do not account for the window function effect of the cluster and shear catalogs in this analytic model. In Appendix D.2, we validate this analytical covariance by using realistic mock shear and cluster catalogs. We also ignore the cross-covariance between the stacked lensing profiles and abundance measurements since this cross-covariance does not have a large impact in the parameter estimation, which we confirm by using the cross-covariance estimated from the mock catalogs. Specifically, we repeat the MCMC analysis based on the fiducial covariance with the cross-covariance from the mock catalogs derived in Appendix D.2 to find that the 68% percentile widths are consistent with the fiducial ones and the shift of the $\chi^2_{\rm min}$ value from the fiducial value is ~ 0.1.

In the parameter estimation, we fix the richness-mass relation parameters for the analytic covariance model to reduce the model calculation time (especially of the lensing covariance). For each setup of the photo-z catalog, source selection cut, and the cosmological parameters, we estimate the analytic covariance model as follows. First, we perform the MCMC analysis with a simpler covariance model which does not include the richness-mass relation dependent terms of $C_{\Delta\Sigma,\alpha\beta}(k)C_{\Delta\Sigma,\alpha'\beta'}(k)$ in equation (D.5) and $C_{{\rm hh},\alpha\alpha'\beta}(k)$ in equation (D.9). We do not fix the richness-mass relation parameters for other terms in the abundance and lensing profiles. We obtain the best-fit parameters as $\{A,B,B_z,C_z,\sigma_0,q,q_z,p_z\}=$

$\{3.16, 0.92, -0.13, 4.17, 0.29, -0.12, -0.02, 0.52\}$ for the *Planck* model, and $\{A, B, B_z, C_z, \sigma_0, q, q_z, p_z\} = \{3.37, 0.84, -0.14, 4.47, 0.17, -0.02, 0.19, 0.50\}$ for the *WMAP* model with the fiducial photo-z catalog (`MLZ`) and source selection cut (*Pcut* with $\Delta z = 0.1$). Second, we calculate the covariance with the analytic model based on these parameters from the simpler covariance to derive the parameter constraints. For the case of the fiducial photo-z catalog and source selection cut, the richness-mass relation parameters for the covariance calculation above are consistent with our final results shown in Table 2.2, and the $\chi^2_{\rm min}$ values are not very different from the final values shown in Table 2.2. We show our covariance matrix for the fiducial setup with the *Planck* cosmological parameters in Figures 2.1 and 2.2.

D.2 Validation against realistic mock shear and cluster catalogs

We validate our model of the covariance matrix presented in Appendix D.1 against the realistic HSC shear and halo catalogs (Shirasaki et al., 2019, see Chapter 2.4.5 for more details). We use 2268 realizations of the mock catalogs that share the same footprints of the shear and halo catalogs as the *real* data catalogs. The cosmological parameters for the mock catalogs are the same as those for *WMAP* used in this thesis. We assign richness values for halos with $M \geq 10^{12} h^{-1} M_\odot$ to create the mock catalogs of the CAMIRA clusters with the richness values. The richness values are assigned according to the richness-mass relation parameters consistent with our results shown in Table 2.2 for the *WMAP* model as $\{A, B, B_z, C_z, \sigma_0, q, q_z, p_z\} = \{3.37, 0.85, -0.14, 4.47, 0.18, -0.05, 0.19, 0.50\}$. We repeat the measurements of the abundance and lensing profiles for each realization to calculate the covariance matrix from the 2268 realizations. Here we measure the lensing profiles from the shear values without shape noise as we use the shape noise covariance estimated in Appendix D.1. We also calculate the covariance contribution $\mathbf{C}^{\rm R}$ from the random subtraction (Singh et al., 2017). As shown in Section 2.3 of Singh et al. (2017), we subtract $\mathbf{C}^{\rm R}$ from the covariance above to account for the random subtraction. Murata et al. (2018) found that this term is negligible ($\mathbf{C}^{\rm R}/\mathbf{C} \sim 0.01$ for the diagonal terms) for the SDSS redMaPPer clusters. Similarly, we find that these values for the HSC CAMIRA clusters are similar to those for the SDSS redMaPPer clusters and thus are negligible for the HSC CAMIRA clusters.

In Figure D.1, we show the comparison between the covariance estimated from mock catalogs and the covariance with the analytic model for the *WMAP* model using the same richness-mass relation parameters. Since the resolution of the lensing shear in the mock catalogs is limited to 0.43 arcmin, we compare the lensing covariance only above an effective resolution limit for each cluster redshift bin. Here we set the resolution limit by comparing the mean of the lensing profiles from the mock catalogs with the model prediction (see Chapter 2.4.3). The figure shows that the diagonal components of the covariance with the analytic model agree well with those from the mock catalogs at better than the $\sim$10% level for both the abundance and lensing profiles measurements. We use the covariance with the analytic model for our parameter estimation because the covariance matrix from the mock catalogs is affected by the resolution

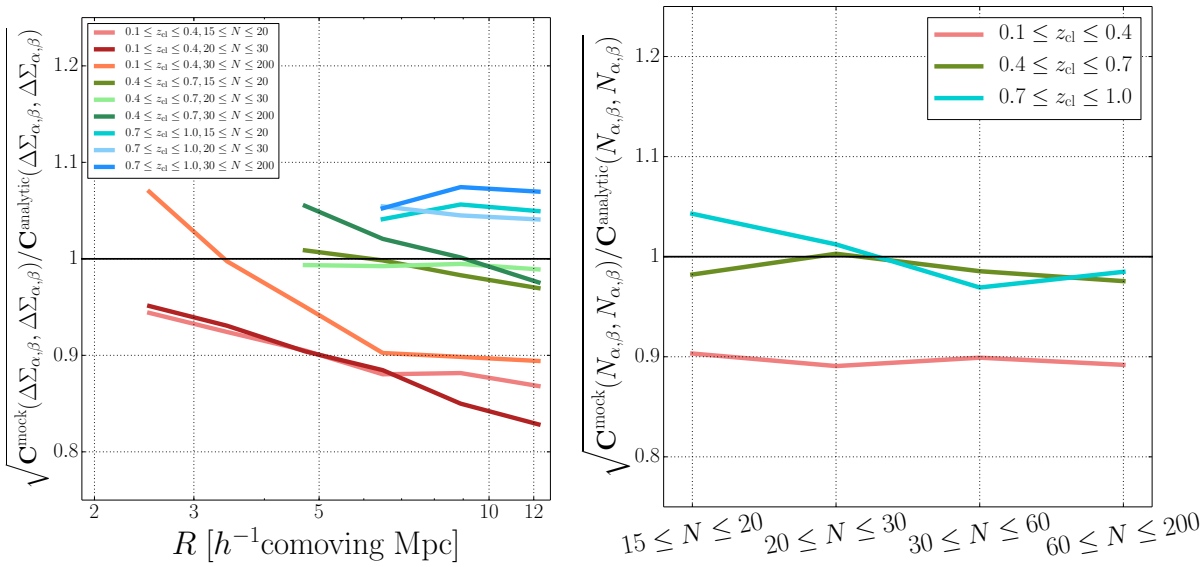

Figure D.1 The comparison of diagonal components between the covariance estimated from the mock catalogs and from the analytic model presented in Appendix D.1 for the *WMAP* cosmological parameters. Here we use the richness-mass relation parameters of $\{A, B, B_z, C_z, \sigma_0, q, q_z, p_z\} = \{3.37, 0.85, -0.14, 4.47, 0.18, -0.05, 0.19, 0.50\}$, which are consistent with our fiducial result for the *WMAP* cosmological parameters shown in Table 2.2. The left panel shows the comparison of the lensing covariance for each redshift and richness bin. We only show the result on the radial scales that are larger than the resolution limits in the mock catalog for each redshift bin. We include the shape noise covariance estimated from randomly rotating galaxy shapes in the data catalog for both covariances. The right panel shows the comparison of the abundance covariances in each redshift bin. The diagonal parts of the analytic covariances match the mock covariance to better than $\sim$10%.

effect as mentioned above.

Appendix E

Sanity check of the mass-richness relation

As a sanity check, in Figure E.1, we compare cluster masses of our mass-richness relation with those obtained from another independent study for the same clusters on the sky in our HSC observation footprint. Here we use the existing independent mass measurements from the Sunyaev–Zel'dovich (SZ) effect for some HSC CAMIRA clusters, as summarized in table 1 of Miyatake et al. (2019) with richness values. We employ eight massive clusters listed in table 1 of Miyatake et al. (2019) for this sanity check. Note that the number of SZ selected clusters are generally smaller than optically selected clusters at present for a given survey region. In Figure E.1, we confirm that our results of the mass-richness are reasonably consistent with the SZ masses described in Miyatake et al. (2019), given the well-known bias in SZ masses ($M_{\rm SZ}$) compared to weak lensing masses ($M_{\rm WL}$) as $1-b = M_{\rm SZ}/M_{\rm WL} \simeq 0.7$, which is summarized in figure 8 of Miyatake et al. (2019).

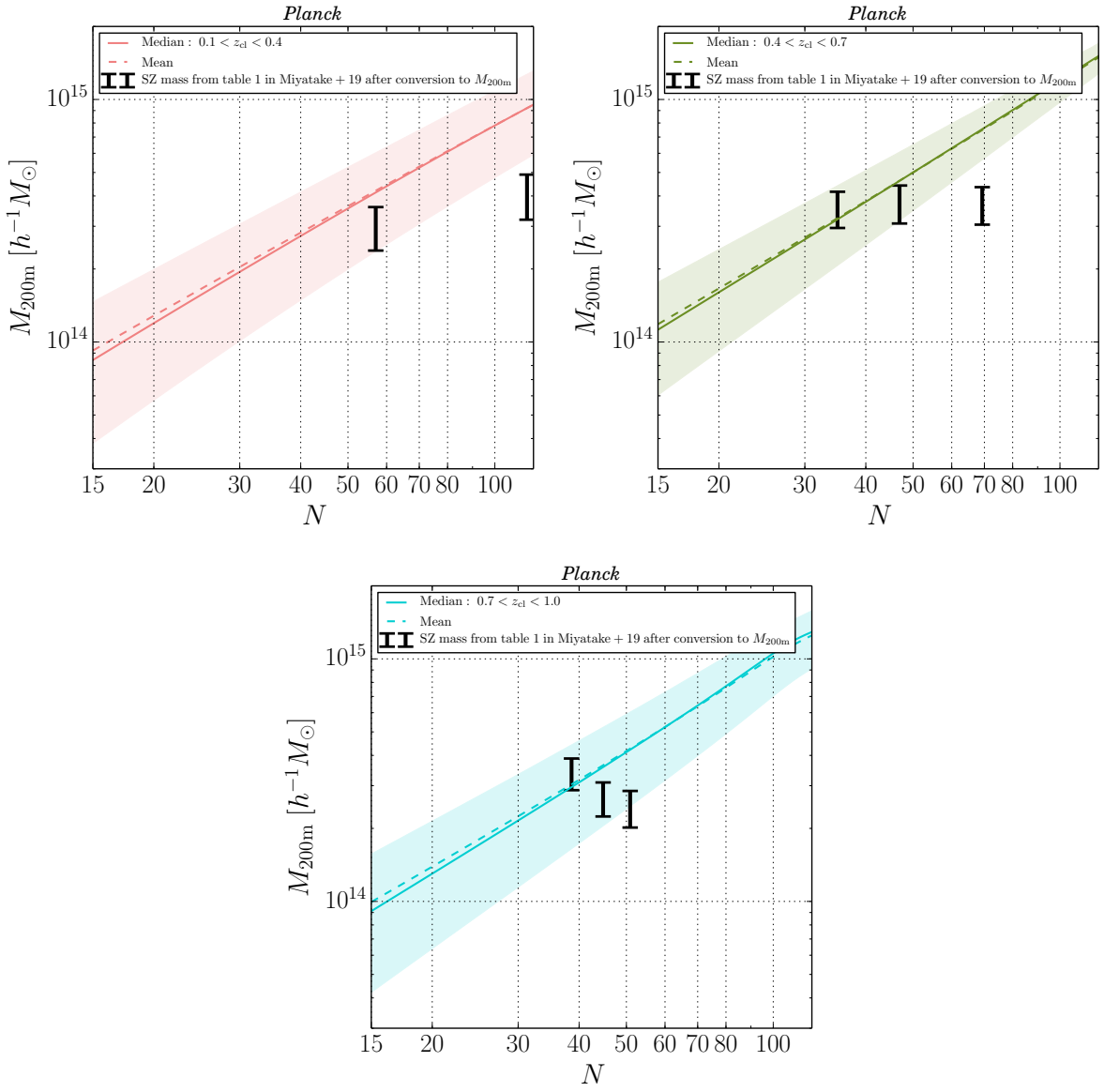

Figure E.1 A sanity check of our mass-richness relation at the best-fit richness-mass relation parameters and the *Planck* cosmology for each redshift range from Figure 2.6. We converted the SZ masses in Miyatake et al. (2019) into our mass convention of $M_{\rm 200m}$ based on the standard module of the *colossus* (Diemer, 2017).

Appendix F

Model parameter constraint contours

For references, we show model parameter constraint contours as follows.

F.1 Mass-richness relation

We show the model parameter constraint contours in Figure F.1 from the fiducial analysis of the mass-richness relation in Chapter 2, to show the marginalized one-dimensional posterior distributions for each parameter and the 68% and 95% credible levels contours for each two-parameter subspace from the MCMC chains.

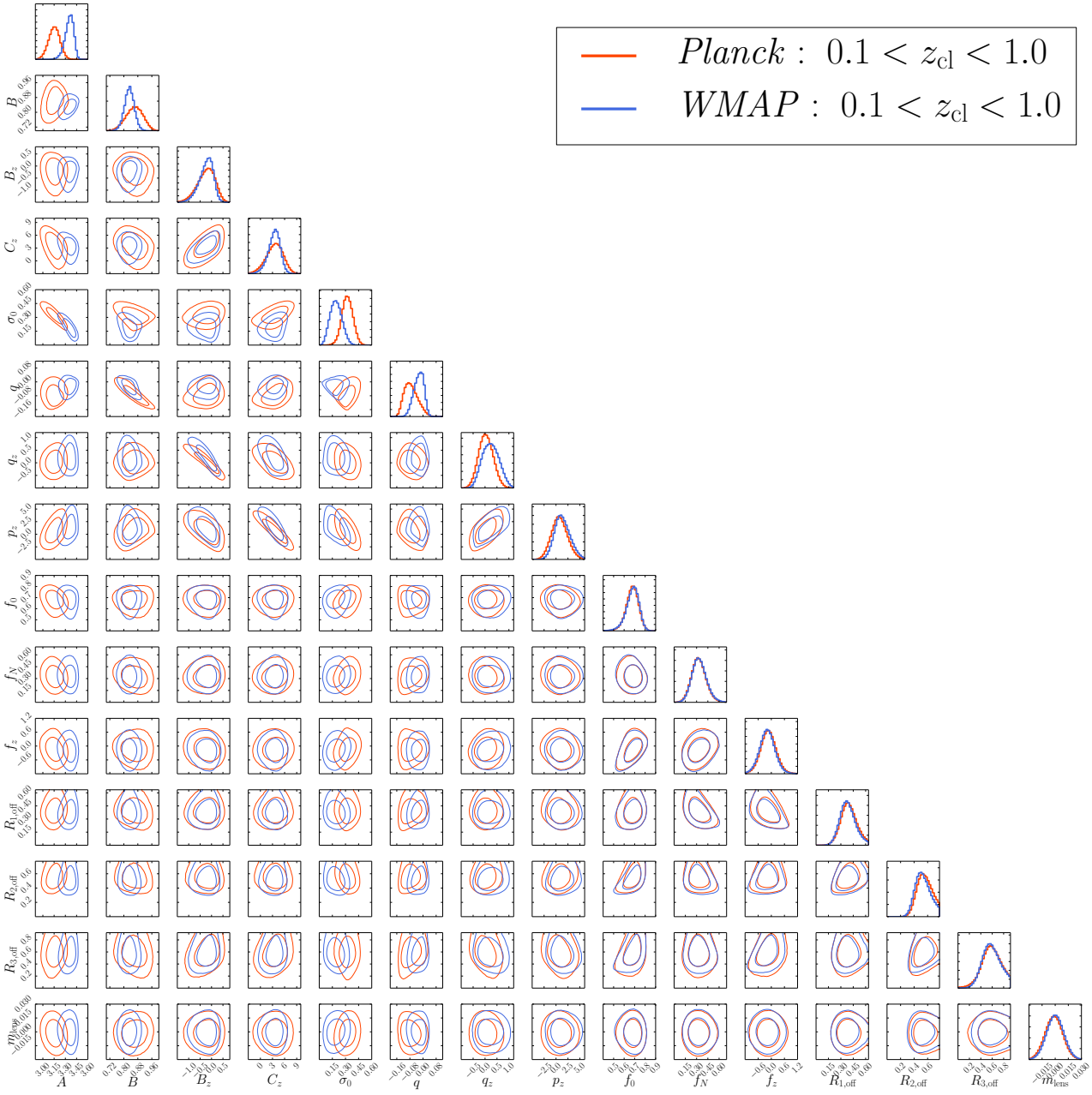

Figure F.1 The model parameter constraints in the fiducial analysis of the mass-richness relation in Chapter 2 for both the *Planck* and *WMAP* cosmological parameters. Diagonal panels show the posterior distributions of the model parameters, and the other panels show the 68% and 95% credible levels contours in each two-parameter subspace from the MCMC chains.

Bibliography

Abbott, T. M. C., et al. 2018, Phys. Rev. D, 98, 43526

Adhikari, S., Dalal, N., & Chamberlain, R. 2014, Journal of Cosmology and Astroparticle Physics, 11, 019

Adhikari, S., Dalal, N., & Clampitt, J. 2016, Journal of Cosmology and Astroparticle Physics, 7, 022

Adhikari, S., Sakstein, J., Jain, B., Dalal, N., & Li, B. 2018, Journal of Cosmology and Astroparticle Physics, 11, 033

Adhikari, S., Dalal, N., More, S., & Wetzel, A. 2019, ApJ, 878, 9

Aihara, H., et al. 2018a, PASJ, 70, S4

Aihara, H., et al. 2018b, PASJ, 70, S8

Aihara, H., et al. 2019, PASJ, arXiv:1905.12221

Allen, S. W., Evrard, A. E., & Mantz, A. B. 2011, ARA&A, 49, 409

Balogh, M. L., Morris, S. L., Yee, H. K. C., Carlberg, R. G., & Ellingson, E. 1997, ApJL, 488, 75

Banerjee, A., Adhikari, S., Dalal, N., More, S., & Kravtsov, A. 2019, arXiv:1906.12026

Bartelmann, M., & Schneider, P. 2001, Phys. Rep., 340, 291

Battaglia, N., et al. 2016, Journal of Cosmology and Astroparticle Physics, 8, 013

Baxter, E. J., Rozo, E., Jain, B., Rykoff, E., & Wechsler, R. H. 2016, MNRAS, 463, 205

Baxter, E., et al. 2017, ApJ, 841, 18

Behroozi, P. S., Wechsler, R. H., & Wu, H.-Y. 2013, ApJ, 762, 109

Bernstein, G. M., & Jarvis, M. 2002, AJ, 123, 583

Bertschinger, E. 1985, ApJS, 58, 39

Bosch, J., et al. 2018, PASJ, 70, S5

Bruzual, G. & Charlot, S. 2003, MNRAS, 344, 1000

Busch, P. & White, S. D. M. 2017, MNRAS, 470, 4767

Chandrasekhar, S. 1943, ApJ, 97, 255

Chang, C., et al. 2018, ApJ, 864, 83

Cohn, J. D., Evrard, A. E., White, M., Croton, D., & Ellingson, E. 2007, MNRAS, 382, 1738

Contigiani, O., Hoekstra, H., & Bahé, Y. M. 2019, MNRAS, 485, 408

Contigiani, O., Vardanyan, V., & Silvestri, A. 2019, Phys. Rev. D, 99, 4030

Cooray, A. & Sheth, R. 2002, Phys. Rep., 372, 1

Costanzi, M., et al. 2018, arXiv:1810.09456

Costanzi, M., et al. 2019, MNRAS, 482, 490

Dark Energy Survey Collaboration, et al. 2016, MNRAS, 460, 1270

de Jong, J. T. A., et al. 2013, The Messenger, 154, 44

Del Popolo, A. & Le Delliou, M. 2017, Galaxies, 5, 17

Diemer, B. & Kravtsov, A. 2014, ApJ, 789, 1

Diemer, B. 2017, ApJS, 231, 5

Diemer, B., Mansfield, P., Kravtsov, A.,& More, S. 2017, ApJ, 843, 140

Diemer, B. 2018, ApJS, 239, 35

Dietrich, J. P., et al. 2014, MNRAS, 443, 1713

Dressler, A. 1980, ApJ, 236, 351

Dressler, A. & Gunn, J. E. 1983, ApJ, 270, 7

Efron, B. 1982, The Jackknife, the Bootstrap and other resampling plans, Philadelphia: Society for Industrial and Applied Mathematics (SIAM)

Eke, V. R., Cole, S., & Frenk, C. S. 1996, MNRAS, 282, 263

Fang, Y., et al. 2016, MNRAS, 463, 1907

Fillmore, J. A. & Goldreich, P. 1984, ApJ, 281, 1

Flaugher, B. 2005, International Journal of Modern Physics A, 20, 3121

Foreman-Mackey, D., Hogg, D. W., Lang, D. & Goodman, J. 2013, PASP, 125, 306

Furusawa, H., et al. 2018, PASJ, 70, S3

Freedman, W. L. 2017, Nature Astronomy, 1, 169

Gao, L., et al. 2008, MNRAS, 387, 536

Gladders, M. D. & Yee, H. K. C., 2000, AJ, 120, 2148

Goodman, J. & Weare, J. 2010, Communications in Applied Mathematics and Computational Science, 5, 65

Górski, K. M., Hivon, E., Banday, A. J., Wandelt, B. D., Hansen, F. K., Reinecke, M., & Bartelmann, M. 2005, ApJ, 622, 759

Gunn, J. E. & Gott, J. R. 1972, ApJ, 176, 1

Haiman, Z., Mohr, J. J., & Holder, G. P. 2001, ApJ, 553, 545

Hamabata, A., Oogi, T., Oguri, M., Nishimichi, T., & Nagashima, M. 2019, MNRAS, 488, 4117

Hamana, T. & Mellier, Y. 2001, MNRAS, 327, 169

Hamilton, A. J. S. 2000, MNRAS, 312, 257

Hashimoto, D., Nishizawa, A. J., Shirasaki, M., Macias, O., Horiuchi, S., Tashiro, H., & Oguri, M. 2019, MNRAS, 484, 5256

Hearin, A. P., et al. 2014, MNRAS, 444, 729

Hikage, C., Takada, M., & Spergel, D. N. 2012, MNRAS, 419, 3457

Hikage, C., Mandelbaum, R., Takada, M., & Spergel, D. N. 2013, MNRAS, 435, 2345

Hikage, C. & Oguri, M. 2016, MNRAS, 462, 1359

Hikage, C., et al. 2019, PASJ, 71, 2, 43

Hinshaw, G., et al. 2013, ApJS, 208, 19

Hirata, C. & Seljak, U. 2003, MNRAS, 343, 459

Hoekstra, H., Herbonnet, R., Muzzin, A., Babul, A., Mahdavi, A., Viola, M., & Cacciato, M. 2015, MNRAS, 449, 685

Hsieh, B. C. & Yee, H. K. C. 2014, ApJ, 792, 102

Hu, W. & Kravtsov, A. V. 2003, ApJ, 584, 702

Ilbert, O., et al. 2009, ApJ, 690, 1236

Ivezić, Ž., et al. 2008, arXiv:0805.2366

Jian, H.-Y., et al. 2018, PASJ, 70, S23

Jing, Y. P., Mo, H. J., & Börner, G. 1998, ApJ, 494, 1

Johnston, D. E., et al. 2007, arXiv:0709.1159

Kaiser, N., Squires, G., & Broadhurst, T., 1995, ApJ, 449, 460

Kawanomoto, S., Uraguchi, F., Komiyama, Y., et al. 2018, PASJ, 70, 66

Kilbinger, M. 2015, Reports on Progress in Physics, 78, 086901

Kitayama, T., & Suto, Y. 1997, ApJ, 490, 557

Komiyama, Y., et al. 2018, PASJ, 70, S2

Kravtsov, A. V., & Borgani, S. 2012, ARA&A, 50, 353

Kuijken, K., et al. 2015, MNRAS, 454, 3500

Laigle, C., et al. 2016, ApJS, 224, 24

Landy, S. & Szalay, A. 1993, ApJ, 412, 64

Larson, R. B., Tinsley, B. M., & Caldwell, C. N. 1980, ApJ, 237, 692

Laureijs, R., et al. 2011, arXiv:1110.3193

Leauthaud, A., et al. 2010, ApJ, 709, 97

Lewis, A., Challinor, A., & Lasenby, A. 2000, ApJ, 538, 473

Lima, M. & Hu, W. 2005, Phys. Rev. D, 72, 043006

Lin, Y.-T., Mohr, J. J. & Stanford, S. A. 2004, ApJ, 610, 745

Lin, Y.-T., et al. 2017, ApJ, 851, 139

Mandelbaum, R., et al. 2005, MNRAS, 361, 1287

Mandelbaum, R., et al. 2013, MNRAS, 432, 1544

Mandelbaum, R., et al. 2018a, PASJ, 70, S25

Mandelbaum, R. 2018b, ARA&A, 56, 393

Mandelbaum, R., et al. 2018c, MNRAS, 481, 3170

Mansfield, P., Kravtsov, A., & Diemer, B. 2017, ApJ, 841, 34

Mantz, A., Allen, S. W., Rapetti, D., & Ebeling, H. 2010, MNRAS, 406, 1759

Markevitch, M., et al. 2004, ApJ, 606, 819

McClintock, T., et al. 2019, MNRAS, 482, 1352

Medezinski, E., et al. 2018a, PASJ, 70, S28

Medezinski, E., et al. 2018b, PASJ, 70, 2, 30

Melchior, P., et al. 2017, MNRAS, 469, 4899

Miyaoka, K., et al. 2018, PASJ, 70, S22

Miyatake, H., et al. 2019, ApJ, 875, 63

Miyazaki, S., et al. 2012, Proc.SPIE, 8446

Miyazaki, S., Oguri, M., Hamana, T., et al. 2015, ApJ, 807, 22

Miyazaki, S., et al. 2018a, PASJ, 70, S1

More, S., Diemer, B., & Kravtsov, A.,V. 2015, ApJ, 810, 36

More, S., et al. 2016, ApJ, 825, 39

Murata, R., Nishimichi, T., Takada, M., Miyatake, H., Shirasaki, M., More, S., Takahashi, R., & Osato, K. 2018, ApJ, 854, 120

Murata, R., Oguri, M., Nishimichi, T., et al. 2019, PASJ, 71, 107

Murata, R., Sunayama, T., Oguri, M., More, S., Nishizawa, A. J., Nishimichi, T.,& Osato, K. 2020, arXiv:2001.01160

Nakajima, R., Mandelbaum, R., Seljak, U., Cohn, J. D., Reyes, R., & Cool, R. 2012, MNRAS, 420, 3240

Navarro, J. F., Frenk, C. S., & White, S. D. M. 1996, ApJ, 462, 563

Nishimichi, T., et al. 2019, ApJ, 884, 29

Nishizawa, A. J., et al. 2018, PASJ, 70, S24

Norberg, P., et al. 2009, MNRAS, 396, 19

Oemler, A. Jr. 1974, ApJ, 194, 1

Oguri, M., Takada, M., Okabe, N., & Smith, G. P. 2010, MNRAS, 405, 2215

Oguri, M. & Takada, M. 2011, Phys. Rev. D, 83, 023008

Oguri, M. 2014, MNRAS, 444, 147

Oguri, M., et al. 2018a, PASJ, 70, S20

Oguri, M., et al. 2018b, PASJ, 70, S26

Okabe, N., Smith, G. P., Umetsu, K., Takada, M., & Futamase, T. 2013,

Okumura, T., Nishimichi, T., Umetsu, K., & Osato, K. 2018, Phys. Rev. D, 98, 3523

Osato, K., Nishimichi, T., Oguri, M., Takada, M. & Okumura, T. 2018, MNRAS, 477, 2141

Ota, N., et al. 2018, PASJ, arXiv:1802.08692

Peacock, J. A. & Smith, R. E. 2000, MNRAS, 318, 1144

Perlmutter, S., et al. 1999, ApJ, 517, 565

Planck Collaboration, et al. 2016, A&A, 594, 13

Planck Collaboration, et al. 2016, A&A, 594, 24

Poggianti, B. M., et al. 1999, ApJ, 518, 576

Pratt, G. W., et al. 2019, Space Sci. Rev., 215, 25

Renzini, A., 2006, ARA&A, 44, 141

Reyes, R., Mandelbaum, R., Gunn, J. E., Nakajima, R., Seljak, U., & Hirata, C. M. 2012, MNRAS, 425, 2610

Riess, A. G., et al. 1998, AJ, 116, 1009

Rowe, B. T. P., et al. 2015, Astronomy and Computing, 10, 121

Rozo, E., et al. 2009, ApJ, 703, 601

Rozo, E., et al. 2010, ApJ, 708, 645

Rozo, E., & Rykoff, E. S. 2014, ApJ, 783, 80

Rozo, E., Rykoff, E. S., Bartlett, J. G., & Melin, J.-B. 2015a, MNRAS, 450, 592

Rozo, E., Rykoff, E. S., Becker, M., Reddick, R. M., & Wechsler, R. H. 2015b, MNRAS, 453, 38

Rykoff, E. S., et al. 2012, ApJ, 746, 178

Rykoff, E. S., et al. 2014, ApJ, 785, 104

Rykoff, E. S., et al. 2016, ApJS, 224, 1

Schneider P., 2006, in Meylan G., Jetzer P., North P., Schneider P., Kochanek C. S., Wambsganss J., eds, Saas-Fee Advanced Course 33: Gravitational Lensing: Strong, Weak and Micro. pp 1–89

Scoccimarro, R., Sheth, R. K., Hui, L., & Jain, B. 2001, ApJ, 546, 20

Seljak, U. 2000, MNRAS, 318, 203

Sheldon, E. S., et al. 2004, AJ, 127, 2544

Shi, X. 2016, MNRAS, 459, 3711

Shin, T., et al. 2019, MNRAS, 487, 2900

Shirasaki, M. & Yoshida, N. 2014, ApJ, 786, 43

Shirasaki, M., Hamana, T., & Yoshida, N. 2015, MNRAS, 453, 3043

Shirasaki, M., Takada, M., Miyatake, H., Takahashi, R., Hamana, T., Nishimichi, T., & Murata, R. 2017, MNRAS, 470, 3476

Shirasaki, M., & Takada, M. 2018, MNRAS, 478, 4277

Shirasaki, M., Hamana, T., Takada, M., Takahashi, R., & Miyatake, H. 2019, MNRAS, 486, 52

Simet, M., McClintock, T., Mandelbaum, R., Rozo, E., Rykoff, E., Sheldon, E., Wechsler, R. H. 2017, MNRAS, 466, 3103

Singh, S., Mandelbaum, R., Seljak, U., Slosar, A., & Vazquez Gonzalez, J. 2017, MNRAS, 471, 3827

Smith, R. E., et al. 2003, MNRAS, 341, 1311

Speagle, J. S., et al. 2019, arXiv:1906.05876

Spergel, D., et al., 2015, arXiv:1503.03757

Springel, V., et al. 2005, Nature, 435, 629

Stanford, S. A., Eisenhardt, P. R., & Dickinson, M. 1998, ApJ, 492, 461

Sugiura, H., Nishimichi, T., Rasera, Y., & Taruya, A. 2019, arXiv:1911.05394

Sunayama, T. & More, S. 2019, MNRAS, 490, 4945

Takada, M., & Bridle, S. 2007, New Journal of Physics, 9, 446

Takada, M., & Hu, W. 2013, Phys. Rev. D, 87, 123504

Takahashi, R., Sato, M., Nishimichi, T., Taruya, A., & Oguri, M. 2012, ApJ, 761, 152

Takahashi, R., Hamana, T., Shirasaki, M., Namikawa, T., Nishimichi, T., Osato, K., & Shiroyama, K. 2017, ApJ, 850, 24

Takahashi, R., Nishimichi, T., Takada, M., Shirasaki, M., & Shiroyama, K. 2018, MNRAS, 482, 4253

Tanaka, M., et al. 2018, PASJ, 70, S9

Tinker, J. L., Robertson, B. E., Kravtsov, A. V., Klypin, A., Warren, M. S., Yepes, G., & Gottlöber, S. 2010, ApJ, 724, 878

Umetsu, K., Broadhurst, T., Zitrin, A., Medezinski, E., Coe, D., & Postman, M. 2001, ApJ, 738, 41

Umetsu, K. & Diemer, B. 2017, ApJ, 836, 231

Vikhlinin, A., et al. 2009, ApJ, 692, 1060

Vogelsberger, M., Marinacci, F., Torrey, P., & Puchwein, E. 2019, arXiv:1909.07976

Voit, G. M. 2005, Reviews of Modern Physics, 77, 207

von der Linden, A. et al. 2014, MNRAS, 443, 1973

Walker, S., et al. 2019, Space Sci. Rev., 215, 7

Wechsler, R. H., & Tinker, J. L. 2018, ARA&A, 56, 435

Weinberg, D. H., Mortonson, M. J., Eisenstein, D. J., Hirata, C., Riess, A. G., & Rozo, E. 2013, Phys. Rep., 530, 87

Wetzel, A. R., Tinker, J. L., Conroy, C., & van den Bosch, F. C. 2013, MNRAS, 432, 336

White, S. D. M., Efstathiou, G., & Frenk, C. S. 1993, MNRAS, 262, 1023

Wong, K. C., et al. 2019, arXiv:1907.04869

Xhakaj, E., et al. 2019, arXiv:1911.09295

Zhang, Y., et al. 2019, MNRAS, 487, 2578

Zheng, Z., et al. 2005, ApJ, 633, 791

Zinger, E., Dekel, A., Kravtsov, A. V., & Nagai, D. 2018, MNRAS, 475, 3654

Zu, Y., Weinberg, D. H., Rozo, E., Sheldon, E S., Tinker, J. L., & Becker, M. R. 2014, MNRAS, 439, 1628

Zu, Y., Mandelbaum, R., Simet, M., Rozo, E., & Rykoff, E. S. 2017, MNRAS, 470, 551

Zürcher, D. & More, S. 2019, ApJ, 874, 184

Zwicky, F. 1933, Helvetica Physica Acta, 6, 110